

# ABSTRACT

Title of Document: COPPER OXIDE NANOARCHITECTURES FOR PHOTOELECTROCHEMICAL HYDROGEN GENERATION

Chia-Ying Chiang, Doctor of Philosophy, 2012

Directed By: Professor Sheryl H. Ehrman,  
Department of Chemical and Biomolecular Engineering

Hydrogen is a high-quality energy carrier, similar to electricity, which can be used with high efficiency and near-zero emissions at the point of use. The most promising means of producing hydrogen using a renewable energy source and potentially reducing the generation of greenhouse gases production is through solar-hydrogen photoelectrochemical (PEC) water decomposition. In order to utilize the solar irradiation, small band gap material is essential. In this dissertation, I focus on the earth abundant, non-toxic and direct transit copper oxide (CuO) with band gap around 1.3-1.8 eV. In a PEC cell, the photo-excited charge carriers need to be separated as soon as they form in order to have a high photocurrent density. Thus, four approaches are studied: (1) decrease particle size to decrease the electron-hole recombination in the particles, (2) increase surface area to increase the active sites and decrease the distance for electrons travel to the surface to react with water (3) increase conductivity to decrease the resistance of the electrode, and (4) shorten charge carrier transport distance to decrease the chance of recombination of charge carriers.

In the first part of this study, I describe the aerosol route, flame spray pyrolysis, for making CuO nanoparticles. By controlling the precursor concentration and flame conditions, the particle size can be tuned. Also, the simulation results of particle growth, based on collision/sintering theory

with sintering by solid state diffusion, are in good agreement with the experimental results. Furthermore, the flame spray pyrolysis made CuO nanoparticles were spin coated on conducting ITO glass substrates for the PEC study. Here, the relatively uniform CuO nanoparticles showed much better photocurrent density compared to the commercial CuO nanoparticles with a broad size distribution. This demonstrates the importance of the size of material for PEC application.

The second approach I introduced is to increase surface area to increase the active sites. Instead of changing the CuO suspension concentration to make films with different porosity, I present a new route for forming porous structures by spin coating the powder including CuO and its intermediate product,  $\text{Cu}_2(\text{NO}_3)(\text{OH})_3$ . During the post annealing process, the intermediate product transforms into CuO and leaves voids in the film, thus producing a porous film and increasing the active surface area for the water splitting reaction.

In the third approach, lithium was incorporated as a dopant to increase conductivity and decrease the resistance of the electrode. With the lithium added, the conductivity increased by two orders of magnitude and thus highly decreased the film resistance and increased the photocurrent density.

The final part of this dissertation focuses on three dimensional current collectors, used to decrease the charge carrier transport distance and thus decrease the chance of recombination. Here, the genetically modified tobacco mosaic virus (TMV1cys) served as a template for the three dimensional structure, made by sputter deposition of CuO. By varying the virus concentration, the distance between the current collectors can be tuned to optimize the charge carrier transport distance, light reflection as well as the CuO thickness for efficient absorption of solar energy.

**COPPER OXIDE NANOARCHITECTURES FOR  
PHOTOELECTROCHEMICAL HYDROGEN GENERATION**

By

Chia-Ying Chiang

Dissertation submitted to the Faculty of the Graduate School of the  
University of Maryland, College Park in partial fulfillment  
of the requirements for the degree of  
Doctor of Philosophy  
2012

Advisory Committee:

Professor Sheryl Ehrman, Committee Chair

Professor Srinivasa R. Raghavan

Professor Raymond A. Adomaitis

Professor Michael Zachariah

Professor Lourdes G. Salamanca-Riba

© Copyright by  
Chia-Ying Chiang  
2012

## ACKNOWLEDGEMENTS

Endless thanks to my advisor, Dr. Sheryl Ehrman, for the advice, support and freedom that she gave me during the years. I would like to thank for the funding support from *A. James Clark School of Engineering Distinguished Fellowship* and *Anneke Levelt Sengers Graduate Fellowship* for supporting my first PhD year and *National Science Foundation DMR 0806610* for the rest of the years. I would also like to thank Dr. Srinivasa R. Raghavan, Dr. Raymond A. Adomaitis, Dr. Michael Zachariah, and Dr. Lourdes G. Salamanca-Riba for serving on my committee and providing me with valuable suggestions and corrections. Additionally, I would like to acknowledge Dr. Peter Zavalij for performing XRD, Dr. Karen Gaskell for performing XPS, and Dr. Li-Chung Lai for helping on the SEM/TEM experiments. Also, the undergrads, Nick Franson, Kosi Aroh, Yoon Shin, and Jillian Epstein for their hard work.

Without *American Friend's* and *International Friend's* lovely people, especially Jeanne McMahon, Susan Cole, and Sue Hoffman, I could've gone through those difficulties in understanding American culture/language and enjoyed the holiday feasts. For those seniors from Taiwan, thanks for taking care of me throughout the years and sharing the happiness and sadness with me. I am so lucky to be here with you guys!

## DANCE MY DREAM

逐夢踏實 生活故事

舞動夢想 轉動地球

# TABLE OF CONTENTS

Acknowledgements .....	ii
Table of Contents .....	iii
List of Tables .....	vi
List of Figures.....	vii
<b>I. Introduction and Overview .....</b>	<b>1</b>
1.1. Problem Description and Motivation.....	1
1.2. Approach.....	2
1.2.1. Decrease Particle Size.....	4
1.2.2. Increase Surface Area .....	4
1.2.3. Increase Conductivity .....	5
1.2.4. Shorten Transport Distance .....	5
<b>II. Background Information .....</b>	<b>6</b>
2.1. Storage of Solar energy.....	6
2.2. Hydrogen Generation by Water Splitting .....	7
2.2.1. Photoelectrochemistry of Semiconductors .....	9
2.2.2. Difficulty and Approach .....	18
2.3. Materials for PEC .....	27
2.3.1. Wide Band Gap Materials .....	28
2.3.2. Small Band Gap Materials.....	30
2.4. Copper Oxide Properties.....	31
2.5. Nanodesign for Copper Oxide Photocathodes .....	33
<b>III. Copper Oxide Nanoparticle Made by Flame Spray Pyrolysis for PEC Water Splitting – CuO Nanoparticle Preparation.....</b>	<b>34</b>
3.1. Abstract .....	34
3.2. Introduction .....	35

3.3. Materials and Methods .....	38
3.3.1. Aerosol Generator and Flame Conditions .....	38
3.3.2. Particle Sampling and Characterization.....	42
3.4. Results and Discussion .....	43
3.4.1. Experiment.....	43
3.4.2. Modeling of CuO Growth by Solid State Diffusion .....	51
3.5. Conclusions .....	56
<b>IV. Copper Oxide Nanoparticle Made by Flame Spray Pyrolysis for PEC Water Splitting – Photoelectrochemical Study .....</b>	<b>57</b>
4.1. Abstract .....	57
4.2. Introduction .....	58
4.3. Materials and Methods .....	61
4.3.1. CuO Particle Preparation .....	61
4.3.2. Electrode Preparation .....	61
4.3.3. Characterization.....	62
4.4. Results and Discussion .....	65
4.5. Conclusions .....	78
<b>V. Li Doped CuO Film Electrodes for Photoelectrochemical Cells .....</b>	<b>79</b>
5.1. Abstract .....	79
5.2. Introduction .....	80
5.3. Experimental .....	82
5.3.1. CuO Particle Preparation .....	82
5.3.2. Electrode Preparation .....	82
5.3.3. Characterization .....	83
5.4. Results and Discussion .....	86
5.5. Conclusions .....	96
<b>VI. Copper Oxide Photocathodes Prepared by a Solution Based Process .....</b>	<b>97</b>
6.1. Abstract .....	97
6.2. Introduction .....	98

6.3. Materials and Methods .....	100
6.3.1. CuO Particle Formation .....	100
6.3.2. Photoelectrode Preparation .....	100
6.3.3. Characterization of PEC Electrode/Cell .....	101
6.4. Results and Discussion .....	103
6.5. Conclusions.....	117
<b>VII. Biological Templates for Anti-reflectance Surface and Current Collectors for Photoelectrochemical Cell Applications .....</b>	<b>118</b>
7.1. Abstract .....	118
7.2. Introduction .....	119
7.3. Materials and Methods .....	122
7.3.1. TMV1cys Preparation .....	122
7.3.2. Self-Assembly and Mineralization .....	123
7.3.3. Sputtering ITO and CuO .....	123
7.3.4. Analysis .....	125
7.4. Results and Discussion .....	126
7.5. Conclusions .....	138
<b>VIII. Conclusions and Future Work .....</b>	<b>140</b>
8.1. Conclusions .....	140
8.2. Future Work .....	143
8.2.1. CuO Stability Improvement .....	143
8.2.2. Possible Nanoarchitectures for PEC Cells .....	144
8.2.3. Effects of Particle Size/Surface Area/Porosity on PEC Cells .....	145
<b>Appendices .....</b>	<b>149</b>
A.1. Film Porosity/Total Surface Area Estimation .....	149
<b>References .....</b>	<b>152</b>



## LIST OF TABLES

Table 3.1. Flame composition and characteristic .....	40
Table 3.2. Precursor concentration vs particle size, for flame set A .....	44
Table 3.3. The comparison of flame A and B at precursor concentration of 17% and 35% .....	47
Table 3.4. Particle size based on both flames and heights from the burner cover for 17% precursor .....	47
Table 3.5. Collision/sintering theory modeling result based on different surface tensions .. .....	54
Table 3.6. The effect of liquid nitrogen quenching on particle size and crystallinity .....	55
Table 4.1. The optical band gaps of CuO films prepared from different sintering temperature and duration .....	67
Table 5.1. The effect of Li doping concentration of the lattice parameter $a$ .....	86
Table 7.1. PEC results based on different CuO thickness and TMV concentrations .....	132
Table 7.2. Photocurrent density of CuO photocathodes in different systems.....	138

## LIST OF FIGURES

Figure 1.1. Four main approaches to increase the CuO photocathodes PEC efficiency: (1) decrease particle size, (2) increase surface area, (3) increase conductivity, and (4) shorten charge carrier transport distance .....	3
Figure 2.1. Amount of energy produced by combustion of different fuels and related carbon emissions (showing also the amount of carbon emission during hydrogen generation by methane reforming). .....	9
Figure 2.2. Solar irradiance based on the wavelength at difference air mass condition...	10
Figure 2.3. The band energy diagram of a p-type semiconductor cathode and a metal anode in electrolyte with illumination. ....	14
Figure 2.4. The band structures of both electrodes, involving the photo-cathode of a p-type semiconductor and metallic anode, at different stages in the formation of the electrochemical chain. $\phi$ is the work function, $E_c$ , $E_f$ , $E_v$ represent for conduction bend energy, bandgap, valence bend energy. $V_{ph}$ is the generation of photovoltage and $V_B$ is the semiconductor surface's electrical potential. ....	15
Figure 2.5 Ideal behavior for a p-type semiconductor in the dark (black dot line) and under irradiation (red solid line). $E_{fb}$ is flatband potential. $i_a$ and $i_c$ represent for anodic current and cathodic current.....	16
Figure 2.6. Effect of particulate size on the electronic structure adopted from Hoffmann et al. (1995).....	23
Figure 2.7. Position of decomposition potentials $E_{n,d}$ and $E_{p,d}$ vs. $E_c$ and $E_v$ of selected semiconductors (Gerischer, 1979). CuO information was calculated and added by Chiang. All the information is based on pH7. ....	25
Figure 2.8. Band gap energies and relative band positions of different semiconductors related to water oxidation/reduction potential (vs.NHE) at pH=0. ....	28

Figure 2.9. Energy levels of aliovalent ions in rutile TiO <sub>2</sub> lattice. ....	30
Figure 2.10. Crystal structure of CuO.....	32
Figure 2.11. pH-potential diagrams (Pourbaix diagram) for the Cu-H <sub>2</sub> O system. ....	32
Figure 3.1. Schematic of the apparatus for the flame spray pyrolysis system .....	39
Figure 3.2. Temperature profile of the both flames .....	41
Figure 3.3. XRD for particles based on different precursor concentrations .....	43
Figure 3.4. TEM micrograph for particles based on different precursor concentrations: (a) 35%, (b) 25%, (c) 17%, (d) 5%, and (e) 0.5% .....	45
Figure 3.5. Particle size distribution based on different precursor concentration .....	46
Figure 3.6. TEM micrograph for particles collected at different heights for both flame conditions .....	49
Figure 3.7. Histogram for particles collected at different heights for both flame conditions: (a) flame A, and (b) flame B .....	50
Figure 3.8. Temperature vs. residence time for both flames .....	51
Figure 4.1. Scanning electron micrographs of samples sintering at different temperature and period: (a) 450 °C for 1 hr, (b) 450 °C for 3 hr, (c) 600 °C for 1 hr, (d) 600 °C for 3 hr .....	65
Figure 4.2. X-ray diffraction patterns of CuO films deposited on a ITO glass substrate .....	66
Figure 4.3. The relationship between $(\alpha h\nu)^2$ and $(h\nu)$ for CuO films with thickness of 580 nm which were sintered at 450 °C and 600 °C and for 1 hr and 3 hr .....	68
Figure 4.4. Current-potential (I-V) characteristics curve for a CuO/ITO electrode (thickness of CuO layer is 580 nm and sintered at 600 °C for 3 hr) in the dark and under illumination in a 1 M KOH electrolyte .....	70

Figure 4.5. Net photocurrent density of different thickness of CuO/ITO electrodes sintering at (a) 450 °C for 1 hr, and (b) 600 °C for 3 hr .....	71
Figure 4.6. Net photocurrent density of CuO/ITO electrodes (CuO thickness is 580 nm) with different CuO sources and sintering temperatures .....	72
Figure 4.7. Scanning electron micrographs of CuO film sintered at 450 °C from different CuO sources: (a) purchased from Sigma-Aldrich, (b) made by our FSP system .....	73
Figure 4.8. Mott-Schottky plots for a CuO/ITO electrode in 1 M KOH electrolyte .....	76
Figure 4.9. Estimated position of CuO bandedges for this study, performed at pH 14, and prior reports in the literature adjusted to pH 14 .....	77
Figure 5.1. XRD for flame spray pyrolysis made Li doped CuO particles .....	87
Figure 5.2. Sintering temperature effect on 2 at% Li doped CuO with thickness of 850 nm .....	88
Figure 5.3. The relationship between $(ah\nu)^2$ and $(h\nu)$ for Li doped CuO powders sintered at different temperatures .....	89
Figure 5.4. SEM image of 2 at% Li doped CuO sintered at (a) 450 °C for 1 hr, and (b) 600 °C for 3 hr .....	90
Figure 5.5. Dopant concentration effects on CuO film: (a) film with thickness of 850 nm and sintered at 450 °C for 1 hr, (b). film with thickness of 850 nm and sintered at 600 °C for 3 hr .....	92
Figure 5.6. The effects of different thickness for the 2 at% Li doped CuO sintered at 450 °C for 1 hr .....	93
Figure 5.7. The Mott-Schottky plot for Li doped CuO-ITO electrode sintered at 450 °C for 1hr in 1M KOH electrolyte .....	95
Figure 6.1. The configuration of the cell and the CuO photocathode structure .....	102
Figure 6.2. X-ray diffraction patterns of CuO powders as prepared .....	104

Figure 6.3. Transmission electron micrographs of samples produced at different temperature and duration: (a) 25 °C for 24 hr, (b) 60 °C for 45 min, (c) 95 °C for 30 min...  
..... 105

Figure 6.4. Scanning electron micrographs of samples produced at 25 °C, 60°C, and 95°C and sintered at 200°C, 400°C and 600°C for 1 hr ..... 106

Figure 6.5. X-ray diffraction patterns of CuO films sintered at different temperatures ..107

Figure 6.6. The relationship between  $(ah\nu)^2$  and  $(h\nu)$  for CuO powder prepared under different reaction conditions and their films sintered at different temperature. The first temperature in the caption is the solution reaction temperature and the second one is the powder sintering temperature ..... 108

Figure 6.7. Current-potential (I-V) characteristics curve for 4 layered CuO/ITO electrodes sintered at different temperatures in the dark and under illumination in a 1 M KOH electrolyte: (a) powder prepared at 25 °C, (b) powder prepared at 60°C, (c) powder prepared at 95°C..... 110

Figure 6.8. Current-potential (I-V) characteristics curve of different thickness of CuO/ITO electrodes: (a) powder prepared at 25 °C and sintered at 600°C, (b) powder prepared at 60°C and sintered at 600°C ..... 111

Figure 6.9. Mott-Schottky plots for a CuO/ITO electrode in 1 M KOH electrolyte ..... 112

Figure 6.10. Scanning electron micrographs of the bird-eye view and side view of sample prepared at 60 °C and sintered at 600 °C ..... 113

Figure 6.11. Estimated position of CuO bandedges for this study, performed at pH 14, and prior reports in the literature (Chiang et al., 2011; Nakaoka et al., 2004; Koffyberg and Benko, 1982) adjusted to pH 14..... 115

Figure 7.1. Diagram of the assembling processes for CuO photocathode with a final bird-eye view illustration: (A) TMV1cys self-assembly onto Au coated substrate, (B) Pd

activated the virus surface, (C) Ni uniformly coated on the virus surface, and (D) sputter deposition of ITO and CuO .....	124
Figure 7.2. TEM image of nickel-coated TMV1cys after heat treatment at 300 °C for 1 hr. ....	126
Figure 7.3. TEM image of a CuO/ITO/NiO nanowire with 15 min and 4 min sputter deposition of CuO and ITO and sintered at 450 °C for 1 hr .....	127
Figure 7.4. XRD for the film of CuO/ITO/NiO-TMV1cys/Au/ITO-glass .....	127
Figure 7.5. TMV concentration effects on the charge transport distance to the current collector and SEM micrographs for the surface morphology of 15 min CuO sputter deposition on different TMV1cys concentration prepared template current collector: (A) plain substrate, (B) 10 <sup>-4</sup> mg/mL, (C) 10 <sup>-3</sup> mg/mL, (D) 10 <sup>-2</sup> mg/mL and 10 <sup>-1</sup> mg/mL. ...	129
Figure 7.6. PEC performance of CuO deposited on plain substrates for the sputter deposition time of 5 min, 15min and 30 min along with a 15 min CuO deposition on TMV1cys patterned substrate. ....	130
Figure 7.7. Appearance of samples with 520 nm CuO deposited on different substrates: (b) flat substrate with mirror like surface, (b4) virus patterned substrate with structure period more than 500 nm, (b3) to (b1) virus patterned substrate with patterned period less than 500 nm which suppress the light reflection. ....	131
Figure 7.8. Reflectance of samples with 15 min CuO deposited on different TMV1cys concentration substrates. ....	135
Figure 7.9. SEM image of virus solution at 10 <sup>-2</sup> mg/mL and sputtering coated with 4 min ITO and various deposition time for CuO: (a) 5 min (b) 15 min and (c) 30 min. ....	136
Figure 7.10. Illustration of the detail construction of virus template, current collector and each CuO rods at different CuO deposition thickness. ....	137

Figure 8.1. Different strategies for stabilization of semiconductor electrolyte interface: (a) surface layer of noble metal or stable semiconductor, (b) stabilization with polymer layer along with electron transfer catalysts, (c) stabilization through catalytic surface states. 144

Figure 8.2. Four different structures for photoelectrochemical cells: (a) Polycrystalline network, (b) polycrystalline nanotube, (c) single-crystal nanowire array, and (d) network of single-crystalline nanowires and dispersed nanoparticles. (Faglia et al., 2009) ..... 145

Figure 8.3. The illustration of *C* ..... 146

Figure A.1. Cross-section view of the film..... 149

# Chapter 1

## Introduction and Overview

This dissertation is focused on the preparation of CuO nanoparticles and CuO thin film architectures to increase the photoelectrochemical (PEC) solar hydrogen generation efficiency. In this chapter, overall problems, approaches, and significant result of this work are outlined.

### 1.1. PROBLEM DESCRIPTION AND MOTIVATION

Several energy crises in the past half century have served as wake-up calls, reminding people of the limited nature of fossil fuels. Since the first crisis happened in the 1970s, scientists and engineers have devoted significant effort towards searching for renewable energy alternatives. One of the most promising energy carriers also as replacement for hydrocarbons is hydrogen (Rifkin, 2002; Hussain et al., 2007). Besides the benefit of its high energy density, it also leaves near-zero emissions at the point of use and thus reduces the production of the global warming gases. However, based on the most used hydrogen generation technique, i.e. steam reformation of natural gas, mostly methane, the issue of the fossil fuel requirement cannot be eliminated. In 1972, two Japanese researchers (Fujishima and Honda, 1972) demonstrated that hydrogen gas can be generated by absorbing the solar energy via a semiconductor electrode ( $\text{TiO}_2$ ), and with photon excited electrons performing the water splitting reaction at the electrode/electrolyte interface. One of the critical issues in this process is the efficiency:



how much of the incident solar energy can be absorbed by the material. The wide band gap materials, such as 3.2eV for TiO<sub>2</sub>, only absorb less than 10% of the solar energy incident on Earth which limits the efficiency. In contrary, small band gap materials can absorb more light, and thus from the most fundamental point of view, a much higher efficiency can be expected.

A small band gap material, CuO, serving as a photocathode for water splitting is a promising approach to generate renewable solar hydrogen energy but CuO still needs tremendous improvements in the electron-hole recombination rate, conductivity, and stability before it can be demonstrated to have commercial potential. In this study, four main concepts are introduced to increase the efficiency of CuO photocathodes for water splitting.

## **1.2. APPROACH**

In optimizing the properties of CuO as well as CuO photocathode architectures, there are four main aspects to address as illustrated in Figure 1.1: (1) decrease particle size to decrease the electron-hole recombination in the particles, (2) increase surface area to increase the active sites and decrease the distance for electrons travel to the surface to react with water, (3) increase conductivity to decrease the resistance of the electrode, and (4) shorten charge carrier transport distance to decrease the chance of recombination of charge carriers. In the process of working on these approaches, the understanding of the basic aerosol dynamics, semiconductor photoelectrochemistry and solid state physics are essential. Thus, detailed background information about the semiconductor

photoelectrochemistry and solid state physics is given in Chapter 2. In a detailed study of CuO nanoparticles prepared by flame spray pyrolysis (FSP), an aerosol route, factors such as varying precursor concentration, introducing quenching gas, flame condition, and particle growth history are studied to control the particle size which is given in Chapter 3. Along with the experiments, the simulation of particle growth based on collision/sintering theory was shown to have a reasonable agreement with the experimental result.

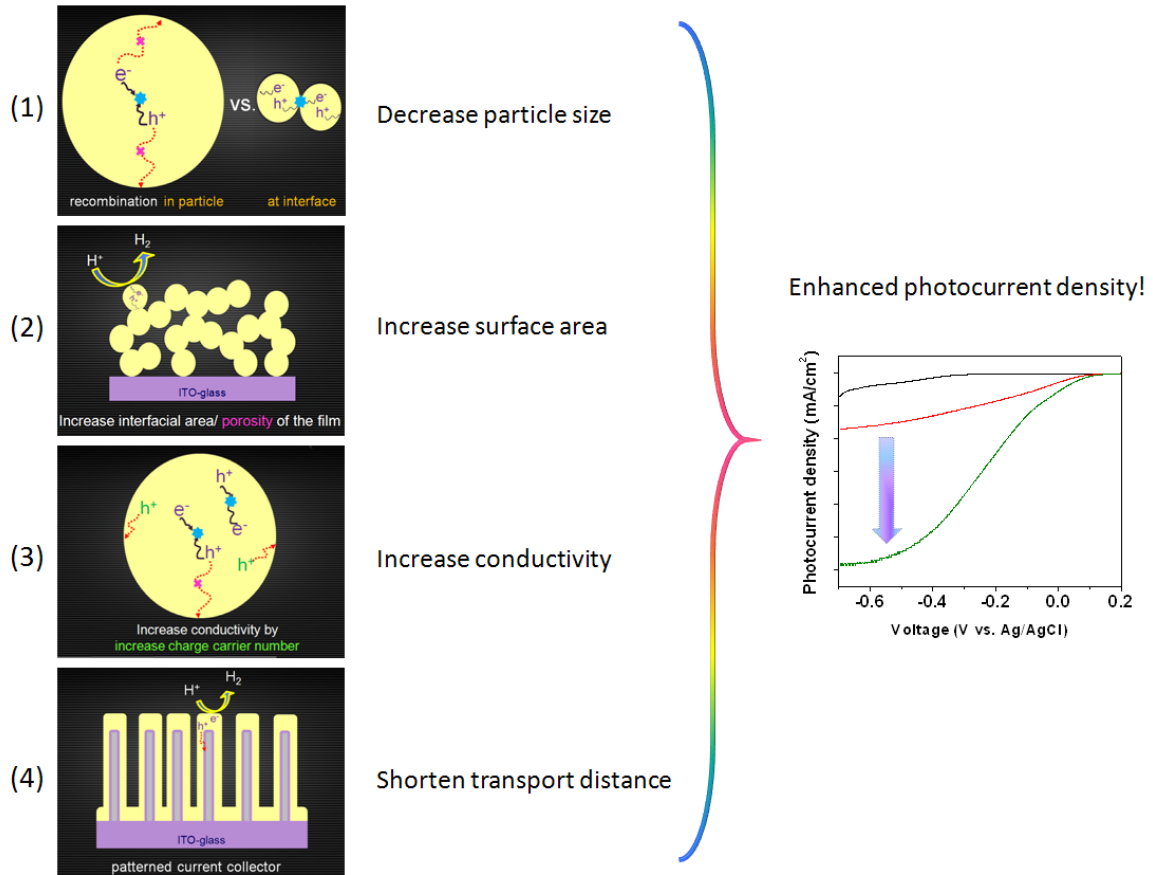


Figure 1.1. Four main approaches to increase the CuO photocathodes PEC efficiency: (1) decrease particle size, (2) increase surface area, (3) increase conductivity, and (4) shorten charge carrier transport distance.

### **1.2.1. Decrease Particle Size**

Particle size is an important issue when CuO serves as a photocathode because it affects the band gap as well as the surface area. Furthermore, as reported in the literature (Jeong and Choi, 1996), the generated electron and hole pairs are more likely to recombine within the CuO particles instead of at the edge of the particles. As a result, decreasing the size might decrease the charge carriers' recombination and thus increase the photocurrent density. Also, a uniform particle size distribution might be helpful when a sintering process is needed to build up the connection between particles. Several methods such as FSP (Chapter 3) and wet chemical process (Chapter 6) are successfully demonstrated the production of CuO nanoparticles. These CuO particles have relatively uniform size distribution compared to the commercial CuO nanoparticles from Sigma-Aldrich (claim to have average size of 50 nm). Improvements in photocurrent density are shown in Chapter 4 and Chapter 6 for the FSP and wet chemical, respectively.

### **1.2.2. Increase Surface Area**

In addition to decreasing the particle size, increasing the porosity of the film might be able to increase the useable surface area of the film electrode. Interestingly, there is no such study to date on CuO photocathodes! There are several ways to prepare films with different porosity such as varying the concentration of the slurry and the intermediate product concentration left in the powder before sintering. Here, the second approach is of higher interest since it wastes less material while spin coating the CuO on the substrate. Results of these experiments are given in Chapter 6.

### **1.2.3. Increase Conductivity**

Li is known for its ability to increase the conductivity of CuO films as high as two orders of magnitude (Suda et al., 1992; Ohya et al., 2000; Saito et al., 2003). Here, in Chapter 5, Li doped films are described. Li doped CuO nanoparticles prepared by flame spray pyrolysis and the CuO film was made by spin coating. The dopant concentrations also play an important role in the CuO photocathode since the alien ions are defects and serve as recombination centers. The details of the increase of conductivity, charge carrier concentration, and photocurrent density are given in Chapter 5.

### **1.2.4. Shorten Transport Distance**

Not only decrease particle size can reduce the probability of electrons/holes recombination, shorten the charge carrier transport distance can also reduce the chance. Thus, the combination of these two approaches is expected to highly increase the photocurrent density. Here, a magnetron sputtering technique was introduced to prepare the CuO film on a genetic modified virus patterned 3D current collector surface. The genetic modified tobacco mosaic virus, i.e. TMV1cys, can self-assemble on a gold coated surface and aligned themselves in a nearly vertical position. These nanorod structures then served as the scaffold for the deposition of the 3D ITO current collectors. By controlling the virus concentration, a desired distance between the nanorod current collectors can be achieved to optimize the photon-excited charge carrier transport distance. More details about this idea can be found in Chapter 7.

## **Chapter 2**

### **Background Information**

A review of solar hydrogen generation is described in this chapter along with the chemical and physical concepts associated with semiconductor electrochemistry. Details of material selection criteria for photoelectrochemical (PEC) cell applications are then discussed and the last part is focused on the properties of p-type CuO photocathodes for PEC applications.

#### **2.1. STORAGE OF SOLAR ENERGY**

Solar energy is not available after sunset or in cloudy days and thus the energy storage is an important issue. Solar energy can be stored by heating a material that goes phase change such as paraffin wax or by heating a material with high specific heat capacity such as salt. However, the energy might not be portable based on above methods. For a portable solar energy system, such as a photovoltaic cell combined with rechargeable batteries might overcome this issue but the life time for batteries usually about 2-7 years might be a concern for a long term usage while the lifetime for a combustion engine is about 10 years. As a result, a high quality energy carrier such as hydrogen is essential for the portable solar energy system.

## 2.2. HYDROGEN GENERATION BY WATER SPLITTING

Decreasing fossil fuel supply and endlessly increasing fossil fuel demand have led to several energy crises since the 1970s. In order to ease the rate of fossil fuel consumption and decrease CO<sub>2</sub> emissions from burning fossil fuels, renewable clean energies such as wind, rain, tides, geothermal heat and sunlight are needed. Among various alternative energy sources, hydrogen fuel offers the highest potential benefits in terms of diversified supply and reduced emissions of pollutants and greenhouse gases (Nowotny et al., 2005). It also has the highest energy content per unit mass of any fuel, i.e. 140.4 MJ/kg for hydrogen and 48.6 MJ/kg for gasoline. However, the situation is reversed if the volume basis is considered, i.e. 8,491 MJ/m<sup>3</sup> for liquid hydrogen and 31,150 MJ/m<sup>3</sup> for gasoline (Gupta, 2009).

Similar to electricity, hydrogen is a high-quality energy carrier, which can be used with a high efficiency and near-zero emissions at the point of use. It has been technically demonstrated that hydrogen can be used to replace current fuels in all their present uses such as transportation, heating, and power generation (Rifkin, 2002; Hussain et al., 2007). The key assertions of the initiative for hydrogen production and utilization are based on the premise that the fuel cell is a proven technology and hydrogen is in abundant supply on Earth (Ogden et al., 1995; Ogden, 1999). But unfortunately, most of the hydrogen on Earth is in the fully oxidized form, H<sub>2</sub>O, which has no fuel value. Therefore, to obtain hydrogen from natural compounds, energy expenditure is needed. Hydrogen can be produced using a variety of starting materials, derived from both renewable and nonrenewable sources, through many different process routes such as reformation of natural gas and electrolysis of water. However, hydrogen generated using renewable

energy is environmentally friendly; it will soon join solar electricity to form the foundation of a sustainable modern energy system (Bak et al., 2002).

Based on the information shown in Fig. 2.1 (Nowotny et al., 2005), the most promising means of producing hydrogen using a renewable energy source and apparently reducing the generation of greenhouse gases production is through solar-hydrogen photoelectrochemical water decomposition (Veziroglou, 1998; Veziroglou, 2000; Bak et al., 2002). This involves the splitting of water into its component gases (oxygen and hydrogen) by using solar energy. With this concept, coupling the widely commercial photovoltaic electricity generation systems, a dc-dc converter and an electrolyzer, solar to hydrogen conversion efficiency has been demonstrated to be around 8% (Bard and Fox, 1995; Hollmuller et al., 2000; Vidueira et al., 2003). However, much higher electric potential, i.e. 1.9 V, than the minimum required potential for water splitting, i.e. 1.23 V, is needed for a commercial electrolyzer to operate at its optimal condition, and thus it limits the overall energy conversion efficiency (Bard and Fox, 1995). In contrary, a more straightforward method to generate hydrogen by water splitting is based on a semiconductor photoelectrochemical (PEC) cell where the photon generated electron-hole pair can perform the water splitting directly, eliminating the electrolyzer step. Usually, the current density generated by a semiconductor photoelectrode immersed in water is much smaller, i.e. 10-20 mA/cm<sup>2</sup> at most, and the required overpotential is therefore substantially lower (Krol and Grätzel, 2011). Another advantage of a PEC system is that it can be constructed as a single, monolithic device and thus significantly lower the costs by decreasing the number of packaging components such as frame, glass, connections, etc (Krol and Grätzel, 2011).

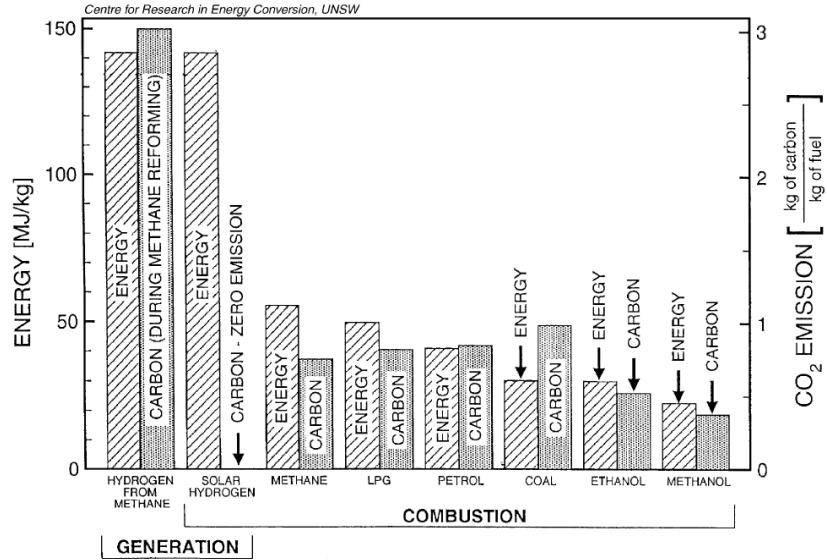


Fig. 2.1. Amount of energy produced by combustion of different fuels and related carbon emissions (showing also the amount of carbon emission during hydrogen generation by methane reforming). (Nowotny et al., 2005)

### 2.2.1. Photoelectrochemistry of Semiconductors

There are three major processes for PEC systems: photon absorption, electron-hole generation and separation, and chemical reaction. The following sections, they will be discussed in this order.

#### Photon Absorption

Solar radiation is electromagnetic radiation in the wavelength range of 0.28-3.0  $\mu\text{m}$  (Fig. 2.2). The spectrum includes 2% of ultraviolet radiation (0.28-0.38  $\mu\text{m}$ ), around 49% of the visible light ranging from 0.38-0.78  $\mu\text{m}$ , and the remaining 49% of infrared radiation with long wavelength (0.78-3.0  $\mu\text{m}$ ). The extraterrestrial spectrum of the sun's radiant energy can be approximated by that of a black body radiator at 6000 K, the temperature



of the surface layer of the sun, and the total power density of the solar radiation outside the Earth's atmosphere is referred to as the solar constant, i.e.  $1353 \text{ W/m}^2$ . However, as the light penetrates through the atmosphere, the radiation is attenuated. The sunlight that has a typical spectrum at the Earth's surface is termed air mass 1.5 global (AM 1.5 G) which corresponds to an angle of 48.2 degree between the position of sun and the zenith. Here, the air mass (number) defines the number of times sunlight traversed the thickness of the Earth's air atmosphere and can be expressed as

$$\text{Air mass} = (\cos\theta)^{-1} \quad (\text{Eq. 2.1})$$

The word global (in air mass 1.5 global) means the total radiation from direct and diffuse radiation. The irradiance of the AM 1.5 radiation is  $827 \text{ W/m}^2$ . However, the commonly used standard AM 1.5 G with radiation of  $1000 \text{ W/m}^2$  is close to the maximum received at the Earth's surface.

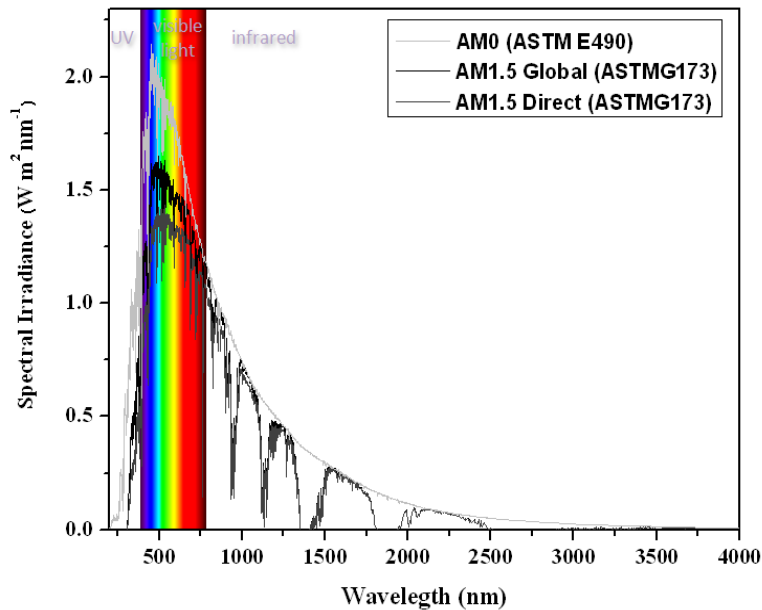
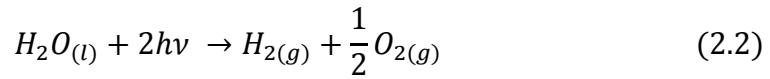


Fig. 2.2. Solar irradiance based on the wavelength at difference air mass condition.

(Spectrum data from [www.astm.gov](http://www.astm.gov))

Considering absorption of energy from the solar spectrum above the threshold energy ( $E_t$ ), a material with band gap smaller or equal to the threshold energy can be used. Thus, the band gap of a photoelectrode has a critical impact on the energy conversion of photons (Wenham et al., 1994). The ideal threshold energy for water splitting is also important.

The overall reaction, PEC water splitting to generate hydrogen and oxygen, is an endothermic reaction accompanied by a large increase in Gibbs free energy ( $\Delta G^o = 237.1$  kJ/mol) which can be calculated by the change of the Gibbs free energy of formation ( $\Delta_f G^o$ ), i.e.  $\Delta G^o = \sum \Delta_f G_{product}^o - \sum \Delta_f G_{reactant}^o$ . This energy can be provided by energetic photons and is expressed as



Reaction (2.2) takes place when the energy of the photons absorbed by the photocathode is equal to or larger than  $E_t$ :

$$E_t^o = \frac{\Delta G^o}{nF} \quad (2.3)$$

where  $F$  is the Faraday constant, equal to  $eN_A$  and  $N_A$  is Avogadro's number and  $e$  is the elementary charge. This yields  $E_t^o = 1.23$  eV, and it is the theoretical equilibrium potential. For actual required cell voltage for the reaction, higher voltage is necessary to conquer the ohmic loss of the electrolyte and overpotential on the electrode/electrolyte interface reaction.

However, when light hits the interface between materials with different refractive indices, a significant portion of it is reflected. In previous PEC studies, have seldom investigated

the efficient utilization of incident light as a means to enhance PEC activity, meaning decreasing the reflection by mimicking the surface structure of nature structures such as moth eye, i.e. a periodical nanostructure. This structure works because the nanostructures are smaller than the wavelength of visible light, and thus the light sees the surface having a continuous refractive index gradient between the air and the medium, which decreases reflection by removing the air-solid interface. For the next generation solar cells, the structures with a scale comparable to the wavelengths of the majority of the useful solar spectrum are the ideal design (Zhu et al., 2010). Furthermore, with a nano-rod structured surface, the light can reflect multiple times and thus increase the photon absorption.

### **Electron-holes Generation and Separation**

In PEC cells, only semiconductor electrodes are useful because the lifetimes of excited states in metals are too short. Electron-hole pairs are generated when the semiconductor is illuminated with photons of energy larger than the band gap ( $E_g$ ) of a semiconductor. Electrons excited to energy levels far away from the band edges are thermalized within  $10^{-12}$ - $10^{-13}$  s. Hence, all light quanta with larger energy than  $E_g$  contribute only the band gap energy to the photo conversion. Therefore, to perform water splitting efficiently, the band gap of the material should be larger than 1.23 eV for conquering the unavoidable losses by entropy production (Nozik, 1978) but should be as small as possible to absorb solar energy efficiently. Thus, semiconductors with band gaps in the range 1.4-2eV are more useful than those of higher or lower bandgaps for the conversion of solar energy. For a p-type material, electrons, the minority charge carriers, that are generated in the depletion area and those generated within a diffusion length of the depletion region then diffuse into it, are separated by the built-in field and are swept to the semiconductor

surface. Thus, cathodic reduction is produced by combining the electrons with the positively charged ions ( $H^+$ ) reaching the semiconductor-electrolyte interface. On the other hand, the majority charge carriers, i.e. holes, are carried to the external circuit and participate in an anodic oxidation reaction at the counter electrode.

Not only the band gap of a material is important but the position of the band edges of semiconductor has to be correctly located relative to the redox Fermi levels of the water oxidation and reduction reactions respectively. A semiconductor with optimal properties for this purpose should therefore have the band edge positions which are shown in Fig. 2.3. This figure is designed for a p-type semiconductor and indicates also the course of the quasi-Fermi levels in the illuminated semiconductor electrode which is needed for the photoelectrolysis of water. The conduction band should be located at the electron energy higher than the water reduction potential; meanwhile, the valance band edge of the electrode should be located at the electron energy lower than the oxidation potential of water. Otherwise, the bias potential would be needed to trigger the reaction. This diagram also shows all the energy losses by charge separation (band bending) and by entropy production in the semiconductor (the distance between the quasi-Fermi levels,  $nE_f^*$  and  $pE_f^*$ , and the respective band edges) and in the electrode reactions. The overvoltages are indicated by the distances between the Fermi levels at the surface of the electrodes and the respective redox Fermi levels (chemical potential) in solution.

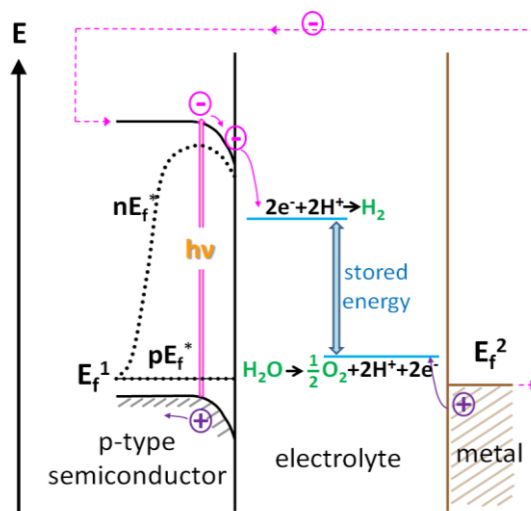


Figure 2.3. The band energy diagram of a p-type semiconductor cathode and a metal anode in electrolyte with illumination.

The band structures of both electrodes, involving the photocathode of a small band gap p-type semiconductor, such as CuO, and a metallic anode, such as Pt, at different stages in the formation of the electrochemical chain of the PEC, are shown schematically in Fig. 2.4. These figures show the band structure, illustrating various energy quantities, such as work function ( $\phi$ ), band levels of the electrodes before and after the chain is established, the potential of  $H^+/H_2$  and  $O_2/H_2O$  redox couples, band bending and electrical as well as photon potential. Fig. 2.4(a) shows the energy diagram before the galvanic contact is made between the two electrodes. The work function  $\phi$  is defined as the energy difference between the Fermi level and the energy level where electrons are free of electrostatic interaction ( $E=0$ ). As seen in Fig. 2.4(b), in the dark, the contact between the two electrodes results in charge transfer from the metal of lower work function to the p-type semiconductor of higher work function until the work functions of both electrodes have the same value. This charge transfer results in a change in the semiconductor

surface's electrical potential by  $V_B$ , leading to band bending. As seen in Fig. 2.4(c), the application of illumination results in the lowering of the surface potential of the photocathode by the generation of photovoltage ( $V_{ph}$ ). However, the  $O_2/H_2O$  potential still is below the  $E_f$  level of the anode. This energy relationship is not favorable for water decomposition. Consequently, Fig. 2.4(d) shows that the application of a bias voltage is required to lower the anode Fermi level,  $E_f^2$ , below the  $O_2/H_2O$  energy level, thus making the process of water decomposition possible.

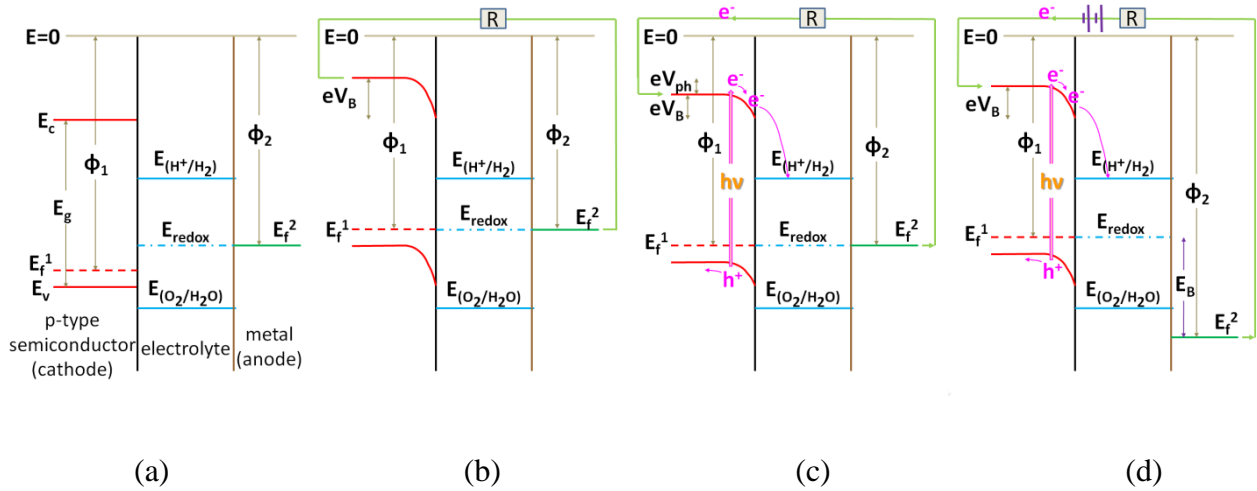


Figure 2.4. The band structures of both electrodes, involving the photo-cathode of a p-type semiconductor and metallic anode, at different stages in the formation of the electrochemical chain.  $\phi$  is the work function,  $E_c$ ,  $E_g$ ,  $E_v$  represent for conduction band energy, bandgap, valence band energy.  $V_{ph}$  is the generation of photovoltage and  $V_B$  is the semiconductor surface's electrical potential.

## Chemical Reaction

Ideal behavior for a  $p$ -type semiconductor electrode in the dark and under illumination is shown in Fig. 2.5. At the flatband potential,  $E_{fb}$ , there is no current, either in the dark or upon irradiation (region II). This is because there is no electric field to separate any generated charge carriers. At potentials more positive than the flatband potential (region I), an accumulation layer forms, and the electrode acts as an anode, both in the dark and upon irradiation. On the other hand, at potentials more negative than the flatband potential (region III), a depletion layer exists, and thus there is no current in the dark. However, upon illumination, the electrons generated at the photocathode, move to the cathode surface, resulting in the reduction of hydrogen ions into gaseous hydrogen. Simultaneously, the holes transfer to the anode via the external circuit, and gaseous oxygen evolves at the electrode surface.

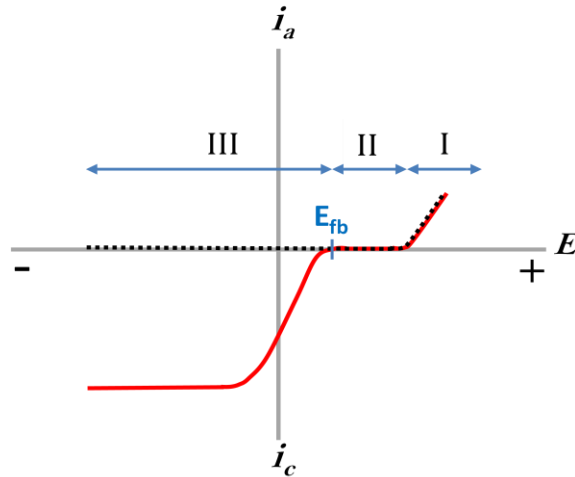


Fig. 2.5 Ideal behavior for a  $p$ -type semiconductor in the dark (black dot line) and under irradiation (red solid line).  $E_{fb}$  is flatband potential.  $i_a$  and  $i_c$  represent for anodic current and cathodic current.

### *Photoelectrochemical Systems*

Based on the basic PEC concept given above, several PEC systems have been studied: single photoelectrode, bi-photoelectrodes, hybrid photoelectrode, and sensitized photoelectrode systems. An example of the single photoelectrode is the well known TiO<sub>2</sub> photoanode demonstrated by Fujishima and Honda (1972), in which there is only one photoactive electrode while the other electrode is not light-sensitive. In order to increase the light absorbance and match the band structures to the water reduction and oxidation chemical potential, a bi-photoelectrode system based on a p-type photocathode and a n-type photoanode was thus developed (Nozik, 1976). The generated photo-voltage on both electrodes results in sufficient voltage for water decomposition without the application of a bias. Another way to increase the voltage is by embedding a photovoltaic cell (Morisaki et al., 1976; Khaselev and Turner, 1998) or some other photoactive layer (Gerischer, 1979; Miller et al., 2003) under the photoelectrode and such a system is called as hybrid photoelectrode. For both bi-electrode and hybrid photoelectrode systems, this allows a substantial increase of solar energy conversion (Nozik, 1976). The relatively later developed system concepts in PEC make use of either noble metals (Giordano et al., 1982; Zhao et al., 1996; Liao et al., 1998; Galinska and Walendziewski, 2005; Strataki et al., 2010) or dye (O'Regan and Grätzel, 1991; El Zayat et al., 1998; Wang et al., 2004; Chen et al., 2009; Laurence, 2011) to sensitize the photoelectrodes to boost the efficiency.



### 2.2.2 Difficulty and Approach

The properties of photoelectrodes should satisfy several specific requirements in terms of semiconducting and electrochemical properties, including band gap (discussed in the process section), transition type, flat band potential, Fermi energy, Schottky-type potential, electrical conductivity and resistance, microstructure, grain size, and corrosion. Also, the Helmholtz potential in the electrode/electrolyte interface and the electrolyte selection play an important role.

#### *Direct and Indirect Transition*

If the crystal momentums (k-vector in the Brillouin zone) of electrons and holes are the same in the maximal energy state in the valence band and the minimal energy state of the conduction band, the semiconductor is so called a direct band gap material and an electron can directly emit a photon with momentum conservation. However, in an indirect band gap material, the electron must pass through an intermediate state and transfer momentum to the crystal lattice by phonon (lattice vibration) before a photon can be emitted. This causes optical transitions to be much less likely in materials with indirect versus direct band gaps. For example, in some PEC candidate materials, such as  $\text{In}_2\text{O}_3$ , with  $E_g = 2.6$  eV, indirect intrinsic ionization requires higher energies than the band gaps (Nanthakumar and Armstrong, 1988). Therefore, these materials also are not suitable for photoelectrode applications. For  $\text{Fe}_2\text{O}_3$ , which also undergoes indirect transition, a much thicker layer would be needed in order to absorb the solar energy and this makes the film less flexible, and the thicker layer leads to charge transport problems as well.

### **Flat Band Potential**

As the p-type semiconductor electrode is immersed in the electrolyte, a downwards curvature of the semiconductor band potential forms in order to balance the difference Fermi levels in the electrode and the electrolyte. This curvature of the bands is equal to the flat band potential,  $U_{fb}$ , which is defined as its name, the potential needed to flatten the band (Seraphin, 1979; Chandra, 1985; Morrison, 1980). At the flat band potential, there is no net transfer of charge, and the Fermi energy lies at the same energy as the solution redox potential. For nonstoichiometric semiconductor compounds, this curvature is related to the segregation-induced surface charge and surface charge induced by the formation of chemisorbed species in the Helmholtz layer. The flat band potential is an important quantity in photoelectrode reactions. Specifically, the process of water photoelectrolysis may take place when the flat band potential is higher than the redox potential of the  $H^+/H_2$  couple (Seraphin, 1979; Chandra, 1985; Morrison, 1980; Bak et al., 2002). It is related to different phases and crystallographic orientations and can be engineered through the imposition of specific surface to bulk concentration gradient (Zhao et al., 1999; Kozuka et al., 2000).

### **Schottky-type Potential**

A Schottky barrier, a potential drop for p-type semiconductors, is commonly formed at the semiconductor/electrolyte interface due to the concentration gradients, surface states, and adsorption states. The formation of such a barrier can prevent the recombination of the photon-excited charge carriers. It can be formed by the imposition of the defect concentration gradients and of the aliovalent ion segregation (Nowotny, 1991; Nowotny,

1997; Adamczyk and Nowotny, 1986). Also, this potential barrier may be formed when there is a structural deformation due to the excess surface energy at the near-surface layer (Zhao et al., 1999; Zhao et al., 1999; Kozuka et al., 2000).

### **Fermi Energy (Chemical Potential of Electrons)**

The Fermi energy,  $E_f$ , a hypothetical level of an electron's potential energy in a crystalline solid as described in the Fermi-Dirac distribution function,  $\bar{n}_i$  (Eq. 2.4)

$$\bar{n}_i = \frac{1}{e^{(\epsilon_i - \mu)/kT} + 1} \quad (2.4)$$

where  $\epsilon_i$  is the energy of a single particle state  $i$ , and  $\mu$  is the chemical potential. The chemical potential is equal to the Fermi energy when  $T = 0$  K. As shown in the equation, the Fermi energy represents a state with a 50% probability of being occupied by an electron in the solid. Thus,  $E_f$  can be considered as the ability of a semiconductor to donate or accept electrons during chemical reaction and describes the electroactivity of a solid. Comparing the physical meaning of Fermi energy in a solid and the chemical potential for an electron which describes the chemical equilibrium, they essentially represent the same concept. Knowing the value of the Fermi level is essential to the quantitative evaluation of the reactivity of a solid whenever charge transfer takes place.

### **Electrical Conductivity and Resistance**

Electrical resistance reduced to a minimal level is essential for efficient charge transfer within the PEC cell. Consequently, this requires the resistance of all elements of the circuit, including electrolyte, electrical leads, electrical connection, measuring and

control equipment, and the most important of all, the electrode material, to be minimized. Since the electrical resistance of the semiconductor photocathode is several orders of magnitude larger than that of the metallic anode, the resistance of the semiconductor plays the most critical role in the cell's resistance. The resistivity of the electrode can be minimized through the modifications of defect disorder to increase the conductivity (Bak et al., 1997). Specifically, this could be achieved by changes in composition resulting in a change of defect charge, i.e. the incorporation of aliovalent cations, leaving an increase in electronic charge carrier concentration (Kofstad, 1972).

The electrical conductivity ( $\sigma$ ), the reciprocal of electrical resistivity, of the photocathode, which is determined by the concentration of the charge carriers and their mobility, is described in Eq. (2.5):

$$\sigma = en\mu_n + ep\mu_p + Z_i e i \mu_i \quad (2.5)$$

where  $n$ ,  $p$ , and  $i$  are the concentration of electrons, holes, and ions, respectively;  $\mu_n$ ,  $\mu_p$ , and  $\mu_i$  are the mobility of electrons, holes, and ion, respectively;  $Z_i$  is the charge number of ion. The ionic component of the electrical conductivity may be ignored at room temperature. At the interactions between the charge carriers are absent, the mobilities are not affected by the charge carrier concentrations. However, at higher concentrations, these interactions would lead to a decrease in the mobilities. Therefore, the maximal  $\sigma$  is a compromise between the effects of increasing charge carriers' concentrations while decreasing their mobilities.

An alternative method of reducing the resistance is through minimization of the thickness of the photoelectrode by fabrication of a thin film or minimization of the path for the

charge carriers' transport to the surface or back contact by utilizing a three dimensional current collector.

### **Microstructure**

The properties of polycrystalline solids are well known to be very sensitive to microstructure such as grain size and the concentration of grain boundaries. For grain size, the effect may be considered as the surface to volume ratio and the impact of the interfacial energy and the local defect chemistry. Theoretical studies provide the guideline in the effect of grain size on the band gap, as shown in Fig. 2.6 (Hoffmann et al., 1995). These data indicate that the band gap can be modified by varying the grain size. As the grain size decreases, a wider band gap is expected and thus might affect optical and electrical properties. Additionally, the local properties such as linear defects formed at the intersection between the external surface and the grain boundaries might also have an impact on the material properties. For example, grain boundaries may act as weak links for the charge transport in polycrystalline materials (Hirschwald et al., 1988; Nowotny, 1988; Nowotny, 1991; Nowotny, 1994). However, these grain boundaries also may act as recombination traps for charge carriers (Seraphin, 1979; Chandra, 1985).

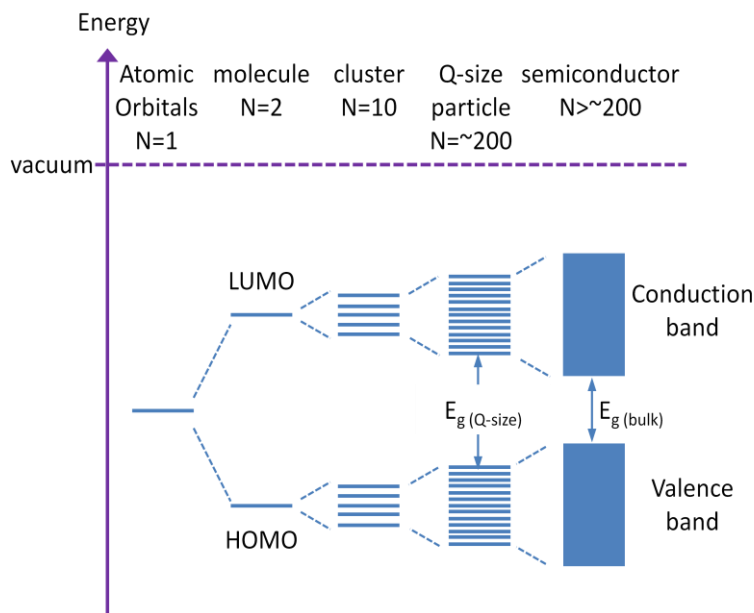
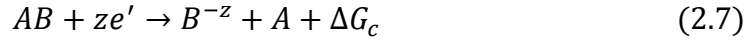
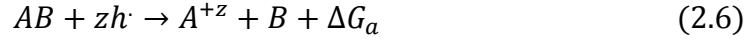


Fig. 2.6. Effect of particulate size on the electronic structure adopted from Hoffmann et al. (1995)

### Corrosion

An essential requirement for the photoelectrode is the resistance to electrochemical corrosion, photo-corrosion, and dissolution at the solid/liquid interface which would lead to the degradation of the material properties (Chandra, 1985; Morrison, 1980). Certain oxide materials, such as  $\text{TiO}_2$  and its solid solutions, are particularly resistant to these corrosions (Fujishima and Honda, 1972; Morisaki, 1976; Chandra, 1985; Bak et al., 2002; Fujishima et al., 1999). Therefore, they are suitable candidates for PEC water decomposition. In contrary, a large group of semiconductors (Khaselev and Turner, 1998; Licht et al., 2000), having suitable width of band gap and direct transition properties for solar energy conversion, are not resistant to corrosion, a process accompanied by charge transfer at the solid/liquid interface. The exposure of the electrode to aqueous

environments during the photoelectrochemical process results in the degraded properties. Such corrosion of an AB semiconductor leading to anodic and cathodic decomposition may be described by the following reactions:



where  $z$  is the number of electrons or holes;  $\Delta G_a$  and  $\Delta G_c$  are the free energy change at the anode and cathode, respectively.

The free enthalpies of the oxidation and reduction reactions per charge carrier are shown in the following equations,

$$E_{p,d} = \frac{\Delta G_a}{zN_A} \quad (2.8)$$

$$E_{n,d} = \frac{\Delta G_c}{zN_A} \quad (2.9)$$

where  $E_{p,d}$  and  $E_{n,d}$  are the free enthalpy of oxidation reaction and reduction reaction per charge carrier, i.e. hole and electron, respectively. The stability criteria of both photocathode and photoanode against electrochemical corrosion have been formulated by Gerischer (1979):

$$E(O_2/H_2O) < E_{p,d} \quad (2.10)$$

$$E(H^+/H_2) > E_{n,d} \quad (2.11)$$

where  $E(\text{H}^+/\text{H}_2)$  is the energy of the redox couple  $\text{H}^+/\text{H}_2$ ,  $E(\text{O}_2/\text{H}_2\text{O})$  the energy of the redox couple  $\text{O}_2/\text{H}_2\text{O}$ . Inequalities (2.10) and (2.11) correspond to the energy values on the electrochemical scale shown in Fig. 2.7 (Gerischer, 1979) along with the band gap ranges and energies of the redox couples ( $E_{p,d}$ ,  $E_{n,d}$ ) for a few semiconductors. In the figure, it can be seen clearly that  $\text{Cu}_2\text{O}$  is not stable for serving either photocathode or photoanode due to corrosion while  $\text{ZnO}$ ,  $\text{CdS}$ ,  $\text{GaP}$ , and  $\text{GaAs}$  can only serve as photocathodes.

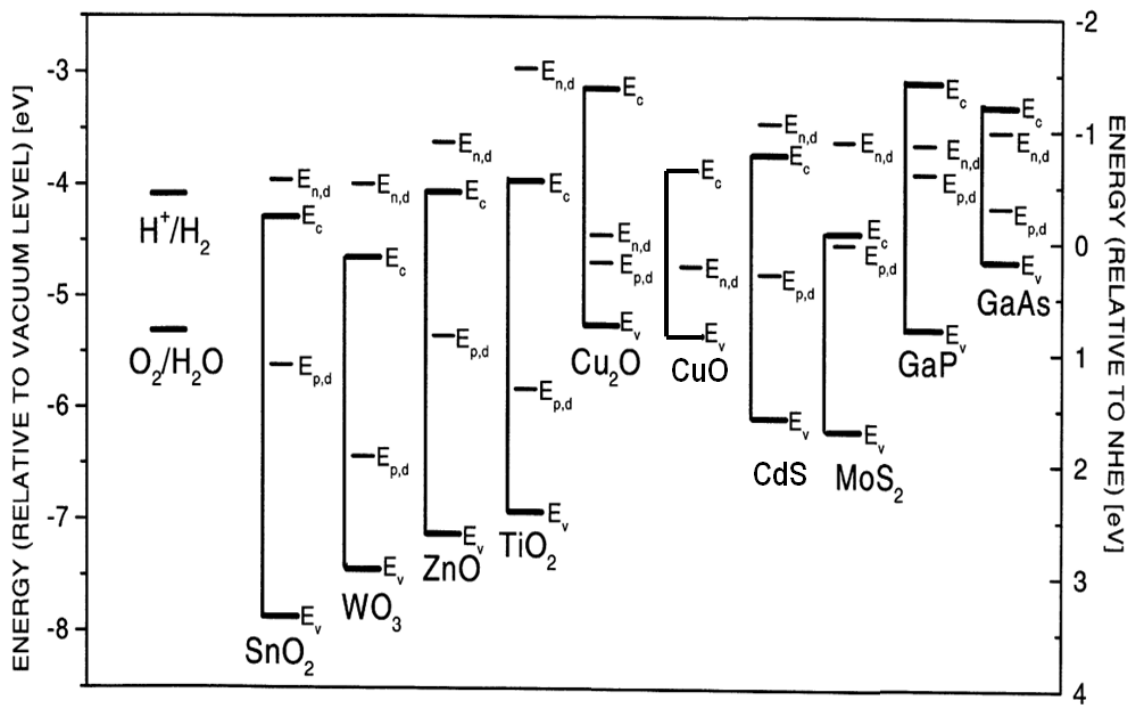


Figure 2.7. Position of decomposition potentials  $E_{n,d}$  and  $E_{p,d}$  vs.  $E_c$  and  $E_v$  of selected semiconductors (Gerischer, 1979).  $\text{CuO}$  information was calculated and added by Chiang.

All the information is based on pH7.



### *Helmholz Potential*

When a semiconductor material is immersed in a liquid, the charge transfer from the p-type semiconductor to the electrolyte leads to the formation of a surface charge and results in downwards band bending, forming a potential barrier. This surface charge is compensated by a charge of the opposite sign, which is induced in the electrolyte within a localized layer, known as the Helmholtz layer. It is ~1 nm thick and is formed of oriented water molecule dipoles and electrolyte ions adsorbed at the electrode surface (Chandra, 1985; Finklea, 1988; Gerischer, 1979). The height of this potential barrier, known as the Helmholtz barrier, is determined by the nature of the electrolyte and the surface properties of the photoelectrode and may be modified through surface engineering of the electrode.

### *Electrolyte*

Selection of optimal ions and their concentrations, leading to maximum mobility can maximize the conduction of the electrolyte, where the relationship between the ionic conductivity and ionic mobility is shown in Eq. 2.12.

$$u = \frac{\lambda^o}{F} \quad (2.12)$$

where  $u$  is the ionic mobility and  $\lambda^o$  is the ionic conductivity and  $F$  is the Faraday constant.  $H^+$  and  $OH^-$  have the highest ion conductivities, i.e. 349.65 S cm<sup>2</sup>/mole and 198 S cm<sup>2</sup>/mole for  $H^+$  and  $OH^-$ , respectively. However, using high concentration of  $H^+$  and  $OH^-$  is problematic owing to their chemical aggressiveness. Alkaline cations, such as  $K^+$  (73.48 S cm<sup>2</sup>/mole) and  $Ba^{2+}$  (63.6 S cm<sup>2</sup>/mole), and anions, such as  $Cl^-$  (76.31 S

$\text{cm}^2/\text{mole}$ ), are alternative candidates because of their relatively high conductivities and assume minimal resistances at concentrations between 3 and 4 M. More information on ion conductivities can be found in the book, Physical Chemistry (Laidler et al., 2003).

### **2.3. MATERIALS FOR PEC**

The commonly used PV cell material, Si, is not an optimal candidate for PEC hydrogen generation due to its insufficient band gap, i.e. 1.1 eV, shown in Fig. 2.8 and the stability issue. Other semiconductor candidates such as GaAs, CdTe and CdSe, though having suitable band gap, are barely attractive because of the elemental toxicity and the accompanied environmental issues during synthesis and disposal process. Thus the low cost, low toxicity and earth abundant metal oxide semiconductors are attractive. The studies based on the metal oxides can simply be grouped into two: large band gap but stable material such as  $\text{TiO}_2$  and small band gap material but not as stable material such as  $\text{Cu}_2\text{O}$  and  $\text{CuO}$ . The following sections review the materials aspects of these two groups.

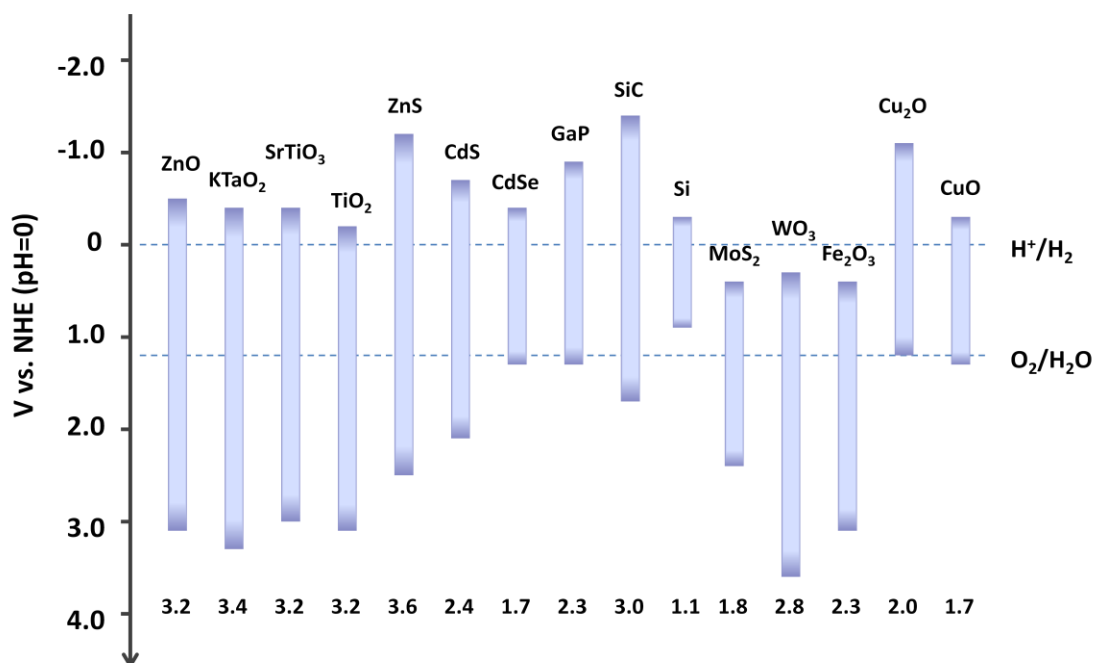


Figure 2.8. Band gap energies and relative band positions of different semiconductors related to water oxidation/reduction potential (vs.NHE) at pH=0. (Information of ZnO to Fe<sub>2</sub>O<sub>3</sub> are adopted from Navarro Yerga et al., 2009, Cu<sub>2</sub>O are adopted from Gerischer, 1978, and CuO are adopted from Chiang et al., 2012d)

### 2.3.1. Wide Band Gap Materials

The most widely studied material for the PEC water splitting is TiO<sub>2</sub> because of its stability in the electrolyte and its resistivity to photocorrosion. However, it is also well known to have a wide band gap (3.0-3.2 eV) and thus it is insufficient with respect to absorbing visible light. As a result, early work was focused on adding an intermediate band to enhance the light absorbance by using metallic dopants such as V<sup>5+</sup>, Cr<sup>3+</sup>, Fe<sup>3+</sup>, Co<sup>2+</sup>, Ni<sup>2+</sup>, and Ru<sup>3+</sup> (Anpo and Takeuchi, 2003; Konta et al., 2004; Hwang et al., 2005). The energy levels of aliovalent ions doped in rutile TiO<sub>2</sub> lattice are shown in Fig. 2.9

(Mizushima et al., 1972; Mizushima et al., 1979; Bak et al., 2002). These dopants also modify the interfacial charge transfer and electron-hole recombination behavior of  $\text{TiO}_2$  (Hoffman et al., 1995; Linsebigler et al., 1996; Bui et al., 2011). Another method to increase the visible light absorbance is by reacting  $\text{TiO}_2$  with other metal oxides such as  $\text{SrO}$ ,  $\text{BaO}$ ,  $\text{Ln}_2\text{O}_3$ , and metal titanates with intermediated band gaps are thus obtained. Among these titanates,  $\text{SrTiO}_3$  (Kato and Kudo, 2002; Ishii et al., 2004),  $\text{La}_2\text{Ti}_2\text{O}_7$  (Uno et al., 2005; Naoyuki et al., 2010), and  $\text{TiSi}_2$  (Ritterskamp et al., 2007) have received the most attention.

The surface modification by an organic dye also helps to increase the light absorbance. Populating the conduction band of wide band gap semiconductors with electrons under visible light by exciting a chromophore such as porphyrins,  $\text{Ru}(\text{bipy})_3^{2+}$  derivatives, and  $\text{Fe}(\text{CN})_6^{4-}$  is also an effective strategy (Hagfeldt and Grätzel, 1995; Kalyanasundaram and Grätzel, 1998; Qu and Meyer, 2001). Other metal oxides such as the corner-sharing structure  $\text{MO}_6$  ( $\text{M}=\text{Ta}$ ,  $\text{Nb}$ ), and the highly UV irradiation sensitive  $\text{MTaO}_3$  ( $\text{M}=\text{Li}$ ,  $\text{Na}$ ,  $\text{K}$ ), and the scheelite structure  $\text{BiVO}_4$  and perovskite structure  $\text{Ag}_3\text{VO}_4$  also showed photocatalytic activity. More detailed reviews of these wide band gap materials can be found in the literature (Bak et al., 2002; Krishnan, 2007; Navarro Yerga et al., 2009).

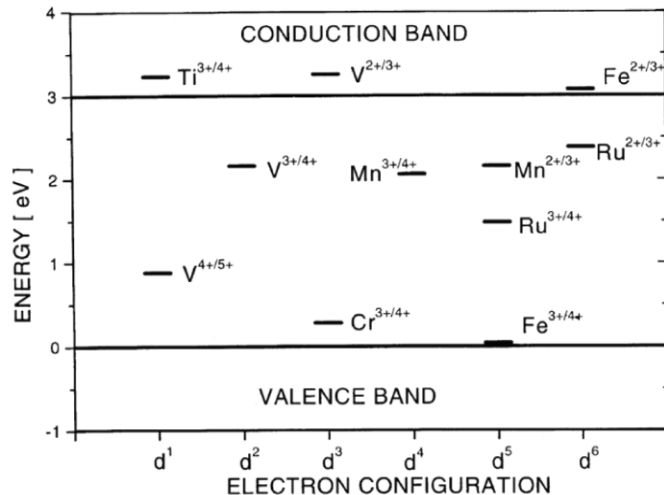


Figure 2.9. Energy levels of aliovalent ions in rutile  $\text{TiO}_2$  lattice. (Mizushima et al., 1972; Mizushima et al., 1979; Bak et al., 2002)

### 2.3.2. Small Band Gap Materials

Materials with band gap ranging from 1.3-2.0 eV are able to absorb sun light efficiently. These materials include p-type CuO (1.3-1.7 eV),  $\text{CaInP}_2$  (1.8-1.9 eV), and  $\text{Cu}_2\text{O}$  (2.0-2.2 eV). However, they either need bias potential to drive the water splitting reaction (Kocha et al., 1991; Kocha and Turner, 1995) or are not stable in the electrolyte under solar irradiation (Hardee and Bard, 1977; Gerischer, 1979; Koffyberg and Benko, 1982). Because of these limitations, compared to the stable  $\text{TiO}_2$  electrodes, only a few studies are focused on these materials.

A recent published paper (Paracchino et al., 2011) address this stability issue by deposition of a thin layer of a stable material, i.e.  $\text{TiO}_2$ , on top of  $\text{Cu}_2\text{O}$  film electrode and thus keeps the electrode at about 78% of the initial activity after 20 min PEC test under

illumination at 0 V (vs. NHE). In another newly published study (Zhang and Wang, 2012), researchers took CuO as a protective layer for preventing Cu<sub>2</sub>O from photocorrosion and the photoactivity is demonstrated to have 74% of initial photoactivity after 20 min of illumination, compared to 30% for a bare Cu<sub>2</sub>O electrode. These all demonstrate the possibility of coating a protective layer to enhance the stability of a small bandgap material. Thus the next issue remaining is how much photocurrent these small band gap materials can generate!

#### **2.4. COPPER OXIDE PROPERTIES**

Copper (II) oxide or cupric oxide (CuO), a black solid, is also known as tenorite. It is a basic oxide, so it dissolves in mineral acids such as H<sub>2</sub>SO<sub>4</sub>, HCl, and HNO<sub>3</sub>. CuO belongs to the monoclinic crystal system and the lattice parameters are  $a = 4.6837$ ,  $b = 3.4226$ ,  $c = 5.1288$ ,  $\alpha = 90^\circ$ ,  $\beta = 99.54^\circ$ ,  $\gamma = 90^\circ$ . Its crystal structure is shown in Fig. 2.10. As shown in the figure, Cu forms four coplanar bonds with O (Forsyth and Hull, 1991).

CuO is an intrinsic p-type semiconductor, and it keeps p-type character even with Al<sup>3+</sup> doping (Ohya et al., 2000). Other dopants such as Fe<sup>2+</sup>, Fe<sup>3+</sup>, Zn<sup>2+</sup>, Mn<sup>x+</sup>, and Li<sup>+</sup> have been added for the studies of ferromagnetism (Borzi et al., 2000; Fan et al., 2005; Saito et al., 2003) and conductivity (Ohya et al., 2000; Saito et al., 2003).

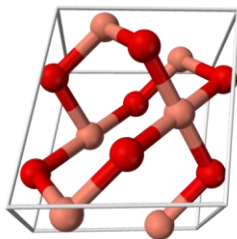


Figure 2.10. Crystal structure of CuO (Forsyth and Hull, 1991).

As mentioned before, CuO is a basic oxide which is not stable in an acidic environment as demonstrated in the Pourbaiz diagram (Steigerwald et al., 1995). The dash lines with notation (a) and (b) represent for the water reduction and oxidation potential, respectively, which varies based on the pH of solution. Based on the band edges of CuO reported in the literature, the reduction potentials of CuO to Cu<sub>2</sub>O and to Cu lie in the gap, and thus CuO might not be stable when there is a highly energetic electron generated by a photon.

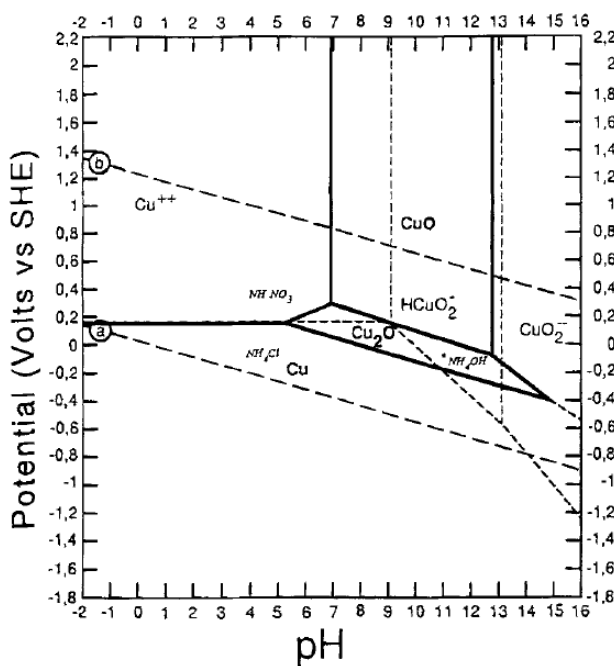


Figure 2.11. pH-potential diagrams (Pourbaix diagram) for the Cu-H<sub>2</sub>O system. (Steigerwald et al., 1995)

## 2.5. NANODESIGN FOR COPPER OXIDE PHOTOCATHODES

Based on the concept discussed above, it can be concluded that if the electrons generated in the bulk of CuO from absorbed irradiation can reach the electrode/electrolyte interface during their lifetime and manage to find the  $H^+$  at the surface for the water reduction reaction, then water electrolysis by a p-type CuO electrode based on the PEC concept can be very efficient. For this reason, the generation and separation of photo-excited charge carriers with a low recombination rate is an essential condition for the PEC materials. The transport of photo-induced charge carriers is determined by the surface properties, crystal size, crystalline structure, the nature and number of defects in the CuO electrode. In order to have efficient photo-excited charge carrier dynamics, the particle size is expected to be smaller than the diffusion length of photo-excited charge carriers (Ashokkumar, 1998), i.e. tens of nanometer to few micrometers. Therefore, the chance of photo-excited electrons reaching the interface increases as the particle size of CuO decreases. Meanwhile, a high degree of crystallinity of CuO particles has a positive impact on transport of the charge carriers while the density of grain boundary and surface defects have negative effects. Apart from controlling the nanocrystalline size, the construction of the three-dimension network serving as the current collector is also an important aspect which can improve the charge carrier separation efficiency. As a result, the following chapters are focused on the processes such as flame spray pyrolysis and wet chemical method production that can produce nanocrystalline CuO particles as well as the effects of film morphologies on PEC. Finally, a three-dimensional bio-template current collector based process will be included.



## Chapter 3

### Copper Oxide Nanoparticle Made by Flame Spray Pyrolysis for Photoelectrochemical Water Splitting – CuO Nanoparticle Preparation

The results presented in this chapter have been published in the following journal article:

Chiang, C. Y.; Aroh, K.; Ehrman, S. “Copper Oxide Nanoparticle Made by Flame Spray Pyrolysis for Photoelectrochemical Water Splitting – Part I. CuO Nanoparticle Preparation” *Int. J. Hydrogen Energ*, **2012**, 37, 4871-4879.

#### 3.1. ABSTRACT

Copper oxide (CuO) semiconductor nanoparticles are of interest because of their promising use for electronic and optoelectronic devices, and the size of the CuO particles for these applications is important. In this work, near spherical CuO nanoparticles with aspect ratio of 1.2-1.3 were made by a flame spray pyrolysis (FSP) method. In FPS, flame temperature, residence time, precursor concentration can be used to control particle size. As the precursor concentration increased from 0.5% to 35% w/w, primary particle diameter increased from  $7\pm 2$  to  $20\pm 11$  nm. Larger primary particle diameters were observed in the low gas flow system (set B) due to the long residence time in the high temperature zone. For the dependence of temperature on particle diameter, particles grew to similar diameter, i.e.  $\sim 11$  nm, in both flame conditions within the hot temperature zone (80% of melting point of CuO) but for particles having longer residence time, i.e. 550 ms in set B, the standard deviation of particle diameter is 45% larger than for particles with

66 ms as residence time in set A. Modeling gave a result for CuO final particle diameter, based on collision/sintering theory with sintering by solid state diffusion, of 6.7 and 9.0 nm for set A and set B, respectively, with surface tension assumed to be  $0.5 \text{ J/m}^2$ . Comparison with the experiment results,  $11 \pm 4$  nm diameter for both flame conditions, indicates the simulations were reasonable.

### **3.2. INTRODUCTION**

Copper oxide (CuO) semiconductor materials have been particularly interesting because of their promising use for electronic and optoelectronic devices, such as electrochemical cells (Poizot et al., 2000; Morales et al., 2005), gas sensors (Katti et al., 2003; Cruccolini et al., 2004; Frietsch et al., 2000), magnetic storage media (Fan et al., 2004), solar cells (Larsson et al., 1996; Gao et al., 2004; Chowdhuri et al., 2004), field emitters (Hsieh et al., 2003; Chen et al., 2003), high-T<sub>c</sub> superconductors (Wu et al., 1987; Dai et al., 2000), nanofluid (Chang et al., 2011), and catalysts (Jiang et al., 1998; Reitz and Solomon, 1998; Carnes and Klabunde, 2003; Santos et al., 2005; Shah et al., 2009). However, for these applications, the size, morphology, and specific surface area of the CuO particles are very important, and sometimes are strongly dependant on the preparation methods.

Nanoparticles are distinguished from bulk materials due to their high surface area to volume ratio which causes the structural and electronic changes. A decrease in size invariably leads to sharpening of the energy bands and also leads to discretization of electron energy levels, concentration of oscillator strength, highly polarizable excited

states, increased electron-electron correlation etc. Investigations have revealed that CuO nanocrystals show distinct structural, chemical bonding (Borgohain et al., 2000) and electronic characteristics (Fan et al., 2006) due to quantum size effects.

For a number of applications, the characteristics of inorganic particles must be tailored through control during preparation. Many methods are available to prepare micron size CuO particles, such as metal-organic chemical vapor deposition (MOCVD) for producing CuO with grain diameters from 0.05 to 0.8 micrometer (Condorelli et al., 1999) and sonochemical synthesis for producing CuO of grain size varying from 10 nm to several microns (Vijayakumar et al., 2001). For preparing nano-sized CuO, some results have been published such as crystallites in the size range of 7-9 nm (Carnes et al., 2002) and 1-10 nm diameter particles (Eliseev et al., 2000) by sol-gel techniques, average diameter of 15-20 nm CuO nanoparticles by solid state reaction (Jia et al., 1998; Wang et al., 2004), CuO with diameter as small as 4 nm by electrochemical method (Borgohain et al., 2000), controllable diameters of 3 to 9 nm by alcohothermal decomposition of copper acetate (Hong et al., 2002), diameters between 3 and 5 nm by colloid-thermal synthesis processing (Son et al., 2006), primary particles of copper oxide about 20-30 nm by spinning disk reactor (Chang et al., 2011).

Although there are many methods available for producing small CuO particles, many are time consuming (Condorelli et al., 1999; Zhang et al., 2006), energy intensive (Jia et al., 1998; Vijayakumar et al., 2000; Wang et al., 2004), and require expensive raw materials (Borgohain et al., 2003; Vijayakumar et al., 2001; Zhang et al., 2006) which make them difficult to be scaled up. Economic concerns dictate that a relatively low cost, easy to operate, and scalable process would be needed. Flame-based aerosol methods have been

developed for the synthesis of a wide variety of metal oxide particles (Ehrman and Friedlander, 1999; Pati et al., 2009; Camenzind et al., 2010). Compared to the various post-treatment steps needed in wet-chemical routes, gas-phase processes allow the preparation of the desired material often without any further post-processing (Camenzind et al., 2005; Chang et al., 2006; Strobel et al., 2006). Furthermore, flame-based aerosol methods also have potential commercial importance because they can be conducted continuously with a high production rate at a relatively low cost (Pratsinis, 1998; Kammler et al., 2001; Jang, 2001).

Flame synthesis is a novel technique for producing fine and pure particles in the as-prepared state in just few milliseconds. However, the produced particles are generally hard agglomerates and the size distribution is somewhat broad, making them undesirable for many applications (Pratsinis, 1998; Jang, 2001). The preparation of nonaggregated particles by methods using flames with liquid precursor sources, i.e. flame spray pyrolysis, has been reported (Kang et al., 2002; Chang et al., 2004). Flame spray pyrolysis (FSP) is a flame-assisted liquid droplet-vapor-to-particle conversion process used to produce single and multi-component nanoparticles (Windeler et al., 1997; Ehrman and Friedlander, 1999; Limaye and Helble, 2002; Mädler et al., 2002; Tani et al., 2004; Jang et al., 2007; Pati et al., 2009; Camenzind et al., 2010). In addition, the FSP setup allows the adjustment of precursor compositions, flame temperature, production rate, and residence time of particles in the flame and hence particle growth and morphology can be controlled, leading to tailor-made single or multicomponent nanocomposite particles.

In this study, several ways to control and vary the size of nano CuO particles are explored and evaluated. Particle size was changed by varying the precursor concentration. With lower precursor concentration, loading of aerosol decreases and the collision rate is slower. Also, the effect of quenching rate on crystalline size was studied by introducing liquid nitrogen into the post flame zone. Furthermore, the temperature of flame and the residence time of particle in high temperature zone were considered and modeling based on sintering/collision theory was compared with the experimental results.

### **3.3. MATERIALS AND METHODS**

#### **3.3.1. Aerosol Generator and Flame Conditions**

In an FSP reactor, an aqueous solution of copper (II) nitrate,  $[\text{Cu}(\text{NO}_3)_2 \cdot 3\text{H}_2\text{O}]$ , (Strem Chemicals, Inc. USA) was atomized by a nebulizer (Gemini Scientific Corp., USA) and passed through a premixed methane flame where vaporized precursor reacted to oxide and formed nanosized CuO particles through gas to particle conversion. Particles then were collected on a polytetrafluoroethylene (PTFE) fabric filter (W. L. Gore & Associates Inc., USA) within a filter funnel (Whatman, Japan) using a vacuum pump (United Vacuum, USA). A schematic of the experimental apparatus for producing copper oxide aerosol from metal salt precursor is shown in Fig. 3.1. The liquid nitrogen was introduced to the system at varying distances from the flame by changing the height and angle of the liquid nitrogen bottle also as shown in Fig. 3.1.

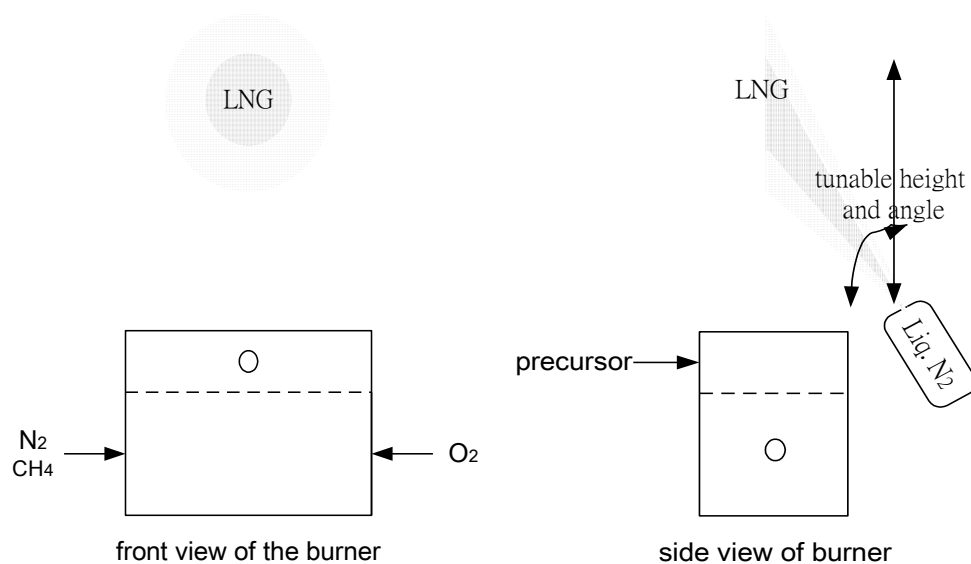
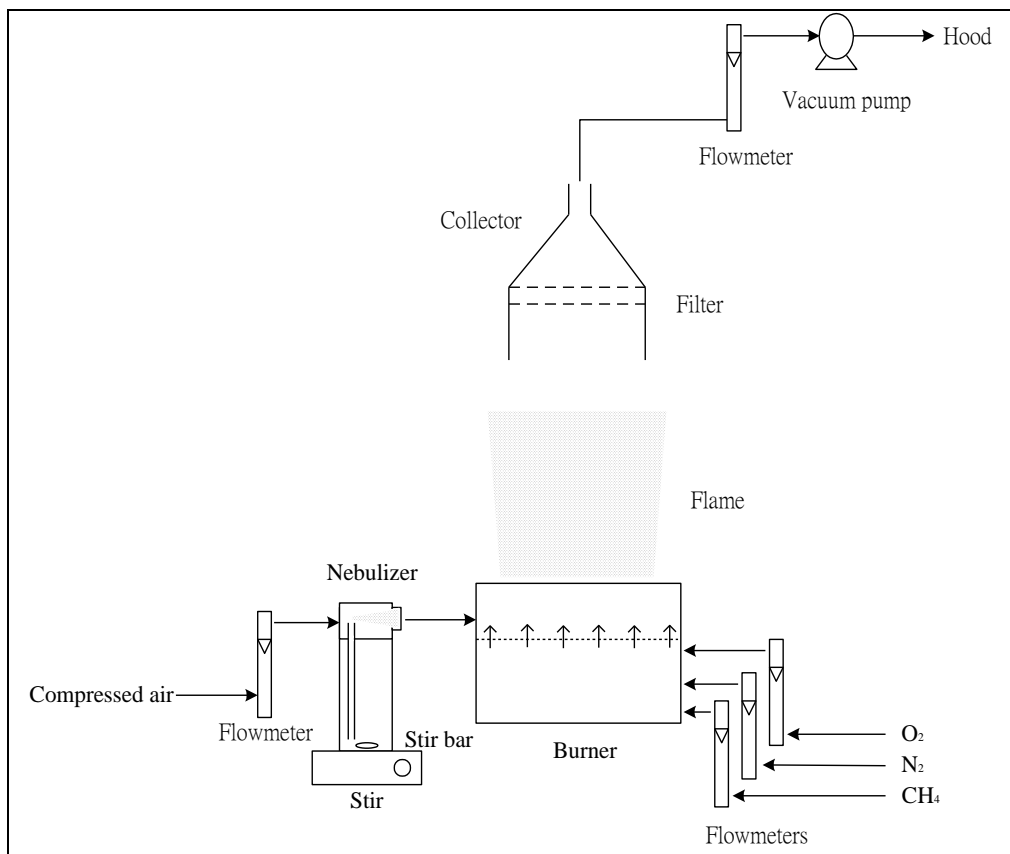


Figure 3.1. Schematic of the apparatus for the flame spray pyrolysis system.

The filtered laboratory air at 3.6 L/min flowed through a nebulizer atomizing precursor solution. Gas flow rates were controlled by rotometers (Cole-Palmer, USA). Both gas flow rates and flame conditions are tabulated in Table 3.1.

Table 3.1. Flame composition and characteristic.

Flame set	Gas flow rate (L/min)					Adiabatic flame temperature (K)	Maximum measured temperature (K)	Residence time $\tau^{**}$ (ms)
	CH <sub>4</sub>	O <sub>2</sub>	N <sub>2</sub>	air	Q <sub>G</sub> *			
A	1.2	2.4	10.2	3.6	13.8	2185	1748	55
B	0.6	0.4	1.5	3.6	6.1	2383	1432	660

\* Q<sub>G</sub>: total gas flow rate

\*\* Residence time in the high temperature zone (80% of CuO melting point)

The flame was made from methane (99.0%, Airgas) and oxygen (99.8%, Airgas) at an equivalence ratio of 1.0. To stabilize the flame, nitrogen (99.998%, Airgas) was introduced. The methane, oxygen and nitrogen were combined at the bottom of the burner then the mixture flowed upward through holes on the aluminum foil while the stream with air/droplets was introduced into the upper part of burner and mixed. The flat flame was stabilized on two parallel stainless steel plates. The temperature profile was measured at the middle of flame with an S-type thermocouple and corrected for radiation losses (Bradley and Matthews, 1968). Two different flame compositions and temperature profiles were chosen (Fig. 3.2) based upon the limits of our system. For set A, the maximum measured temperature was 1748 K with a cooling rate of approximately 209 K

per centimeter over the first 6 cm downstream, 54 K per centimeter from 6 to 10 cm, and 14 K per centimeter from 10 cm to the collector. For set B, the maximum measured temperature was 1432 K with a cooling rate of approximately 168 K per centimeter over the first 4 cm downstream, 109 K per centimeter from 4 to 8 cm, and 9 K per centimeter from 8 cm to the collector. The adiabatic flame temperatures calculated for the flame were 2185 K and 2383 K, respectively. The difference between the maximum measured temperature and the adiabatic flame temperature could be attributed to heat losses to the stainless steel cover and the evaporation of water.

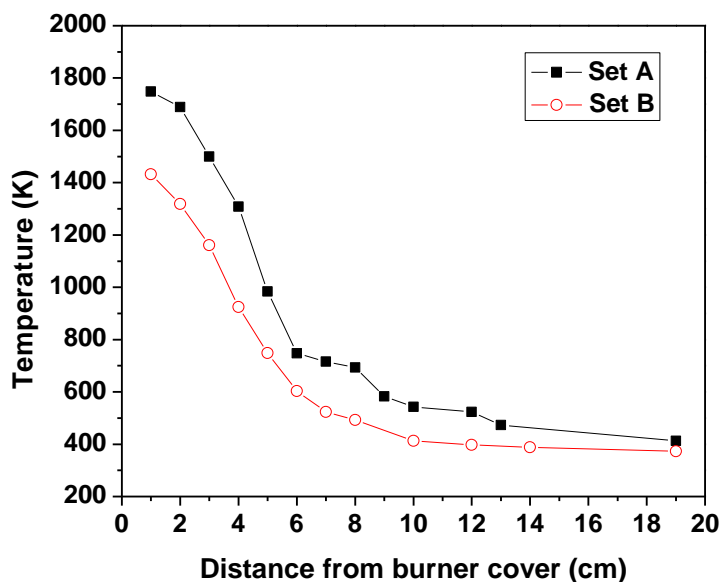
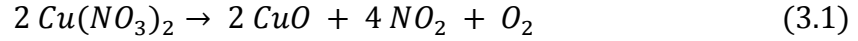


Figure 3.2. Temperature profile of the both flames.

The copper (II) nitrate (Strem Chemicals, Inc. USA) precursor solutions were prepared in the concentrations of 0.5%, 5%, 17%, 25%, and 35% w/w copper nitrate/solution with DI



water as solvent. Decomposition of copper nitrate in the flame is expected to follow the mechanism given in Eq. 3.1.



### 3.3.2. Particle Sampling and Characterization

For phase determination, X-ray diffraction (XRD) measurements were performed using a Philips PW 1800 diffractometer with a graphite monochromator and with Cu  $K_\alpha$  ( $\lambda=1.54 \text{ \AA}$ ) as the incident radiation. The particle morphology was studied via a transmission electron microscopy (JEM 2100 LaB6 TEM, Japan), operated at 200 kV. The CuO nanoparticles were collected onto a carbon-coated copper grid (Ted Pella, Inc.) for TEM analysis based on different experimental conditions. Also, particle diameters and size distributions were determined by counting at least 300 particles per sample and recording their average diameter from the TEM images.

For determining the average grain size, the Scherrer equation (Eq. 3.2) (Alexander and Klug, 1920) was chosen.

$$\tau = \frac{K\lambda}{\beta \cos \theta} \quad (3.2)$$

where  $\tau$  is the mean crystallite dimension,  $K$  is the shape factor,  $\lambda$  is the x-ray wavelength, typically  $1.54 \text{ \AA}$ ,  $\beta$  is the line broadening at half the maximum intensity (FWHM) in radius and  $\theta$  is the Bragg angle. The dimensionless shape factor has a typical value of about 0.9, but varies with the actual shape of the crystallite. Peaks with  $2\theta$  of  $32.57^\circ$ ,  $35.59^\circ$ ,  $38.85^\circ$ , and  $48.80^\circ$  were taken for this calculation.

## 3.4. RESULTS AND DISCUSSION

### 3.4.1. Experiment

Particles produced in the system were confirmed to be CuO based on XRD analysis and shown in Fig. 3.3. These CuO particles were nearly spherical with aspect ratio of 1.2-1.3. The aspect ratio was determined by the ratio of the longest and shortest line that bisects the area.

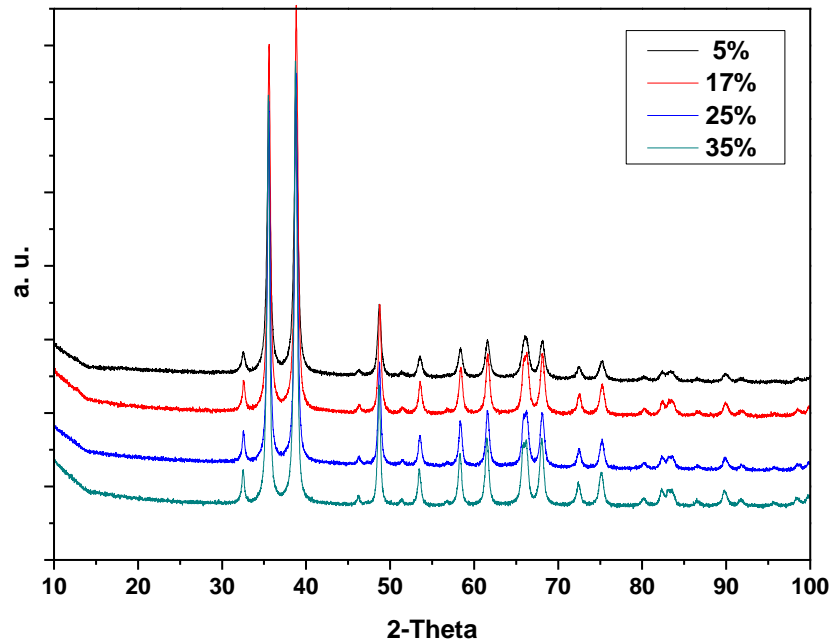


Figure 3.3. XRD for particles based on different precursor concentrations.

The precursor concentration effect on particle size was listed in Table 3.2. As the precursor concentration increased, primary particle size increased. However, as the concentration reached to a certain level, the concentration effects on primary particle size

were not as obvious as at lower concentration sets, i.e. 5% and 0.5%. The volume loading, volume of aerosol/total volume, reduced from  $1.28 \times 10^{-10}$  to  $1.83 \times 10^{-12}$  from concentration 35% to 0.5% w/w, which was two orders of magnitude lower, thus led to much smaller particle diameter.

Table 3.2. Precursor concentration vs particle size, for flame set A.

Precursor concentration (w/w %)	Size ( by FWHM) (nm)	Number mean Particle diameter (nm)	Standard deviation (nm)
35	34	19.0	11.4
25	29	20.6	11.8
17	28	18.0	9.3
5	18	12.1	6.5
0.5	5	7	1.8

Furthermore, variation of particle diameter in each sample was observed in transmission electron micrographs of copper oxide shown in Fig. 3.4. This variation may be attributed in the variation of temperature in the flame (Ehrman and Friedlander, 1999). Based on image analysis of the TEM images, the particle size distributions of particles prepared at different precursor concentrations are given in Fig. 3.5, and an apparent dependence of particles size on the precursor concentration was found.

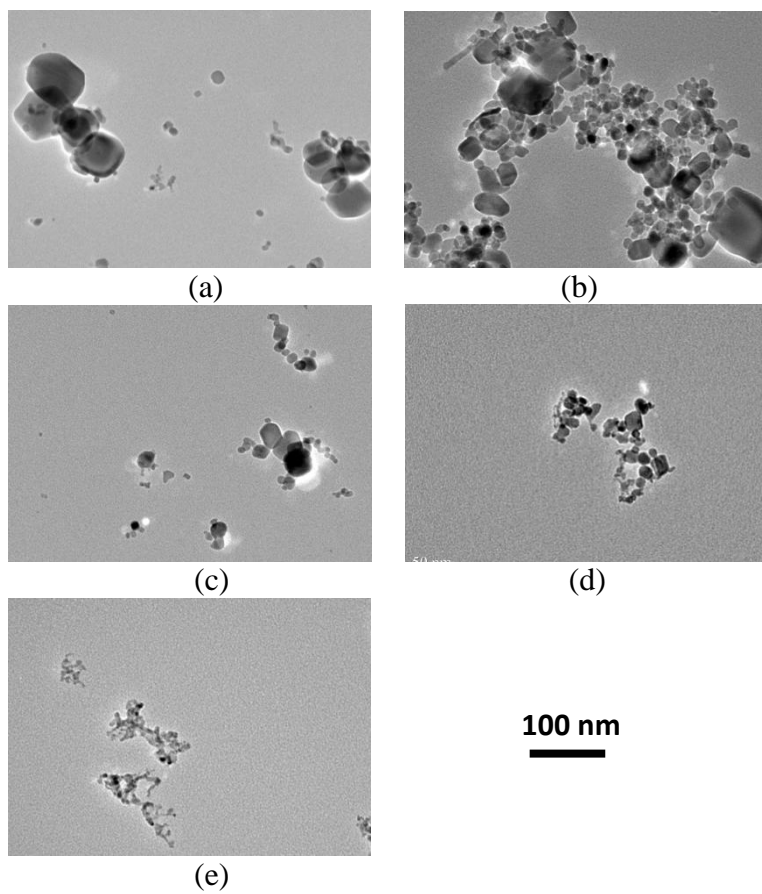


Figure 3.4. TEM micrograph for particles based on different precursor concentrations: (a) 35%, (b) 25%, (c) 17%, (d) 5%, and (e) 0.5%.

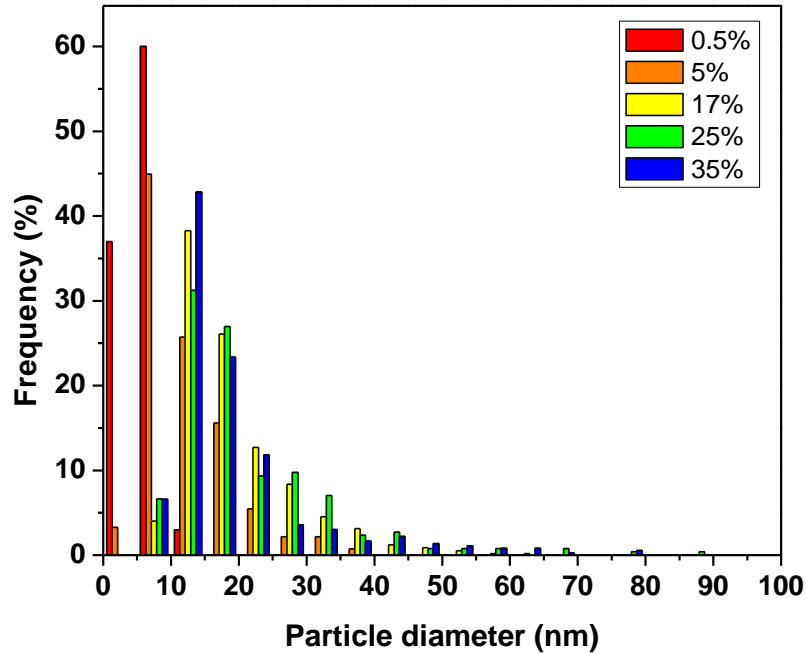


Figure 3.5. Particle size distribution based on different precursor concentrations.

In order to understand the flame condition effects on particle size, both 17% and 35% precursors were chosen for both flames. The result is tabulated in Table 3.3. Primary particle diameter were observed to be larger in set B because the particle residence time in the high temperature zone (above 1180 K, 80% of the melting temperature of CuO), i.e. 5 cm for set A and 3 cm for set B, was much longer due to the lower gas flow rate (the residence time was shown in Table 3.1). Also, in set B, with greater residence time in the high temperature zone, the particle size distribution was slightly broader for both 17% and 35% precursor concentrations.

Table 3.3. The comparison of flame A and B at precursor concentration of 17% and 35%.

Precursor concentration (w/w %)	Set A		Set B	
	Number mean diameter (nm)	Standard deviation (nm)	Number mean diameter (nm)	Standard deviation (nm)
35	19.0	11.4	21.4	12.1
17	18.0	9.3	21.3	10.5

Time temperature history is an important factor for governing formation and growth of nanoparticles in an FSP system (Wu et al., 1993). Thus, average primary particles sizes and their standard deviations of samples collected at varying heights (at least three times per condition) above the burner cover (related to residence time) were studied and are tabulated in Table 3.4.

Table 3.4. Particle size based on both flames and heights from the burner cover for 17% precursor.

Height above burner cover (cm)	Set A		Set B	
	Number mean Particle diameter (nm)	Standard deviation (nm)	Number mean Particle diameter (nm)	Standard deviation (nm)
1	9.2	3.0	14.2	3.9
2	9.0	1.8	15.0	5.5
4	11.4	3.8	11.4	6.5
6	11.5	4.4	18.1	11.0
10	14.8	7.8	19.2	11.6
19	18.0	9.3	21.3	10.5

In set A, particles grew very fast in the very first few centimeters because that was the high temperature zone which particles grew by coalescence and less aggregation of particles was observed (as shown in Fig. 3.6). In contrast, the diameter of the particles that were obtained at flame set B was larger at the first two centimeter then shrunk to 11 nm and started to grow after that. This might be due to the evaporation of solvent and decomposition of the copper nitrate salt. After a period of time, the particles formed copper oxide then started to coalesce with each other, increasing the size of the particles. Also, as particle grew larger, the particle size distribution also became broader as shown in Fig. 3.7. This might be explained by the difference in the number of times that particles can possibly collide, thus leading to a broader size distribution. With a further analysis of particle size depending on temperature, particles grew to similar size, i.e. ~11 nm in diameter, in both flame conditions within the high temperature region. This might imply the importance of temperature in coalescence dominated zone is more than time. However, for the temperature ranging from 1180 K to 500 K, i.e. 5-12 cm for set A and 3-7 cm for set B, particles grew much faster in flame B due to the longer residence time in the high temperature region. Considering particle growth as a function of residence time, particles tended to have broader size distribution if they have longer residence time which represented that there would be more chance to coalesce under higher temperature. For example, particles were about 11 nm when the temperature was at 1180 K, but for set B with longer residence time, the standard deviation of particle size is 45% larger than for set A.

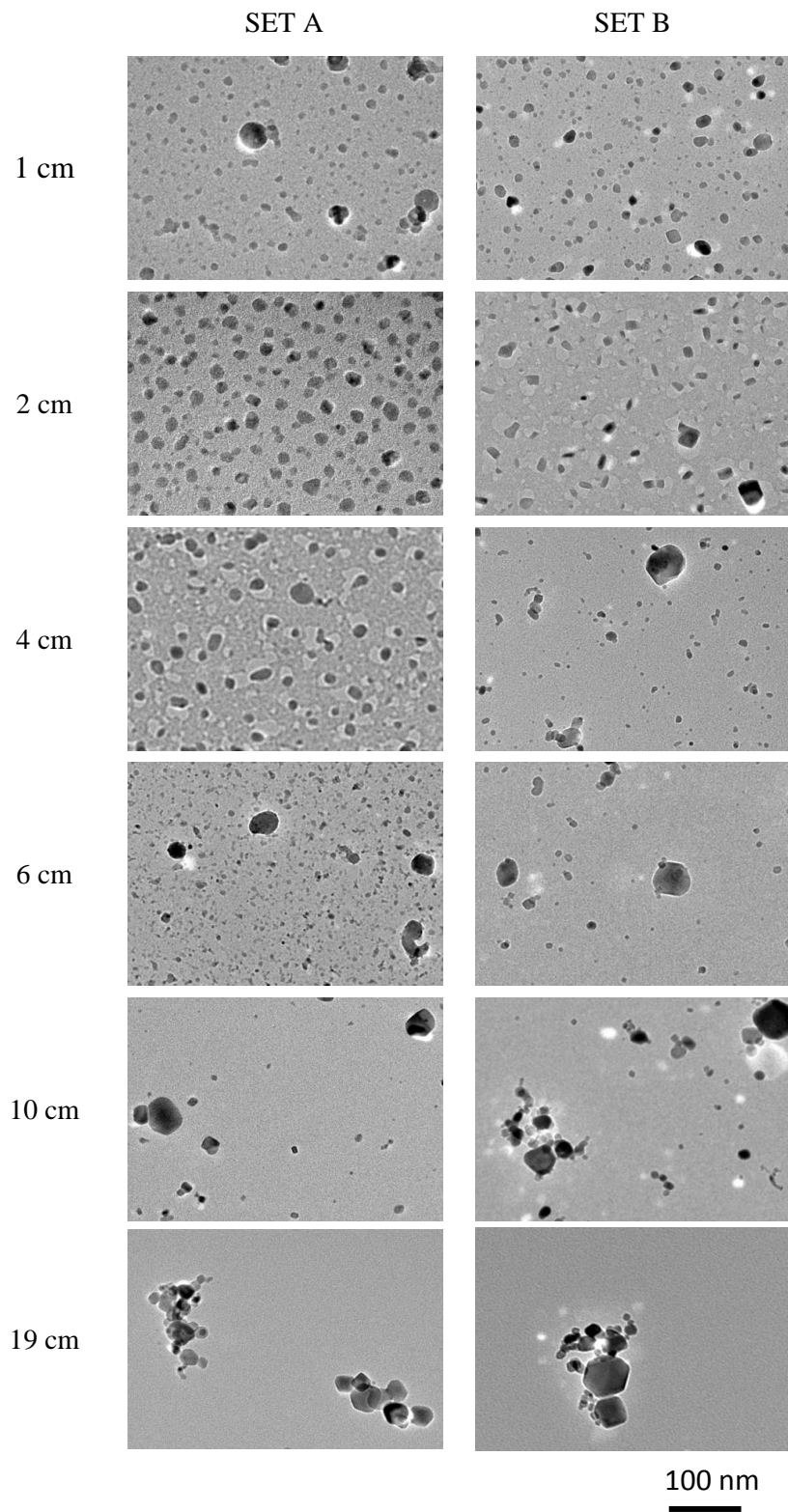
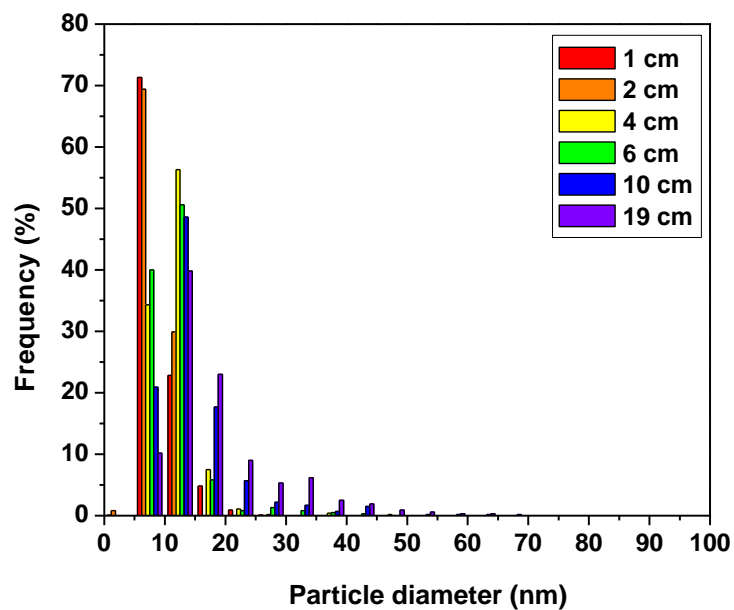
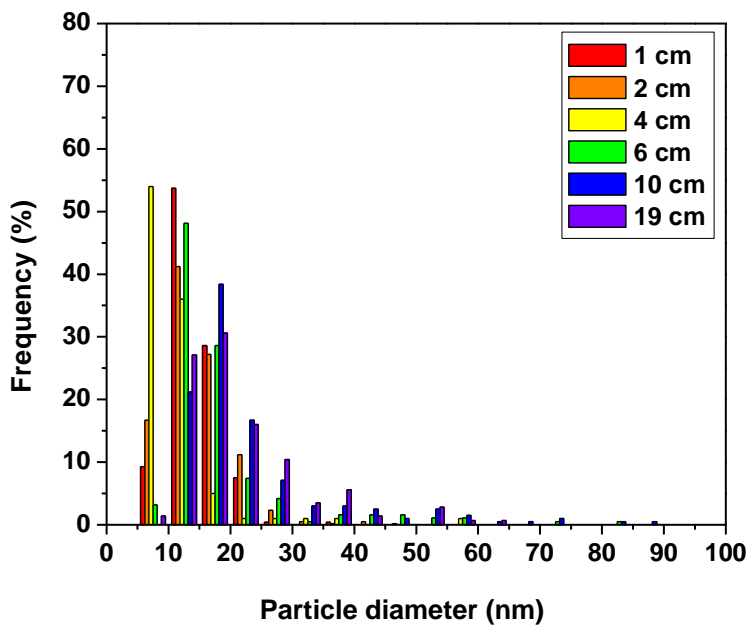


Figure 3.6. TEM micrograph for particles collected at different heights for both flame conditions.





(a)



(b)

Figure 3.7. Histogram for particles collected at different heights for both flame conditions: (a) flame A, and (b) flame B.

### 3.4.2. Modeling of CuO Growth by Solid State Diffusion

The sintering of CuO particles may occur via a viscous flow mechanism if the particles are liquid (Frenkel, 1945) or it might take place by solid state diffusion if the particles are in the solid phase (Kingery et al., 1976). In the two flames in this study, particles would only stay above the melting point of bulk CuO for 25 ms (as shown in Fig. 3.8). This time period is relatively short compared to the time for full coalescence, although the melting temperature for nanoparticles might be less than its bulk phase. As a result, the sintering process was assumed to be by solid state diffusion.

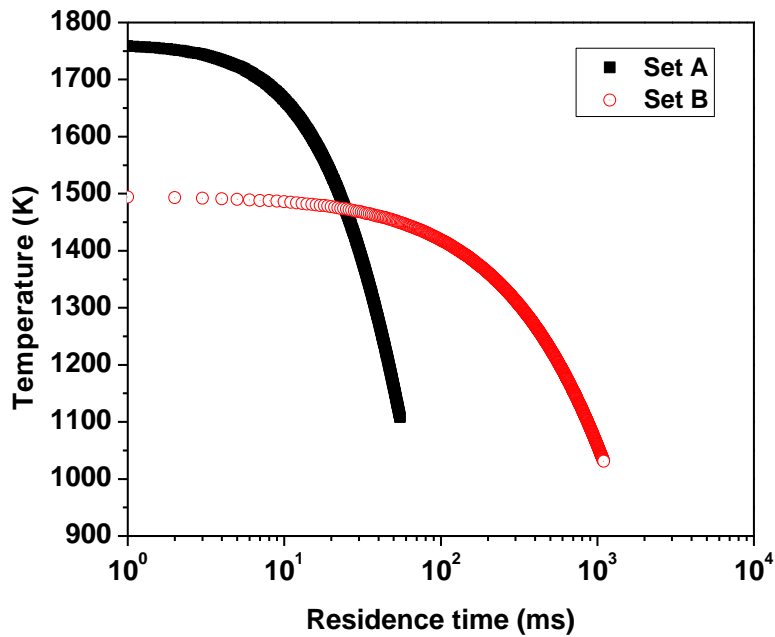


Figure 3.8. Temperature vs. residence time for both flames.

Particle coalescence is driven by the excess surface free energy above the equilibrium state which means the minimizing surface area of fused particles. In the final stages of

coalescence, the change in surface area is given by Koch and Friedlander (1990), and Friedlander and Wu (1994)

$$\frac{dA}{dt} = -\frac{1}{\tau_f}(A - A_s) \quad (3.3)$$

where  $A$  is the surface area of the two particles,  $A_s$  is the resulting minimum surface area after complete coalescence, and  $\tau_f$  is the characteristic coalescence time.

The variables are changed from particle surface area to particle volume in the manner of Lehtinen et al., (1996)

$$\frac{dv_p}{dt} = \frac{3v_p}{\tau_f}(m^{-1} - m^{-4/3}) \quad (3.4)$$

In the equation,  $v_p$  is the volume of the coalescing particles, and  $m$  is the number of particles which coalescing together, taken to be two for simplification.

The characteristic coalescence time was derived by Friedlander and Wu (1994) based on the slowest sintering step

$$\tau_f = \frac{3kTv_p}{64\pi v_0 D \sigma} \quad (3.5)$$

where  $k$  is the Boltzmann constant,  $T$  is temperature of flame,  $v_0$  is the molecular volume for diffusion,  $D$  is the solid state diffusion coefficient and  $\sigma$  is the surface tension.

Also, as the distance from the burner surface increased, a linear function for temperature drop was used to express the gas or particle velocity changed based on distance (Eq. 3.6).

Furthermore  $U_0$  is also a function of distance because of the flame spread resulting from diffusion.

$$\frac{dx}{dt} = \frac{U_0(x)}{T_0} T(x) \quad (3.6)$$

where  $U_0$  is the reference velocity at the reference temperature  $T_0$ .

An expression for particle growth in a precursor-flame jet cooled by concurrent air flow was proposed by Ulrich (1971). Particles in Brownian motion grow as a result of collisions, and coalesce almost instantaneously until the temperature falls to 80% of their melting point (Ulrich, 1971). Thus, the particle size based on collision/sintering theory was obtained by solving Eq. 3.4 with the characteristic coalescence time calculated from Eq. 3.5 and substituting the bulk solid state diffusion coefficient, Eq. 3.7 (Rebane et al., 1997).

$$D = D_0 \exp\left(\frac{-150 \times 10^3}{kT}\right) \quad (3.7)$$

However, because of the lack of surface tension information, several values of surface tension in the range of most metal oxides were used for the comparison. The model results based on different flame conditions are shown in Table 3.5. The simulation was stopped at temperature around 1100 K which is less than the 80% of the melting point of CuO, i.e. 1180K. In the table, taking surface tension equal to 0.5 J/m<sup>2</sup> as an example, in the shorter residence time in the high temperature zone, 66 ms, for set A, resulted in smaller primary particles (6.7 nm). On the other hand, for set B, the residence time was about 550 ms, 8.3 times more than set A, and the particles had more time to coalesce and

led to larger size (9 nm). The experimental particle size at 1180 K was  $11 \pm 4$  nm for both flames. Comparing this data and the modeling result, a fairly good correspondence was reached. However, there is still some difference between the collision/sintering theory and experiment result. This might be due to the limited accuracy of the material properties for nano-sized particles, such as two important temperature dependent variables, solid state diffusivity and surface tension. It has been suggested that diffusion in nanosized particles may differ from bulk diffusion processes (Horvath et al., 1987). In other words, compared to grains, the more loosely packed structure of grain boundaries would result in a higher diffusivity for atoms in grain boundaries. In nanocrystalline materials, the extensive interface regions are loosely packed and thus lead to higher diffusivity (Belova et al., 2003).

Table 3.5. Collision/sintering theory modeling result based on different surface tensions.

Surface tension (J/m <sup>2</sup> )	Primary particle size (nm)	
	Set A	Set B
0.1	3.9	5.3
0.3	5.6	7.6
0.5	6.7	9.0
1.0	8.4	11.4

Furthermore, with the introduction of liquid nitrogen into the system downstream, particles with similar sizes as shown in Table 3.6. The 17% copper nitrate precursor was chosen with flame A. The difference between these three experiments was the distance of the liquid nitrogen introduced point to the collector filter paper which varied the cooling

rate in the post flame zone.

Table 3.6. The effect of liquid nitrogen quenching on particle size and crystallinity.

Liquid nitrogen introduced distance (cm)	Temperature at filter paper (°C)	Size (by FWHM) (nm)	Number mean Particle diameter (nm)	Standard deviation (nm)
None	140	28	18.0	9.3
21.5	80	24	17.8	9.0
13.5	80	17	17.5	8.6

As shown in the table, when the distance between the collector and the liquid nitrogen introduced point was greater, the crystalline size measured by XRD was larger. On the other hand, as the distance between the two points was reduced from 21.5 cm to 13.5 cm, the crystalline size can be reduced from 24 nm to 17 nm which was about 30% smaller. Comparing the result with the data without liquid nitrogen, it was a 15% to 40% difference in the crystalline size. Also the introduction of liquid nitrogen lowered the temperature and diluted the gas stream which decreased the collision as well as the coalescence rate, and the standard deviation of CuO particle diameters was observed to be slightly smaller.

### 3.5. CONCLUSIONS

Copper oxide (CuO) nanoparticles produced via flame spray pyrolysis were nearly spherical with aspect ratios of 1.2-1.3. Several parameters such as flame temperature, residence time, precursor concentration can change the particle size and the size distribution. For example, as the precursor concentration increased from 0.5% to 35%, primary particle size increased from  $7\pm 2$  to  $20\pm 11$  nm in diameter. Primary particle sizes were observed to be larger in set B because the particle residence time in the high temperature region was 8.3 times longer due to the lower gas flow rate. With a further analysis of particle size depending on temperature, particles grew to similar size, i.e.  $\sim 11$  nm, in both flame conditions within the hot temperature region (80% of melting point of CuO) but for set B with longer residence time, the standard deviation of particle size is 45% larger than set A. With liquid nitrogen introduction into the system to quench the particles, as the quenching rate increased, the particle tended to have a smaller crystalline size due to less time available for the atoms to become oriented.

The modeling results of CuO particle growth based on collision/sintering theory with sintering by solid state diffusion were 6.7 and 9.0 nm for set A and set B with the assumption of surface tension of  $0.5 \text{ J/m}^2$ . Comparing the modeling result with the experimental result, which is  $11\pm 4$  nm for both flames, it gave a reasonable simulation. The difference between them might be due to the lack of physical property measurements for nano-scaled materials, which might not be the same as their bulk properties.

## Chapter 4

### Copper Oxide Nanoparticle Made by Flame Spray Pyrolysis for Photoelectrochemical Water Splitting – Photoelectrochemical Study

The results presented in this chapter have been published in the following journal article:

Chiang, C. Y.; Aroh, K.; Franson, N.; Satsang, V. R.; Dass, S.; Ehrman, S. “Copper Oxide Nanoparticle Made by Flame Spray Pyrolysis for Photoelectrochemical Water Splitting – Part II. Photoelectrochemical Study” *Int. J. Hydrogen Energ.*, **2011**, 36, 15519-15526.

#### 4.1. ABSTRACT

A scalable method for hydrogen generation by splitting water via a photoelectrochemical cell was studied. Flame spray pyrolysis and spin coating processing methods were used for preparing copper oxide nanoparticles and copper oxide photocathodes. Copper oxide p-type semiconductor nanoparticles made by flame spray pyrolysis were spin coated on conducting ITO substrates and served as photocathodes for photoelectrochemical splitting of water. The film thickness was controlled by the concentration of the CuO suspension solution and numbers of layer deposited on the substrate. As sintering temperature increased to 600 °C, crystalline diameter increased from 28 nm (before sintering) to 110 nm and the bandgaps decreased from 1.68 eV to 1.44 eV. A 387 nm thickness CuO film with bandgap 1.44 eV was demonstrated to have 1.48% total conversion efficiency and 0.91% photon-to-hydrogen generation efficiency. The net photocurrent density (photocurrent - dark current) was measured to be 1.20 mA/cm<sup>2</sup> at



applied voltage of -0.55 V vs. Ag/AgCl in 1 M KOH electrolyte with 1 sun (AM1.5G) illumination. Based on the Mott-Schottky plot, the carrier density was estimated to be  $1.5 \times 10^{21} \text{ cm}^{-3}$  and the flatband potential to be 0.23 V vs. Ag/AgCl. Furthermore, the valence band edge and conduction band levels were found to lie at -5.00 eV and -3.56 eV respect to the vacuum respectively.

## 4.2. INTRODUCTION

Hydrogen is very attractive as a clean fuel due to its high energy density and benign product, water, upon oxidation (Bak et al., 2002; Yilanci et al., 2009). It can be produced from a variety of feedstocks such as fossil resources, i.e. coal and natural gas, as well as renewable resources, i.e. biomass and even water. The splitting of water by sunlight to produce hydrogen is one of the most altruistic forms of energy production, because both water and sunlight are abundant. Since Edmond Becquerel (1839) discovered the photoelectric effect, both scientists and engineers have been allured by the idea of converting sunlight into electric power or chemical fuels. The dream is to capture the freely available energy from sunlight and turn it into electric power, or use it to generate fuels such as hydrogen (Grätzel, 2001). Producing hydrogen from water splitting using solar energy based on photoelectrochemical (PEC) cells (Heller, 1984; Murphy et al., 2006; Chen et al., 2007; Liu et al., 2008) is highly desirable because it leaves less of a carbon footprint and it allows storage of solar energy as fuel. The first study of PEC water splitting by  $\text{TiO}_2$  was reported by Fujishima and Honda (1972). The details such as the charge transport of mesoscopic semiconductor materials (Hagfeldt and Grätzel,

1995), materials-related process and aspects (Bak et al., 2002), and hydrogen generation at irradiated oxide semiconductor-solution interfaces (Rajeshwar, 2007) have been explored extensively since then.

For economic reasons, it is very important to develop durable photoelectrode materials and their processing technologies with high-efficiency and corrosion-resistance characteristics by integrating and engineering smart systems. Since there is no ideal photoelectrode material commercially available for water splitting, tailored materials have to be engineered. In a PEC cell, light falls on and is absorbed by a semiconductor surface, and electron-hole pairs are generated. The depletion layer formation at the semiconductor electrolyte interface leads to energy band bending in materials. The electrons and holes perform chemical redox reactions at the semiconductor photocathode (for a p-type material) and the platinum anode. Typically, for p-type semiconductors, minority carrier (electrons,  $e^-$ ) migration constitutes the photovoltage and results in the splitting of water at the electrolyte interface, creating  $\text{OH}^-$  and  $\text{H}_2$ . The majority charge carriers (holes,  $h^+$ ) migrate to the transparent conducting oxide coated substrate surface, and electric current flows through the circuit connecting the photocathode to the metal anode. The  $\text{OH}^-$  are transported through the electrolyte and react at the anode surface transferring the ionic charge to the electrode and producing water and oxygen gas (Bockris and Khan, 1993).

Light quanta with energy less than the bandgap of a semiconductor and the fraction of light with higher energy than the bandgap would either be lost in the conversion process or have no contribution to the PEC process, and thus the bandgap of a material plays an important role in terms of the device efficiency. As discussed in Kuczkowski (1991), the

resulting maximum efficiency of about 31% of visible sunlight conversion corresponds to a semiconductor bandgap of 1.1-1.4 eV and so there is an incentive to avoid materials with bandgaps much greater than this minimum required. In this point of view, relatively low cost materials, i.e. copper oxide with direct bandgap around 0.7-1.6 eV (Schultze and Lohrengel, 2000) is the first concern. Furthermore, in order to boost the efficiency, high surface area materials or architectures would be needed. Thus the decrease of CuO particle size to the nanoscale might increase the PEC performance. In recent years, use of nanostructured materials in PEC cells has offered increased efficiencies, resulting from their unique electrical and optical properties. Nanosized semiconductors can be used to obtain large specific surface areas for solar energy absorption and nanoparticles can be explored to modify spatial separation of photogenerated electrons and holes as well as the local electron polarization (Turner, 1999). Furthermore, Nakaoka et al. (2004) proposed that the value of energy gap ( $E_g$ ) is larger for smaller CuO crystals, i.e. bandgap of 1.56 eV for crystalline size of 12 nm and bandgap of 1.38 eV for the crystalline size of 41 nm. The dependence of the energy gap of particles reduced in size to the nanoscale could be attributed to the structural changes, surface reconstruction, lattice contraction atomic relaxation, surface, or strain induced by a host material.

In this part of study, CuO nanoparticles made by a relatively cheap and scalable process (Pratsinis, 1998; Kammler et al., 2001; Jang, 2001), flame spray pyrolysis (FSP) as shown in part I (Chapter 3 and Chiang et al., 2012a), were applied to the PEC cell application. The properties of CuO nanoparticles and the CuO thin film electrodes were analyzed and the PEC performances of the flame made CuO as well as the commercial CuO were also studied and compared.

## **4.3. MATERIALS AND METHODS**

### **4.3.1. CuO Particle Preparation**

For the production of CuO nanoparticles, flame spray pyrolysis (FSP) was chosen because of its capability for producing nanoparticles in an industrial scale at a relatively low cost. Copper nitrate [Cu(NO<sub>3</sub>)<sub>2</sub>·3H<sub>2</sub>O], (Strem Chemicals, Inc. USA) with concentration of 17% w/w was chosen as the precursor and decomposed in a methane flame. The particles were collected on a filter paper (W. L. Gore & Associates Inc., USA) and then taken off by a blade. More detailed information about particle formation and FSP system can be found in Chapter 3 (Chiang et al., 2012a).

### **4.3.2. Electrode Preparation**

Spin coating was chosen for the film preparation process with ethanol used as the solvent to suspend copper oxide particles. An ultrasonicator (Branson B3, USA) was used to disperse particles in solvent at a concentration of 30 mg CuO/mL ethanol to decrease the probability of particle aggregation. The spin coating experiment was conducted by a spinner (Headway PWM32 Spinner, USA) at 2000 rpm for 8 seconds (each layer) in a class 10,000 clean room. Samples with 2-15 layers coated have been tested. Indium-tin-oxide (ITO) coated microscope slides (SPI supplies, USA) with resistivity of 8-12 Ω were chosen as the conductive glass substrate. The ITO substrates were cleaned by isopropanol and dried before use to remove any grease and dust. A benchtop muffle furnace (Thermo Scientific Thermolyne, USA) was used to sinter the film samples after the spin coating process in order to produce more durable films.

### 4.3.3. Characterization

**X-ray Diffraction.** The crystalline size of these CuO particles and CuO film was determined by X-ray diffraction (XRD) results, using the Scherrer equation (Eq. 4.1) (Alexander and Klug, 1950). XRD measurements were performed using a Philips PW 1800 diffractometer with a graphite monochromator and with Cu  $K_{\alpha}$  ( $\lambda=1.54 \text{ \AA}$ ) as the incident radiation.

$$\tau = \frac{K\lambda}{\beta \cos \theta} \quad (4.1)$$

where  $\tau$  is the mean crystallite dimension,  $K$  is the shape factor,  $\lambda$  is the X-ray wavelength, typically  $1.54 \text{ \AA}$ ,  $\beta$  is the line broadening at half the maximum intensity (FWHM) in radius and  $\theta$  is the Bragg angle. The dimensionless shape factor has a typical value of about 0.9, but varies with the actual shape of the crystallite.

**Scanning Electron Microscopy (SEM).** The morphology of the copper oxide film and thickness were studied by using scanning electron microscopy (Hitachi SU-70 SEM, Japan) with the acceleration voltage of 5 kV and the working distance of about 6 mm. The thickness of the film was determined by the cross section of the film samples.

**UV-vis Absorbance.** The transmittance spectra were determined using a UV-vis spectrophotometer (Hitachi, Japan). The absorption coefficient ( $\alpha$ ) of the films was estimated from the spectrum with taking ITO glass substrate placed in the reference beam and calculated by Eq. 4.2.

$$\alpha = \frac{\left[ \ln \left( \frac{1}{T} \right) \right]}{d} \quad (4.2)$$

$\alpha$  is absorption coefficient (1/m),  $d$  is the film thickness (m),  $T$  is transmittance of the film. The bandgap of CuO film can be determined by the plot of  $(\alpha h\nu)^2$  against photon energy ( $h\nu$ ) with  $n=1$  for direct transit shown as Eq. 4.3.

$$\alpha h\nu = A(h\nu - E_g)^{n/2} \quad (4.3)$$

where  $A$  is a constant,  $E_g$  is the optical bandgap,  $h$  is Planck's constant and  $\nu$  is the frequency of light.

**Photoelectrochemical (PEC) Study.** The PEC study was for determination of the photocurrent at both dark and illumination conditions in a three-electrode configuration. 1M KOH (pH 14) was chosen as electrolyte while Ag/AgCl in saturated KCl (Gamry Instruments, USA) and platinum gauze (52 mesh, 99.9%, Sigma-Aldrich, USA) were chosen as reference electrode and counter electrode, respectively. The reactor was made by quartz plates (Chemglass, USA). The CuO electrode was scanned at 50 mV/s between -700 mV and 200 mV versus Ag/AgCl. The CuO electrodes with area of 2.25 cm<sup>2</sup> were illuminated with a 150 W full spectrum solar simulator (Oriel Instruments, USA) using a full reflector beam turning mirror (Oriel Instruments, USA) and a AM1.5G filter with a measured intensity of 1 sun (1000 W/m<sup>2</sup>) by a reference cell (Oriel instrument, USA) at 25°C. The bias voltage and current measurements were made by a potentiostat (eDAQ, Australia) coupled with the hardware system (e-corder, Australia) and a software (EChem, Australia).

**Flatband Potential and Carrier Density.** In order to know the flatband potential and carrier density, the Mott-Schottky plot was needed and could be done by the AC impedance measurement. It was performed in the dark at AC amplitude of 5 mV and a frequency of 1 kHz with a three-electrode system. The equipment used was an Impedance (Solartron, USA) coupled with a potentiostat. The capacity can be calculated by the following equations based on the imaginary part of the impedance ( $Z''$ ),

$$Z = Z' + iZ'' \quad (4.4)$$

$$Z'' = -\frac{i}{\omega C} = -\frac{i}{2\pi f C} \quad (4.5)$$

where  $Z$  is the impedance,  $Z'$  is the real part of impedance,  $C$  is capacitance,  $f$  is AC frequency in Hertz. Based on the Mott-Schottky plot ( $1/C^2$  versus  $V$ ), the flatband potential ( $V_{fb}$ ) can be obtained by the intercept of  $x$  axis and from the slope, the carrier density ( $N_D$ ) can be obtained.

$$\frac{1}{C^2} = \left( \frac{2}{e\epsilon\epsilon_0 A^2 N_D} \right) \left[ (V - V_{fb}) - \frac{k_B T}{e} \right] \quad (4.6)$$

where  $e$  is the electronic charge,  $\epsilon$  is dielectric constant of CuO,  $\epsilon_0$  is the permittivity of vacuum,  $A$  is the area,  $V$  is the applied voltage,  $k_B$  is Boltzmann's constant,  $T$  is the absolute temperature where  $(k_B T/e)$  is a temperature-dependent correction term.

#### 4.4. RESULTS AND DISCUSSION

CuO/ITO films sintered at different temperatures and durations were studied in order to understand the change of particle size and the resistance in the film based on different particle sizes. The thickness of CuO layers was determined by the cross section image taken by SEM and each layer of CuO spin on the substrate was about 97 nm thick. The morphologies of the sintered CuO electrodes were shown in Figure 4.1.

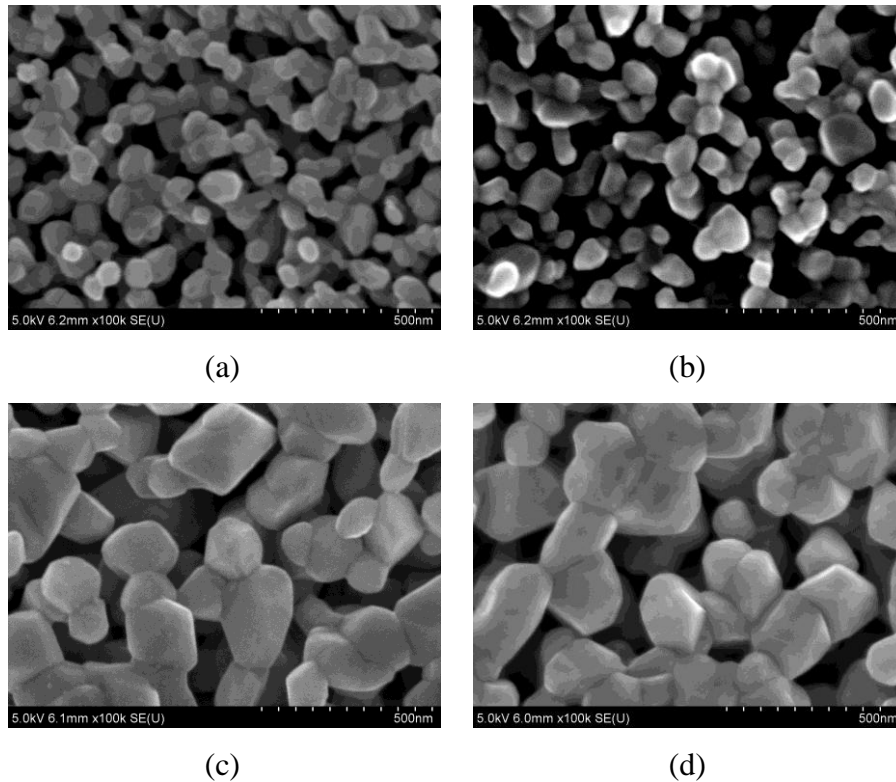


Figure 4.1. Scanning electron micrographs of samples sintering at different temperature and period: (a) 450 °C for 1 hr, (b) 450 °C for 3 hr, (c) 600 °C for 1 hr, (d) 600 °C for 3 hr.

Furthermore, there was not an obvious difference of the morphologies of the CuO electrodes based on SEM before and after one dark and one light scan in the PEC study.



As shown in the SEM micrographs, particle size increases from about 50 nm to 150 nm in diameter with the increase of sintering temperature from 450 °C to 600 °C. Also, the film samples were confirmed to be CuO by X-ray diffraction pattern as shown in Figure 4.2. The crystalline sizes calculated by Scherrer equation and based on different sintering temperatures and durations were tabulated in Table 4.1. Since all the powder used was collected and well mixed before using for the film preparation, the XRD result should be representative. Also, at least three film samples for each condition were prepared for the measurement to check the reproducibility. The given numbers in the table are the average. As sintering temperature and duration increased, the crystalline size increased from 28 nm for the CuO particle prepared by FSP to 66-77 nm and 106-110 nm for CuO thin film sintered at 450 and 600 °C, respectively. This trend is consistent with the result given in SEM micrographs.

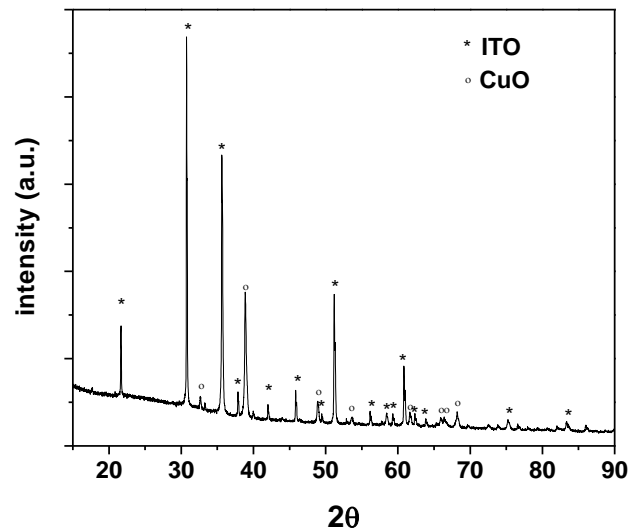


Figure 4.2. X-ray diffraction patterns of CuO films deposited on a ITO glass substrate.

Table 4.1. The optical bandgaps of CuO films prepared from different sintering temperature and duration.

Sinter temperature (°C)	Sintering duration (hr)	Crystalline size* (nm)	Bandgap (eV)	Thickness (nm)	Net		
					photocurrent density (mA/cm <sup>2</sup> )	Efficiency $\eta_c$ (%)	Efficiency $\varepsilon$ (%)
---	---	28.0	1.68	---	---	---	---
450	1	66.6	1.64	580	0.26 / 0.39	0.11 / 0.30	0.32 / 0.48
450	3	70.4	1.58	580	0.32 / 0.50	0.13 / 0.38	0.39 / 0.62
600	1	106.1	1.49	580	0.51 / 0.98	0.21 / 0.72	0.63 / 1.21
600	3	110.6	1.44	580	0.51 / 1.06	0.21 / 0.80	0.63 / 1.30
600	3	110.6	1.44	390	0.51 / 1.20	0.21 / 0.91	0.63 / 1.48

\* Crystalline size was calculated by the Scherrer equation.

Note: for the two numbers in the last three columns, the first number is the bias voltage at -0.2 V vs. Ag/AgCl and the second is at -0.55 V vs. Ag/AgCl.

For determination of the bandgap for each CuO film sample, the plot of  $(\alpha h\nu)^2$  versus photon energy was shown in Figure 4.3. Based on the interception of the axis of photo energy ( $h\nu$ ), the bandgap ( $E_g$ ) of CuO films with thickness of 580 nm sintered at different temperature and time were determined. The linear relationship observed indicated that the transition is performed directly. For the nanoparticle with crystalline size of 28 nm produced from FSP, the optical bandgap was measured to be 1.68 eV. As the sintering temperature increased from 450 °C to 600 °C, the bandgap decreased from around 1.58-1.64 eV to 1.44-1.49 eV based on the sintering duration, 3hr and 1hr respectively, which was also confirmed by the difference in the colors of the films. The change of  $E_g$  can be attributed to the temperature and duration of sintering. As the sintering temperature and duration increase, the particles are expected to grow larger and thus the physical

properties of CuO would approach to the bulk. The change of bandgaps based on particle size was also noticed by Nakaoka et al. (2004) who proposed that the value of energy gap ( $E_g$ ) is larger for smaller CuO crystals, i.e. bandgap of 1.56 eV for crystalline size of 12 nm and bandgap of 1.38 eV for the crystalline size of 41 nm.

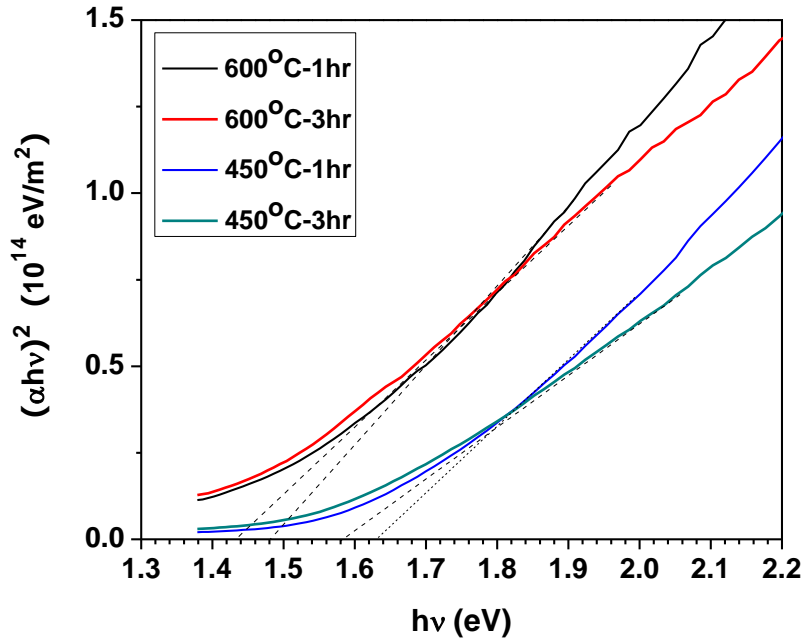


Figure 4.3. The relationship between  $(\alpha hv)^2$  and  $(hv)$  for CuO films with thickness of 580 nm which were sintered at 450 °C and 600 °C and for 1 hr and 3 hr.

The photocurrent density of the CuO-ITO electrode as a function of applied voltage in 1M KOH solution is shown in Figure 4.4. The electrode showed an onset of photocurrent at 0.15 V vs. Ag/AgCl, which rose to 0.5 mA/cm<sup>2</sup> at about -0.2 V vs. Ag/AgCl (0 V vs. NHE,  $E_{\text{redox}}(\text{H}_2\text{O}/\text{H}_2)$ ) and then reached a maximum net photocurrent density (photocurrent – dark current) of 1.06 mA/cm<sup>2</sup> at -0.55 V vs. Ag/AgCl before the onset of

the dark current. The onset of the cathodic photocurrent giving a positive potential shift of about 0.7 V from the dark current rise is the proof of the p-type semiconductor behavior.

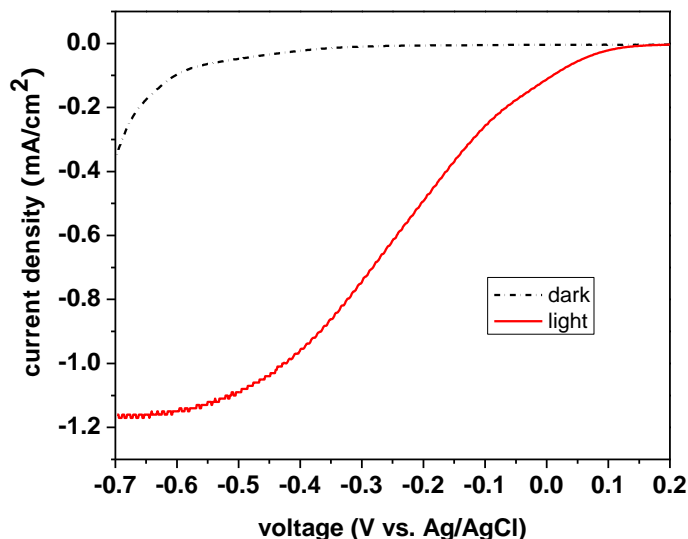
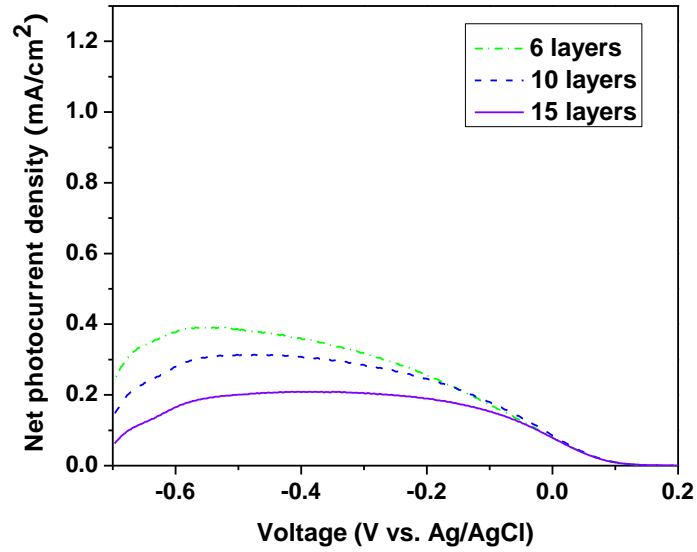


Figure 4.4. Current-potential (I-V) characteristics curve for a CuO/ITO electrode (thickness of CuO layer is 580 nm and sintered at 600 °C for 3 hr) in the dark and under illumination in a 1 M KOH electrolyte.

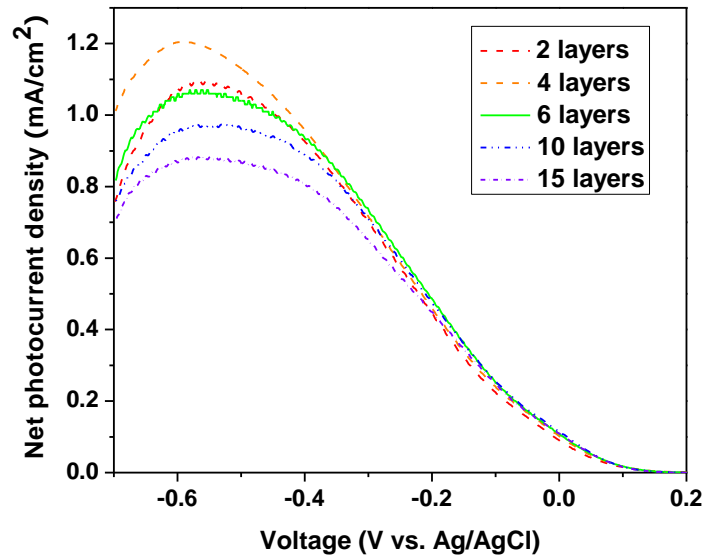
In Figure 4.5, the effects of the thickness of the CuO films on the net photocurrent density were considered. For films sintered at 450 °C shown in Figure 4.5(a), as the film thickness increased from 6 layers to 15 layers, i.e. 580 nm-1450 nm in thickness, the net photocurrent density decreased from 0.4 to 0.16 mA/cm<sup>2</sup>. This might be because as film thickness increased, the resistance of the film increased and the electrons and holes would have a greater tendency to recombine since it is more difficult for the charge carrier to be transported to the external circuit. Similar situation was observed for the films sintered at

600 °C. However, upon lowering the thickness of the film to 4 and 2 layers, i.e. 387 to 193 nm, the photocurrent density first increased then decreased. This might indicate that the optimized thickness is near 387 nm. However, for the photocurrents for 3-5 layers, i.e. 290-483 nm, there was not an apparent difference which implied that in this range, the ratio of the effect on increasing absorption of light to the effect on resistance in the system might be comparable. For a further decrease, the thickness of the film might lead to lack of the CuO to absorb the light efficiently. Furthermore, by comparing the two sintering temperatures and durations, a much higher photocurrent density was obtained with the sample sintering at 600 °C for 3 hr, and this might be due to the larger particle size, i.e. smaller bandgap, which can absorb more light. Furthermore, the electrical conductivities of CuO films sintered at 450 °C and 600 °C were measured to be  $1.2 - 5.4 \times 10^{-6}$  S/cm and  $1.6 - 2.7 \times 10^{-6}$  S/cm, respectively by the electrochemical impedance spectroscopy. There is no significant difference of the film electrical conductivities based on the sintering temperatures, but as the thickness increased, the resistance would increase accordingly because of the linear relationship between resistance and the thickness (length). Comparing this result with the literature (Chauhan et al., 2006), an opposite tendency was observed. In Chauhan et al.'s results, a better photocurrent density was obtained when the sintering temperature was lower (Chauhan et al., 2006). The difference between these two might be easily explained by the CuO particle size and the thickness of the CuO film. Electron-hole pairs have high potential to recombine if the particle size is large or the thickness of the film is large. Usually the diffusion length of the charge carrier is in the magnitude of a nanometer, thus as particle

size and film thickness are in the micron scale, the high electron-hole recombination rate would decrease the photocurrent density.



(a)



(b)

Figure 4.5. Net photocurrent density of different thickness of CuO/ITO electrodes sintered at (a) 450 °C for 1 hr, and (b) 600 °C for 3 hr.

The comparison of the CuO sources for the PEC performance, CuO nanoparticles with reported diameter smaller than 50 nm were purchased from Sigma-Aldrich. With the same method for manufacturing the CuO electrodes and both with thickness of 580 nm, the photocurrent density result was shown in Figure 4.6. The maximum photocurrent densities all located at the applied bias voltage of -0.55 V vs. Ag/AgCl and after the dark current raised (-0.55 V vs. Ag/AgCl), the net photocurrent densities decreased. The relatively flat tendency for the Sigma-Aldrich CuO samples was due to the scale. No matter what the sintering temperature and duration, the CuO electrode composed of CuO from Sigma-Aldrich generated much lower net photocurrent densities, i.e. 0.05 and 0.25 mA/cm<sup>2</sup> at -0.55 V vs. Ag/AgCl for films sintered at 450 °C and 600 °C respectively.

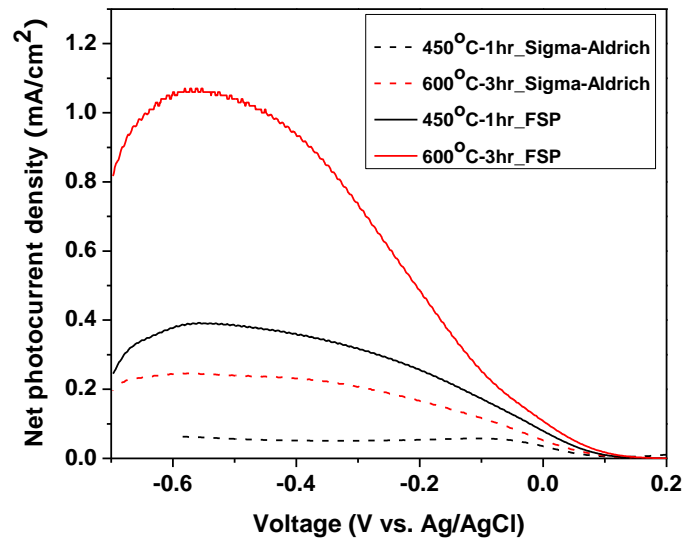


Figure 4.6. Net photocurrent density of CuO/ITO electrodes (CuO thickness is 580 nm) with different CuO sources and sintering temperatures.

Comparing these results to the CuO made by FSP with net photocurrent densities of 0.39 and 1.06 mA/cm<sup>2</sup> at -0.55 V vs. Ag/AgCl for films sintered at 450 °C and 600 °C, the photocurrent of CuO made by FSP was about 4.2-7.8 times higher. The reason might be explained by the particle morphologies as shown in the SEM micrographs (Figure 4.7). The CuO particles purchased from Sigma-Aldrich were not similar in size. The large particles might lead to an increased chance for the electron and hole to recombine and the poor sintering in the small particles also leads to a higher resistance for the electron and hole to transport. In this point of view, the relatively uniform CuO nanoparticles made by the FSP system give a much better performance in the photoelectrochemical study.

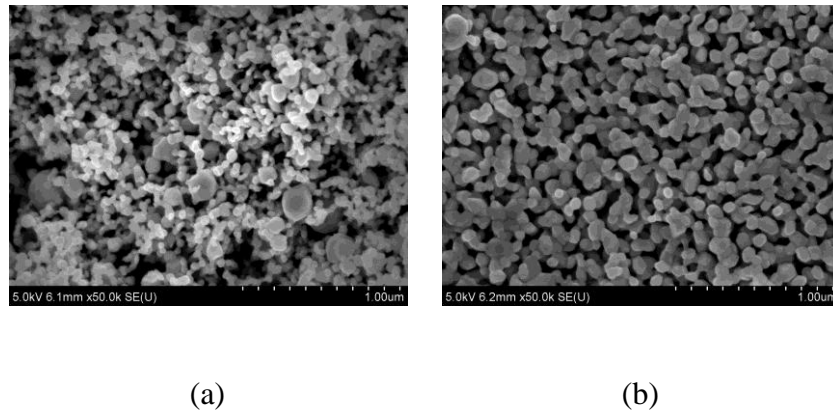


Figure 4.7. Scanning electron micrographs of CuO film sintered at 450 °C from different CuO sources: (a) purchased from Sigma-Aldrich (b) made by our FSP system.

**Conversion Efficiency.** There are two ways to calculate the conversion efficiency of PEC cells: the total conversion efficiency ( $\epsilon_{eff,total}$ ) which includes light and electrical energy of the cell to chemical energy with an external applied potential under illumination condition (Khan and Akikusa, 1999), and the other is the solar conversion



efficiency ( $\eta_c$ ) or efficiency of photon-to-hydrogen generation which is the ratio of the power used on water splitting to the input light power (Bak et al., 2002).

$$\epsilon_{eff,total} = \frac{\text{total power output}}{\text{light power input}} \times 100\% = \frac{j_p E_{rev}^0}{I_0} \times 100\% \quad (4.7)$$

where  $j_p$  is photocurrent density at a certain applied voltage,  $E_{rev}^0$  is the standard water splitting reaction potential (1.23 V vs. NHE) at pH =0.0, and  $I_0$  is the light intensity with unit of W/m<sup>2</sup>.

$$\eta_c = \frac{j_p (E_{rev}^0 - V_{bias})}{I_0} \times 100\% \quad (4.8)$$

where  $V_{bias}$  (V vs. RHE) is the applied external potential.

Also with the conversion of Ag/AgCl reference electrode to the reversible hydrogen electrode (RHE) (Eq. 4.9), the applied external potential and the effect of pH of electrolyte can be converted into the potential versus RHE.

$$E_{RHE} = E_{AgCl} + E_{AgCl}^0 + 0.059pH \quad (4.9)$$

where  $E_{AgCl}^0 = 0.197 V$  at 25°C.

For the four layer CuO film electrode (387 nm in thickness) sintered at 600 °C for 3 hr, at the applied voltage of -0.2 V vs. Ag/AgCl in 1M KOH, the photocurrent was found to be 0.51 mA/cm<sup>2</sup> and  $\epsilon_{eff,total}$  and  $\eta_c$  were calculated to be 0.63% and 0.21%, respectively. On the other hand, at the applied voltage of -0.55 V vs. Ag/AgCl in 1M KOH which gave the maximum photocurrent, i.e. 1.20 mA/cm<sup>2</sup>, the  $\epsilon_{eff,total}$  and  $\eta_c$  were calculated to be

1.48% and 0.91%, respectively. Additional efficiency calculation results are also tabulated in Table 4.1. Comparing the efficiency with the other metal oxide film systems based on AM 1.5 (1000 W/m<sup>2</sup>) illumination source, the undoped  $\alpha$ -Fe<sub>2</sub>O<sub>3</sub> at potential of 1.23 V vs. RHE gave the total conversion efficiency of 0.0123%-0.738% (Duret and Gratzel, 2005; Kay et al., 2006; Saremi-Yarahmadi et al., 2009; Tahir et al., 2009). For CuO system, most of the systems were not done under the AM 1.5 illumination condition and thus no straight forward comparison was available.

Figure 4.8 is the Mott-Schottky plot of (capacitance)<sup>-2</sup> vs. potential for a CuO-ITO electrode in 1M KOH electrolyte. The extrapolation of the straight line to the abscissa and the slope give the flatband potential,  $V_{fb}$ , and the charge carrier density,  $N_D$ , respectively. The value of  $N_D$  was estimated to be  $1.5 \times 10^{21}$  cm<sup>-3</sup> assuming 10.26 as the dielectric constant of CuO (Nakaoka et al., 2004) and 38% as the film porosity which led to an estimated total surface area of  $1.43 \times 10^{-3}$  m<sup>2</sup>. The detail of the film porosity estimation was given in the appendix A.1. Comparing this number with values in the literature, i.e.  $4.0 \times 10^{18}$  cm<sup>-3</sup> for sintering CuO powder by Koffybery and Benko (1982),  $4.0 \times 10^{20}$  cm<sup>-3</sup> for electrodeposited CuO film by Nakaoka et al. (2004),  $2 \sim 43 \times 10^{18}$  cm<sup>-3</sup> for sol-gel method prepared CuO film by Chauhan et al. (2006), it is found that the carrier density is higher than others, and thus leads to a higher photocurrent density. The flatband potential was found to be 0.23 V vs. Ag/AgCl at pH 14 that included the ( $k_B T/e$ ) term. In the literature, the flatband potentials are known as 0 V (Schultze and Lohregel, 2000), and 0.3 V (vs. SCE) p-CuO (Hardee and Bard, 1977).

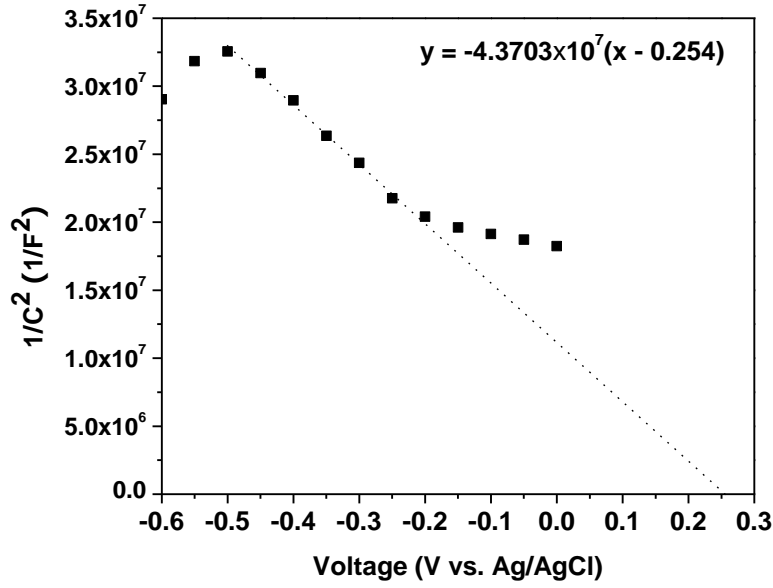


Figure 4.8. Mott-Schottky plots for a CuO/ITO electrode in 1 M KOH electrolyte.

From the experimental results, the position of the band edges for CuO with respect to the vacuum level can be calculated by first knowing the position of the valence band edge with respect to the vacuum level which is denoted here by  $D$ ,

$$D = V_{fb} + 4.64 + \Delta E_F + V_H \quad (4.10)$$

where 4.64 represents the absolute potential of Ag/AgCl below the vacuum level,  $\Delta E_F = E_F - E_V$  which is the difference between Fermi level and the valence band edge, and  $V_H = 0.059(P_0 - pH)$  is Helmholtz potential between CuO electrode and electrolyte. Since the flatband potential was determined at the experimental value of  $P_0$  so  $V_H$  can be neglected (Koffyberg and Benko, 1982). Followed by Eq. 4.10 with  $V_{fb} = 0.23 V$  (vs. Ag/AgCl) at pH 14,  $\Delta E_F = 0.13 eV$  (Koffyberg and Benko, 1982),  $D$  can be obtained

with the value of 5.00 eV (below vacuum level). Since the bandgap of the CuO electrode used is 1.44 eV, the conduction level should lie at 3.56 eV (below vacuum level). This is also the value of the electron affinity. The energy band scheme for CuO in this study as well as CuO in the literature (Nakaoka et al., 2004, Koffyberg and Benko, 1982) was illustrated in Figure 4.9 with all values adjusted to pH 14 electrolyte. All these three studies show the p-type characteristic for the CuO electrodes and the valence and conduction bands located at -4.80 to -5.15 eV and -3.24 to -3.80 eV respected to vacuum, respectively.

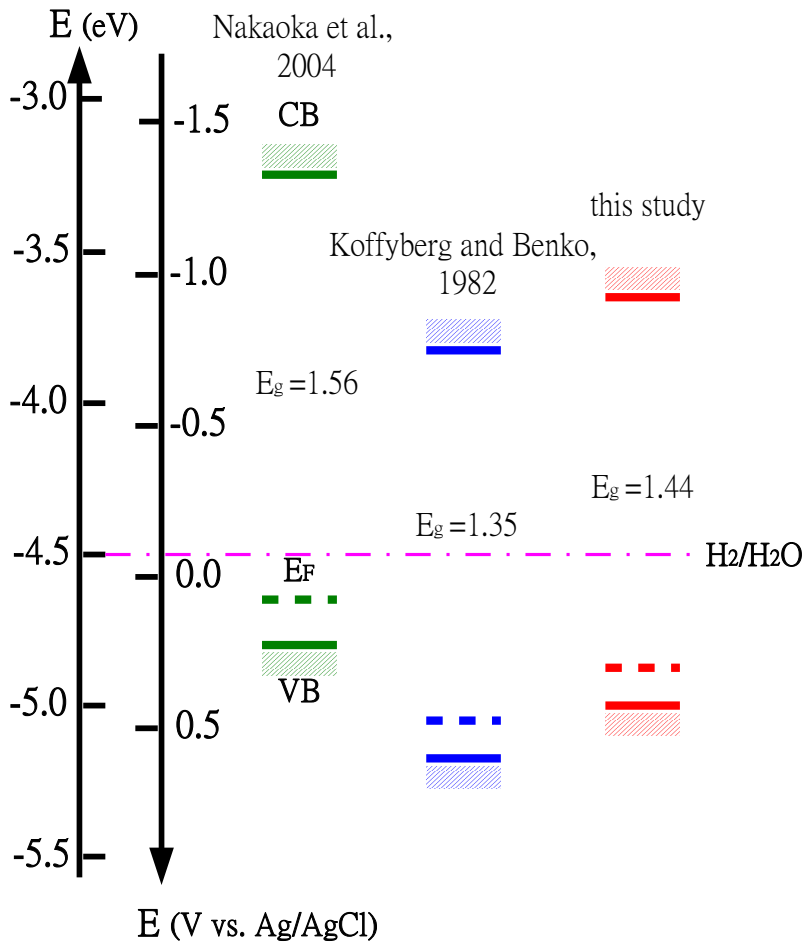


Figure 4.9. Estimated position of CuO bandedges for this study, performed at pH 14, and prior reports in the literature adjusted to pH 14.

## 4.5. CONCLUSIONS

An easy to scale up and relatively low cost photoelectrochemical cell was successfully demonstrated by flame spray pyrolysis made CuO nanoparticles spin coated for 387 nm on a ITO substrate sintered at 600 °C for 3 hr. The high net photocurrent density, i.e. 1.20 mA/cm<sup>2</sup> at applied voltage of -0.55 V vs. Ag/AgCl in 1 M KOH electrolyte, was obtained and which corresponds to the total conversion efficiency ( $\epsilon_{eff,total}$ ) and photon-to-hydrogen generation efficiency ( $\eta_c$ ) as 1.48% and 0.91%, respectively. The bandgap of the CuO thin film was found to be 1.44-1.64 eV based on their sintering temperature and duration. Based on the Mott-Schottky plot, the carrier density was estimated to be  $1.5 \times 10^{21}$  cm<sup>-3</sup> and the flatband potential to be 0.23 V vs. Ag/AgCl. Furthermore, the valence band edge and conduction band level of our CuO thin films lie at -5.00 eV and -3.56 eV respect to the vacuum.

## Chapter 5

### Li Doped CuO Film Electrodes for Photoelectrochemical Cells

The results presented in this chapter have been published in the following journal article:

Chiang, C. Y.; Shin, Y.; Ehrman, S. “Li Doped CuO Film Electrodes for Photoelectrochemical Cells” *J. Electrochem. Soc.*, **2012**, 159, B227-B231.

#### 5.1. ABSTRACT

Li is known for its ability to increase the conductivity of CuO films. Li doped CuO nanoparticles prepared by flame spray pyrolysis and followed by spin coating for the film preparation were studied at dopant concentrations of 0.5 at%, 2 at%, 3.5 at% and 5 at%. The photocurrent density and photon-to-hydrogen conversion efficiency increased by a factor of five to ten when introducing Li into CuO. This is attributable to the increase in the electrical conductivity of the film by almost two orders of magnitude, i.e. from  $2 \times 10^{-6} \sim 4 \times 10^{-6}$  S/cm to  $7 \times 10^{-5} \sim 3 \times 10^{-4}$  S/cm, and thus the increase in the lifetime of the photogenerated charge carriers. The best photocurrent density and photon-to-hydrogen conversion efficiency was  $1.69 \text{ mA/cm}^2$  and 1.3%, respectively, corresponding to the film prepared by 2.0 at% Li-CuO sintered at  $450 \text{ }^\circ\text{C}$  for 1 hr with the thickness  $1.7 \text{ }\mu\text{m}$  at bias voltage of  $-0.55 \text{ V vs. Ag/AgCl}$  in 1M KOH and under 1 sun illumination. Furthermore, the charge carrier density was estimated based on the Mott-Schottky plot to be  $4.2 \times 10^{21} \text{ cm}^{-3}$  which is almost double the charge carrier densities obtained by other doping conditions. The high carrier charge density was also confirmed by the higher photocurrent density.

## 5.2. INTRODUCTION

Hydrogen is an attractive alternative energy because of its high energy density while producing water, a harmless byproduct, upon oxidation (Bak et al., 2002; Yilanci et al., 2009). It can be obtained from fossil fuels, such as coal and natural gas, or renewable resources, such as biomass and water. Among these hydrogen generation methods, water splitting is of interest one by considering the relative abundance of water. Researchers have proved that it is possible to simply use sunlight to split water and generate renewable hydrogen energy by a photoelectrochemical (PEC) cell (Heller, 1984; Murphy et al., 2006; Chen et al., 2007; Liu et al., 2008; Grätzel, 2001). Furthermore, by a PEC cell, the solar energy can be transformed into a fuel and stored for later usage. Compared to obtaining hydrogen from fossil fuels, solar water splitting has the potential to be carbon free. However, the critical technical issue is the efficient absorption of solar energy. Only photons with higher energy than the bandgap of a material can be absorbed and used. In other words, materials with smaller bandgap are preferred. Thus, the narrow bandgap material, copper oxide, is very attractive. Additional advantages of copper include its relatively low toxicity and high earth abundance.

Several methods have been used to prepare copper oxide thin films, such as sol-gel (Chauhan et al., 2006), spray pyrolysis (Morales et al., 2004), electrodeposition (Nakaoka et al., 2004), reactive sputtering (Drobny and Pulfrey, 1979; Samarasekara, 2006; Petrantoni et al., 2010), chemical vapor deposition (Arana-Chavez et al., 2010), and flame spray pyrolysis and wet chemical powder preparation coupled with spin coating (Chapter 4 and Chiang et al., 2011; Chapter 6 and Chiang et al., 2012b). Among them, we

have demonstrated that the CuO thin films prepared from making CuO nanoparticles from flame spray pyrolysis (Chapter 3 and Chiang et al., 2012a) followed by spin coating for film preparation give a high photocurrent and a 0.91% photon-to-hydrogen generation efficiency. Typically, for CuO, an intrinsic p-type semiconductor, minority carrier (electrons,  $e^-$ ) migration constitutes the photovoltage and results in the splitting of water at the electrolyte interface, creating  $\text{OH}^-$  and  $\text{H}_2$ . The majority charge carriers (holes,  $h^+$ ) migrate to the transparent conducting oxide coated substrate surface, and electric current flows through the circuit connecting the photocathode to the metal anode. The  $\text{OH}^-$  is transported through the electrolyte and reacts at the anode surface transferring the ionic charge to the electrode and producing water and oxygen gas (Bockris and Khan, 1993).

However, one of the drawbacks of pure CuO serving as a photoelectrode is the relatively low conductivity. The efficiency of a PEC cell may be enhanced by increasing the conductivity of the film, i.e. decreasing the resistance to charge carrier transport. By increasing the conductivity of the film, the recombination rate of excited electrons and holes might be reduced. Doping desired elements into CuO particles to increase conductivity can be easily done by adding the dopant into the precursor. In the literature,  $\text{Li}^+$  ion, which has similar radius to  $\text{Cu}^{2+}$  ion, has been found to increase the conductivity of CuO films about two orders of magnitude (Suda et al., 1992; Ohya et al., 2000; Saito et al., 2003). However, there is no systematic study of the effects of Li doping on PEC behavior. Thus, parameters such as Li dopant concentration, film thickness, and sintering temperatures are studied.



## **5.3. EXPERIMENTAL**

### **5.3.1. CuO Particle Preparation**

To produce copper oxide particles, flame spray pyrolysis (FSP) was used because of its highly efficiency at a relatively low cost. A detailed description of these FSP processes can be found in our previous study (Chapter 3 and Chiang et al., 2012a). Lithium acetate (Sigma-Aldrich, USA) at concentrations of 0.5 at%, 2 at%, 3.5 at% and 5 at% was added into the 1M copper nitrate [ $\text{Cu}(\text{NO}_3)_2 \cdot 3\text{H}_2\text{O}$ ] (Strem Chemicals, Inc. USA) solution as the precursor for the experiment. This precursor was decomposed in a methane flame, and the resulting CuO nanoparticles were collected on filter paper (W. L. Gore & Associates Inc., USA) coupled with a vacuum pump. Using a blade, the particles were scraped off the filter paper and collected in a vial.

### **5.3.2. Electrode Preparation**

Films were produced using the spin coating method. Ethanol was used to suspend the CuO particles. To limit the chances of particle aggregation, an ultrasonicator (Branson B3, USA) was used to keep the particles dispersed in ethanol. Conducting indium-tin-oxide (ITO) coated microscope slides (SPI supplies, USA) with resistivity of 8-12 ohms were used as the substrate. Before usage, the ITO glass substrates were cleaned by isopropanol and dried to remove any foreign, unwanted substances. The film deposition was done by using a spinner (Headway PWM32 Spinner, USA). Each layer of the film was spun on the substrate at 2000 rpm for 8 sec. The film samples were sintered in a benchtop muffle furnace (Thermo Scientific Thermolyne, USA) after the spin coating procedure, to produce more durable films.

### 5.3.3. Characterization

**X-Ray Diffraction.** Specific crystalline sizes of CuO particles and films were determined by X-ray diffraction (XRD) along with the Scherrer equation. A Philips PW 1800 diffractometer with a graphite monochromator with an incident radiation of Cu  $K\alpha$  ( $\lambda=1.54 \text{ \AA}$ ) was used in the XRD analysis.

**X-ray Photoelectron Spectroscopy.** The composition of the Li doped CuO samples were determined using a Kratos Axis 165 X-ray photoelectron spectrometer operating in hybrid mode using Al  $K\alpha$  monochromatic X-rays (1486.6 eV). The survey spectra were done under a pass energy of 160 eV while the high resolution spectra were done under a pass energy of 20 eV. Charge neutralization was required to minimize surface charge.

**Scanning Electron Microscopy (SEM).** The morphology and thickness of the films was studied by using scanning electron microscopy (SEM). The acceleration voltage was set at 3 kV and the working distance at roughly 6 mm. The thickness was measured by analyzing cross-sections of the samples.

**UV-vis Absorbance.** UV-vis spectrophotometer (Hitachi, Japan) was used to measure the transmittance spectra. By placing the ITO glass substrate in the reference beam, we could estimate the absorption coefficient ( $\alpha$ ) of the film. The transmittance ( $T$ ) was calculated using equation:

$$\alpha = \frac{\left[ \ln \left( \frac{1}{T} \right) \right]}{d} \quad (5.1)$$

where  $d$  is the film thickness (m). The bandgap of CuO film can be determined by the plot of  $(\alpha hv)^2$  against photon energy ( $hv$ ) with  $n=1$  for direct transit shown as Eq. 5.2.

$$\alpha hv = A(hv - E_g)^{n/2} \quad (5.2)$$

where  $A$  is a constant,  $E_g$  is the optical bandgap,  $h$  is Planck's constant and  $\nu$  is the frequency of light. The linear relationship was determined over the range of  $hv$  from 1.7 to 1.9 eV. Based on the interception of the axis of photo energy ( $hv$ ), the bandgaps ( $E_g$ ) of CuO were determined.

**Photoelectrochemical (PEC) Characterization.** The PEC study was for determination of the photocurrent at both dark and illumination conditions in a three-electrode configuration. 1M KOH (pH 14) was chosen as electrolyte while Ag/AgCl in saturated KCl (Gamry Instruments, USA) and platinum gauze (52 mesh, 99.9%, Sigma-Aldrich, USA) were chosen as reference electrode and counter electrode, respectively. The reactor was made by quartz plates (Chemglass, USA). The CuO electrode was scanned at 50 mV/s between -700 mV and 200 mV versus Ag/AgCl. The CuO electrodes with area of  $2.25 \text{ cm}^2$  were illuminated with a 150 W full spectrum solar simulator (Oriel Instruments, USA) using a full reflector bean turning mirror (Oriel Instruments, USA) and a AM1.5G filter with a measured intensity of 1 sun ( $1000 \text{ W/m}^2$ ) by a reference cell (Oriel instrument, USA) at  $25 \text{ }^\circ\text{C}$ . The bias voltage and current measurements were made by a potentiostat (eDAQ, Australia) coupled with the hardware system (e-corder, Australia) and software (EChem, Australia).

**Flatband Potential and Carrier Density.** By doing the impedance measurement (Solartron, USA), Mott-Schottky measurements were done in a dark setting at AC

amplitude of 5 mV and a frequency of 1 kHz with a three-electrode system. The plot gives reliable information on the flatband potential and carrier density. The capacity ( $C$ ) can then be calculated using the following equations by taking into account the imaginary part of the impedance ( $Z''$ ) as shown in Eq. 5.4,

$$Z = Z' + iZ'' \quad (5.3)$$

$$Z'' = -\frac{i}{\omega C} = -\frac{i}{2\pi f C} \quad (5.4)$$

where  $Z$  is the impedance,  $Z'$  is the real part of the impedance,  $C$  is the capacitance and  $f$  is the AC frequency in Hertz. The flatband potential ( $V_{fb}$ ) can be obtained from the x-intercept whereas the carrier density ( $N_D$ ) can be calculated from the slope of the Mott-Schottky plot based on Eq. 5.5.

$$\frac{1}{C^2} = \left( \frac{2}{e\epsilon\epsilon_0 A^2 N_D} \right) \left[ (V - V_{fb}) - \frac{k_B T}{e} \right] \quad (5.5)$$

where  $e$  is the electronic charge,  $\epsilon$  is dielectric constant of CuO,  $\epsilon_0$  is the permittivity of vacuum,  $A$  is the surface area,  $V$  is the applied voltage,  $k_B$  is Boltzmann's constant,  $T$  is the absolute temperature where  $(k_B T/e)$  is a temperature-dependent correction term.

**Electrical Conductivity.** Gold was sputtered at two ends of the CuO film which was coated on quartz substrate as electrode. The distance between two ends was 1.5 cm. The electrical conductivity of the films was determined by electrochemical impedance spectroscopy (EIS) carried out on a potentiostat/galvanostat (Solartron, USA).

## 5.4. RESULTS AND DISCUSSION

The FSP produced particles were confirmed to be single phase CuO, as shown in Fig. 5.1. The Rietveld analysis was done to determine the lattice parameters. For CuO, the standard lattice parameter  $a$  is 4.6837 Å. Shown in Table 5.1, as the Li dopant concentration increased, the lattice parameter  $a$  increased to 4.6903 Å when the dopant concentration reached to 5 at%. The increase in the lattice size could be explained by the difference ionic radii of  $\text{Cu}^{2+}$  and  $\text{Li}^+$  where  $\text{Cu}^{2+}$  has crystal ionic radius of 87 pm and  $\text{Li}^+$  has crystal ionic radius of 90 pm. The increase of Li doping concentration leading to a higher Li concentration in CuO was further confirmed by the increase of Li peak intensity in XPS analysis. However, the detected dopant concentration (3.6 at%, 8.8 at%, and 10.5 at%) is higher than the Li concentration in the precursor (2 at%, 3.5 at%, and 5 at%). The increased concentration of lithium at the surface compared to the bulk is likely due to surface segregation of the lithium.

Table 5.1. The effect of Li doping concentration on the lattice parameter  $a$ .

Li doping concentration	Lattice parameter $a$ (Å)
CuO Standard	4.6837(5)
0.5 at%	4.6898(13)
2.0 at%	4.6898(18)
3.5 at%	4.6898(15)
5.0 at%	4.6903(12)

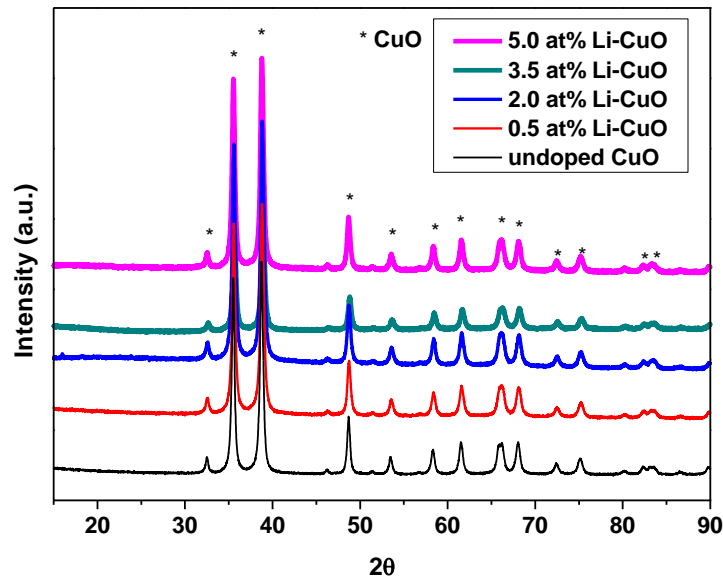


Figure 5.1. XRD for flame spray pyrolysis made Li doped CuO particles.

Figure 5.2 shows the sintering temperature effects on the photocurrent density. There is no photocurrent for the non-sintered samples (not shown in the figure) and it might be explained by the lack of charge carrier transport path between particles. As the sintering temperature increased to 300 °C and 450 °C, connections between the particles improved as necks between particles were formed and this led to improved efficiency for charge carrier transport and an increase in the photocurrent. However, when the sintering temperature further increased to 600 °C for 3 hr, much bigger particles are formed because of a much faster diffusion rate for CuO at 600 °C. As in the literature (Jeong and Choi, 1996), the generated electron and hole pairs are more likely to recombine in the CuO particles instead of at the edge of the particles. This is also implied in the literature (Chapter 4 and Chiang et al., 2011) when the nanosized CuO particles have better

efficiency compared to those CuO particles purchased from Sigma-Aldrich with wide size range, i.e. from tens of nanometer to hundreds of nanometers in diameter.

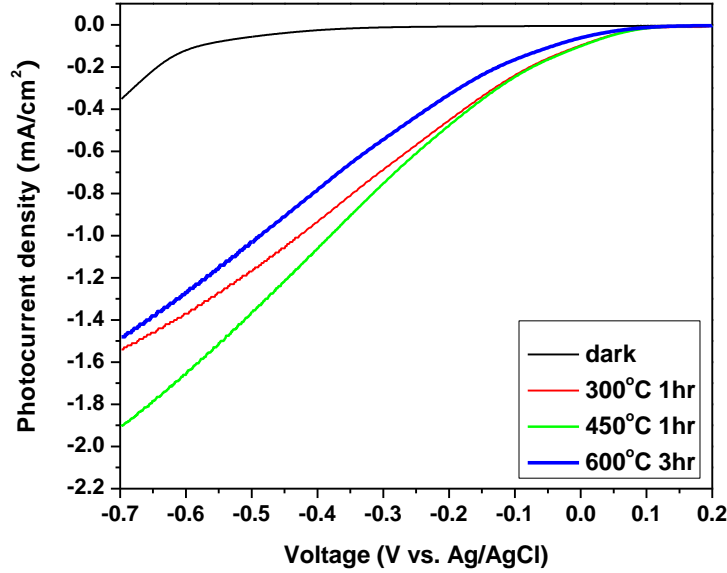


Figure 5.2. Sintering temperature effect on 2 at% Li doped CuO with thickness of 850 nm.

The plot of  $(\alpha h\nu)^2$  versus photon energy was shown in Figure 5.3 for the determination of the bandgap for each CuO film samples. Based on the interception of the axis of photo energy ( $h\nu$ ), the bandgaps ( $E_g$ ) of CuO sintered at temperature either 450°C for 1hr or 600°C for 3 hr were determined. The linear relationship observed indicated that the transition is performed directly. For the nanoparticles with an average crystalline size of 27 nm produced from FSP, the optical bandgap was measured to be  $1.65 \pm 0.02$  eV. As the sintering temperature increased from 450 °C to 600 °C, the bandgap decreased from

around  $1.64 \pm 0.02$  eV to  $1.44 \pm 0.02$  eV which was also confirmed by the difference in the colors of the films.

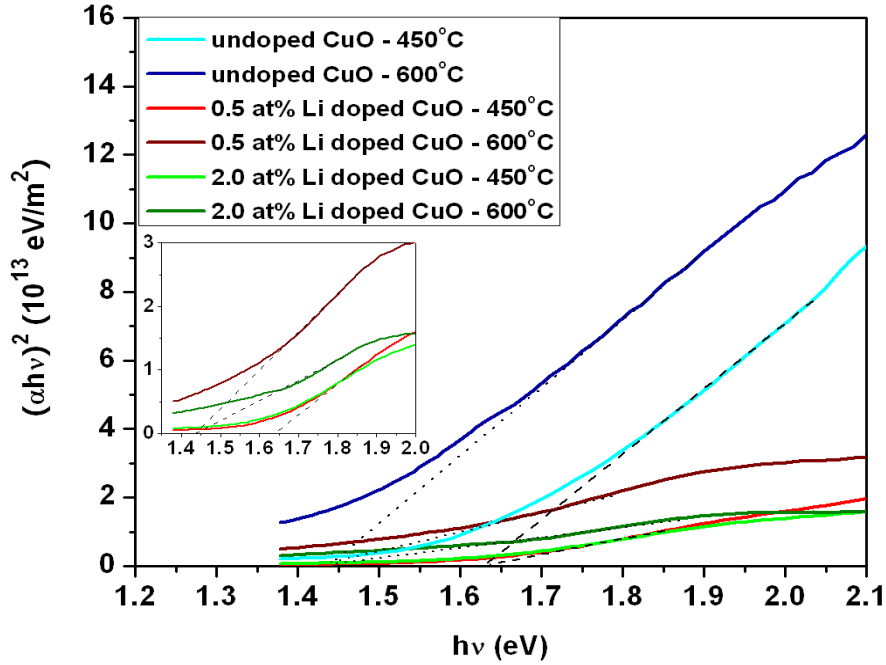


Figure 5.3. The relationship between  $(\alpha h\nu)^2$  and  $(h\nu)$  for Li doped CuO powders sintered at different temperatures.

The change of  $E_g$  can be attributed to the size and morphology changing during the sintering process (Fig. 5.4). The crystalline size of 2 at% Li doped CuO was determined to be 82 nm and 117 nm for sintering temperature at 450 °C for 1 hr and 600 °C for 3 hr, respectively. As the sintering temperature and duration increase, the particles are expected to grow larger and thus the physical properties of CuO would approach to the bulk. The change of bandgaps based on particle size was also noticed in our previous study of undoped CuO (Chapter 4 and Chiang et al., 2011) and by Nakaoka et al. (2004)



who proposed that the value of energy gap ( $E_g$ ) is larger for smaller CuO crystals, i.e. bandgap of 1.56 eV for crystalline size of 12 nm and bandgap of 1.38 eV for the crystalline size of 41 nm. Doping of Li into CuO did not change the light absorbance and thus there was no significant change in the bandgap.

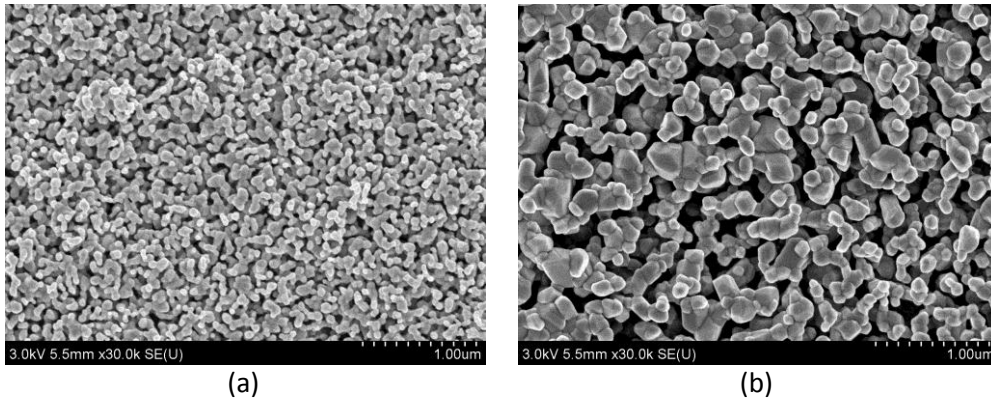
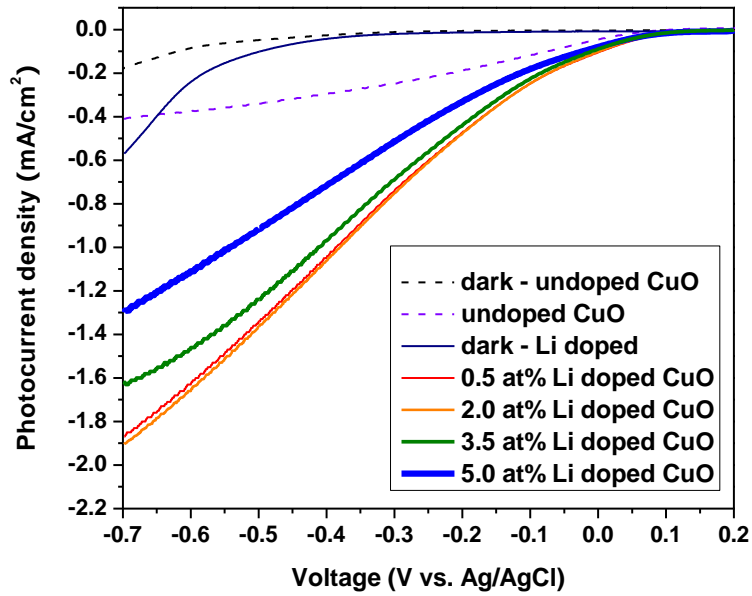


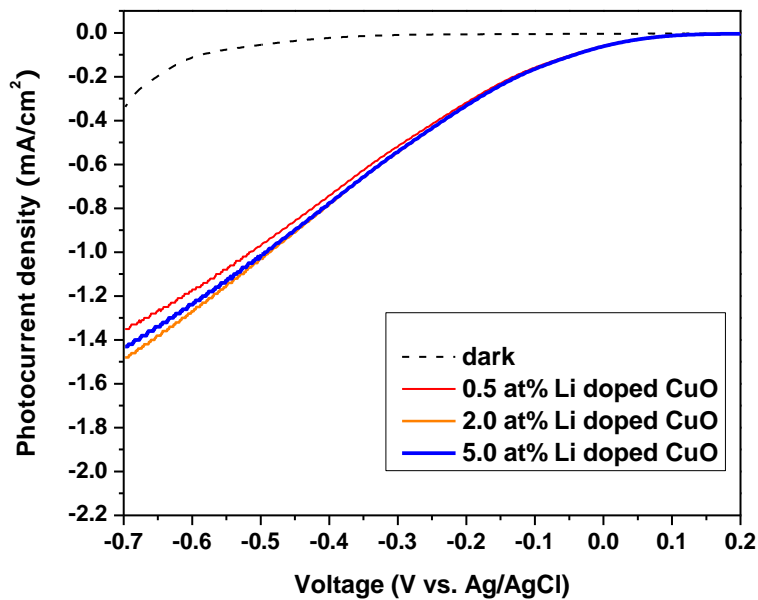
Figure 5.4. SEM image of 2 at% Li doped CuO sintered at (a) 450 °C for 1hr and (b) 600 °C for 3hr.

The photocurrent density of the Li doped CuO-ITO electrode as a function of applied voltage in 1M KOH solution is shown in Figure 5.5. The electrode showed an onset of photocurrent at 0.1 V vs. Ag/AgCl. The onset of the cathodic photocurrent giving a positive potential shift of about 0.65 V from the dark current rise, i.e. -0.55 V vs. Ag/AgCl, is the proof of the p-type semiconductor behavior. Furthermore, in Figure 5.5(a), the photocurrent densities of different dopant concentration samples with thickness of 850 nm and sintered at 450 °C for 1 hr were shown. All the samples with Li dopant added have better photocurrent density compared to the undoped one, i.e. 0.35 mA/cm<sup>2</sup> at applied voltage -0.55 V vs. Ag/AgCl. The photocurrent density increased

dramatically (about 4.3 times) when there was a 0.5 at% Li dopant added and it further increased to 4.9 times, i.e.  $1.69 \text{ mA/cm}^2$ , when 2 at% Li was doped into CuO particles. However, when the dopant concentration was further increased, the photocurrent density decreased and it might be due to a dramatical increase of the aliovalent defects in terms both of charge and spin in the CuO crystal structure leading to a local lattice distortion (Saito et al., 2003). Those defects can serve as recombination centers for the photon generated electron and hole pairs and thus decrease the photocurrent density. However, for samples sintered at  $600 \text{ }^\circ\text{C}$  for 3 hr, the photocurrent densities were not as high as that for samples sintered at  $450 \text{ }^\circ\text{C}$  for 1 hr. This might be explained by the fact that as temperature increases, the atoms have higher energy to arrange themselves. Thus, based on the thermodynamic preference, the material would try to lower its potential by repelling the extrinsic atom. The samples after sintering were examined by XPS and no significant lithium signal was found. This might be due to the lithium becoming volatile upon annealing (Myrach et al., 2010) and copper segregating to the surface (Fatih and Marsan), leading to a lower lithium concentration at the surface, i.e. 6-8 nm, and below the sensitivity limits of XPS. Much higher Li doping is expected to have a high extent of dopant segregation leading non uniform distribution of lithium within the particles, and a dramatic increase in the concentration of aliovalent defects, leading to local lattice distortion. These defects could serve as the electron and hole recombination centers, decreasing the charge carrier density and thus decreasing the photocurrent as shown in Figure 5.5(b).



(a)



(b)

Figure 5.5. Dopant concentration effects on CuO film: (a) film with thickness of 850 nm and sintered at 450 °C for 1 hr, (b). film with thickness of 850 nm and sintered at 600 °C for 3 hr.

Figure 5.6 shows the thickness effects on the 2 at% Li doped CuO film electrodes. As the thickness increased from 430 nm to 1.7  $\mu\text{m}$ , the photocurrent density increases but the degree of the increase in photocurrent density due to the increase of film thickness was leveled when the film became thicker.

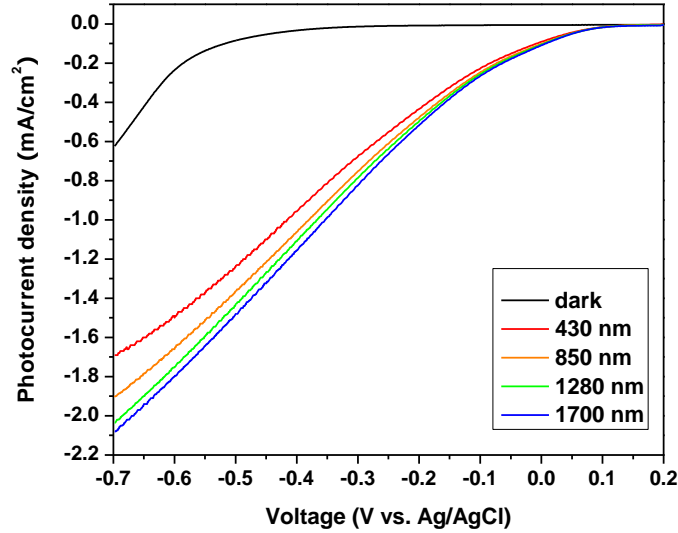


Figure 5.6. The effects of different thickness for the 2 at% Li doped CuO sintered at 450  $^{\circ}\text{C}$  for 1 hr.

In our previous study (Chapter 4 and Chiang et al., 2011), at the sintering temperature of 450  $^{\circ}\text{C}$ , the FSP made CuO nanoparticles with thickness of 580 nm have a photocurrent density of 0.40  $\text{mA}/\text{cm}^2$ . As the thickness further increase to 1.45  $\mu\text{m}$ , a decrease in photocurrent density, i.e. 0.16  $\text{mA}/\text{cm}^2$ , was found which might be attributed to the higher resistance of the film and lead to higher chances of charge carrier recombination. However, as the 2 at% Li was added, the conductivity increased from about  $2 \times 10^{-6} \sim 4 \times 10^{-6}$  S/cm to  $7 \times 10^{-5} \sim 3 \times 10^{-4}$  S/cm based on the electrochemical impedance spectroscopy (EIS), and it helps greatly in the transport of the charge carriers. A similar result was

found in the literature (Saito et al., 2003). This then boosted the amount of free charge carriers and more important, a much thicker film, can be prepared for absorbing more photons with less restriction on the poor conductivity of the thicker film. As shown in Figure 5.6, the photocurrent density was found to be  $1.7 \text{ mA/cm}^2$  at the bias voltage of  $-0.55 \text{ V vs. Ag/AgCl}$  which is about ten times of the undoped CuO film with the similar thickness, i.e.  $1.5\text{-}1.7 \text{ }\mu\text{m}$ , which is shown in our previous study (Chapter 4 and Chiang et al., 2011).

Figure 5.7 is the Mott-Schottky plot for CuO-ITO electrodes in  $1\text{M KOH}$  electrolyte. The value of  $N_D$  was calculated based on assuming  $10.26$  as the dielectric constant of CuO (Nakaoka et al., 2004). An apparent difference in the slopes, which corresponds to the charge carrier density, was observed. The  $2 \text{ at\% Li}$  doped CuO electrode showed the lowest slope corresponding to the highest charge carrier density, i.e.  $4.2 \times 10^{21} \text{ cm}^{-3}$ , which is almost double comparing to the charge carrier densities of other doping conditions, i.e.  $1.7 \times 10^{21} \text{ cm}^{-3}$  to  $2.3 \times 10^{21} \text{ cm}^{-3}$ . Comparing this number with values in the literature, it is higher than CuO sintered powder and sol-gel method prepared CuO film, i.e.  $\sim 10^{18} \text{ cm}^{-3}$ , by Koffybery and Benko (1982) and by Chauhan et al.(2006) respectively. It is also higher than electrodeposited CuO film, i.e.  $10^{20} \text{ cm}^{-3}$ , by Nakaoka et al.(2004) and wet chemical method prepared by Chiang et al.(2012b and Chapter 6). However, the charge carrier density has the same order of magnitude in our FSP made none doped CuO-ITO electrode (Chapter 4 and Chiang et al., 2011). The high carrier charge density found in the study also confirmed by the higher photocurrent density result. The flatband potential was found to be around  $0.1$  to  $0.3 \text{ V vs. Ag/AgCl}$  at  $\text{pH } 14$  that included the  $(k_B T/e)$  term.

In the literature, the flatband potentials were known as 0 V (Schultze and Lohrengel, 2000) and 0.3 V (vs. SCE) p-CuO (Hardee and Bard, 1977).

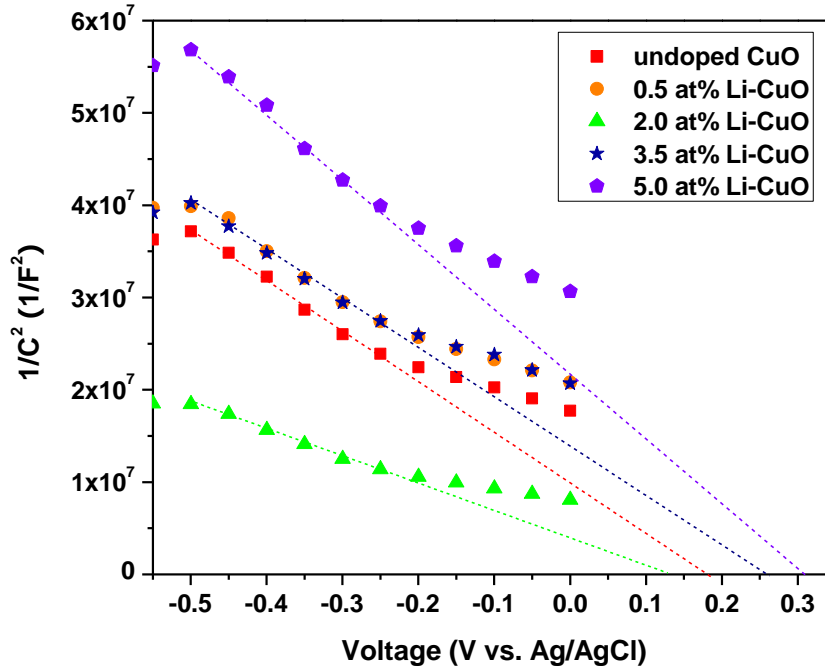


Figure 5.7. The Mott-Schottky plot for Li doped CuO-ITO electrode sintered at 450 °C for 1hr in 1M KOH electrolyte.

**Conversion Efficiency.** The solar conversion efficiency ( $\eta_c$ ) or efficiency of photon-to-hydrogen generation (Eq. 5.6) can be used to judge the efficiency of the PEC cell.

$$\eta_c = \frac{j_p(E_{rev}^0 - V_{bias})}{I_0} \times 100\% \quad (5.6)$$

where  $j_p$  is photocurrent density at a certain applied voltage,  $E_{rev}^0$  is the standard water splitting reaction potential (1.23 V vs. NHE) at pH =0.0,  $I_o$  is the light intensity with unit of  $W/m^2$ , and  $V_{bias}$  (V vs. RHE) is the applied external potential.

For the 2 at% Li doped CuO film electrode with thickness of 1.7  $\mu m$  sintered at 450  $^{\circ}C$  for 1 hr, at the applied voltage of -0.55 V vs. Ag/AgCl in 1M KOH which gave the maximum photocurrent, i.e. 1.69  $mA/cm^2$ , the  $\eta_c$  was calculated to be 1.3%.

## 5.5. CONCLUSIONS

The best photocurrent density and photon-to-hydrogen efficiency found in this Li doped CuO PEC study were 1.69  $mA/cm^2$  and 1.3%, respectively, corresponding to the film prepared by 2.0 at% Li-CuO sintered at 450  $^{\circ}C$  for 1 hr with the thickness 1.7  $\mu m$  at bias voltage of -0.55 V vs. Ag/AgCl in 1M KOH and under 1 sun illumination. This high photocurrent density was further proved by the high charge carrier density, i.e.  $4.2 \times 10^{21} cm^{-3}$ , which is higher than most of prior reports in the literature. The photocurrent density and PEC efficiency are enhanced by a factor of about five to ten by introducing Li into CuO based on film thickness. This is because of the increase in the electrical conductivity of the film from  $2 \times 10^{-6} \sim 4 \times 10^{-6} S/cm$  to  $7 \times 10^{-5} \sim 3 \times 10^{-4} S/cm$  when 2 at% Li was doped.

## Chapter 6

### Copper Oxide Photocathodes Prepared by a Solution Based Process

The results presented in this chapter have been published in the following journal article:

Chiang, C. Y.; Shin, Y.; Aroh, K.; Ehrman, S. "Copper Oxide Photocathodes Prepared by a Solution Based Process" *Int. J. Hydrogen Energ*, **2012**, accepted.

doi:10.1016/j.ijhydene.2012.02.049

#### 6.1. ABSTRACT

Solution based processes are well known by their low-cost trait to fabricate semiconductor devices. In this study, we devised an economical and easily scalable solution based route to PEC cells, taking copper nitrate as the copper ion source and adding an alkali hydroxide, here NaOH, to produce high aspect ratio (3.1 to 9.7) CuO nanoparticles. These CuO particles were used for splitting water and generation of hydrogen via a photoelectrochemical cell. CuO nanoparticle morphology, i.e. rod-like, spindle-like, and needle-like, was dependent on the processing temperature. Sintering the spin coated CuO films improved crystallinity. The band gaps for these films were estimated to be 1.35 eV and 1.64 eV for sintering temperatures of 600 °C and 400 °C for 1 hr, respectively. The porous structure of the nano-sized CuO films increased surface area and thus led to a high photocurrent, i.e. 1.20 mA/cm<sup>2</sup>, for powder prepared at 60 °C and sintered at 600 °C for 1 hr. These films demonstrated 0.91% solar conversion



efficiency at an applied voltage of -0.55 V vs. Ag/AgCl in 1 M KOH electrolyte with 1 sun illumination. The charge carrier density was estimated to be  $6.1 \times 10^{20} \text{ cm}^{-3}$ . This relatively high charge carrier density may be due to the high surface area and short transport distance to the electrode/electrolyte interface in the porous nanostructure.

## 6.2. INTRODUCTION

A photoelectrochemical (PEC) cell is a device that drives an uphill chemical reaction, using solar energy photons so that solar energy is stored as chemical potential energy in the form of the reaction products. The process of making chemical fuels, here hydrogen by solar energy conversion, is a sustainable solution to the energy shortage problem. The PEC water splitting process aims to integrate both solar energy absorption and the hydrogen/oxygen generation function at one photoelectrode. This photoelectrode material must be able to absorb sunlight efficiently and have the right band position to trigger the water splitting reaction. Furthermore, for long term consideration, earth abundant, environmentally benign and inexpensive materials are more favorable for low cost and large scale production.

CuO is a well-known semiconductor with a narrow bandgap, i.e. 0.7-1.6 eV (Schultz and Lohrengel, 2000), which makes it a great candidate for absorbing solar energy. In addition, it is relatively low cost and non toxic and it has a direct band gap which makes it even more attractive. CuO has valence and conduction band edges at -5.00 eV and -3.66 eV respect to the vacuum, respectively (Chapter 4 and Chiang et al., 2011). Thus it can serve as a photocathode to split water into hydrogen, a clean and renewable energy

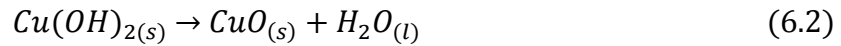
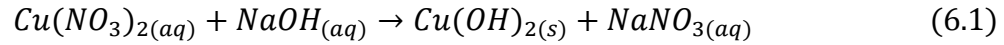
(Barrerca et al., 2009). Since the first reported PEC study published by Fujishima and Honda (1972), numerous studies have been conducted. Over the years, several improvements were made in the materials used for solar energy absorption. Recently, nanosized semiconductor particles have been used in PEC cells. However, the processes used to make these nanosized semiconductor materials are energy intensive (Vijayakumar et al., 2001), or demand expensive raw materials (Borgohain et al., 2000; Zhang et al., 2006) making them difficult to scale up.

Nanostructured oxide semiconductors made by solution based processes have been finding widespread application in inexpensive electronic devices (Han et al., 2009). In this study, we aim to devise an economical route to PEC cells, taking copper nitrate as the copper ion source and adding an alkali hydroxide, here NaOH, to produce CuO. It is an environmentally benign process, generating only water and sodium nitrate which is a widely used ingredient in fertilizer and food preservatives. Furthermore, one possible potential source for  $\text{Cu}^{2+}$  might be aqueous copper solutions generated from purification of waste streams produced during printed circuit board manufacturing and chemical mechanical polishing. Here, for the first time, the hydrogen energy generation potential of CuO nanoparticles produced via this route is explored. By varying the reaction temperature and duration, CuO powders with different morphologies and crystallinity were observed. The powder was washed, spin coated and sintered to make CuO film electrodes and photoelectrochemical characterization of the electrodes was performed.

## 6.3. MATERIALS AND METHODS

### 6.3.1. CuO Particle Formation

Cu-containing solution, i.e.  $\text{Cu}[(\text{NO})_3]_2$  (Strem Chemicals, Inc. USA) with concentration 1M was preheated to the reaction temperatures, i.e. 60 °C and 95°C, and 1M NaOH (Fisher Scientific, USA) was added for the reaction (Eq. 6.1 & Eq. 6.2). The solutions were vigorously stirred for 24 hr at 25 °C, 45 min at 60 °C and 30 min at 95 °C.



The solid/liquid separation was done by vacuum filtration. DI water was first used to wash the solid several times, followed by washing with ethanol. Then, the solid was dried overnight and collected for electrode preparation and chemical analysis.

### 6.3.2. Photoelectrode Preparation

Spin coating was chosen for the film deposition because of its simple operation with good reproducibility. An ultrasonicator (Branson B3, USA) was used to disperse particles in ethanol at a concentration of 30 mg CuO/mL ethanol to decrease the probability of particle aggregation. The deposition of each layer was conducted by a spinner (Headway PWM32 Spinner, USA) at 2000 rpm for 8 seconds on indium-tin-oxide (ITO) coated microscope slides (SPI supplies, USA) with resistance of 8-12 ohms. In order to increase the durability of the films and the crystallinity of CuO, the film electrodes were sintered at 400 °C and 600 °C for 1 hr in a bench-top muffle furnace (Thermo Scientific

Thermolyne, USA).

### 6.3.3. Characterization of PEC Electrode/Cell

The chemical composition of recycled powder was determined by Rietveld analysis of X-ray diffraction (XRD), patterns obtained using a Philips PW 1800 diffractometer with a graphite monochromator and Cu K<sub>α</sub> (λ=1.54 Å) as the incident radiation. The morphology and thickness of the CuO films were studied by a scanning electron microscope (Hitachi SU-70 SEM, Japan) with an acceleration voltage of 3 kV. Cross sections of the films were prepared for the thickness measurements. The transmittance spectra were determined using a UV-vis spectrophotometer (Hitachi, Japan). The absorption coefficient ( $\alpha$ ) of the films was estimated by Eq. 6.3.

$$\alpha = \frac{\left[ \ln \left( \frac{1}{T} \right) \right]}{d} \quad (6.3)$$

where  $\alpha$  is absorption coefficient (1/m),  $T$  is transmittance of the film, and  $d$  is the film thickness (m). The bandgap of the CuO films can be determined by the Tauc plot, i.e.  $(\alpha h\nu)^2$  against photon energy ( $h\nu$ ) with  $n=1$  for direct transition of CuO as shown in Eq. 6.4.

$$\alpha h\nu = A(h\nu - E_g)^{n/2} \quad (6.4)$$

where  $A$  is a constant,  $h$  is Planck's constant,  $\nu$  is the frequency of light, and  $E_g$  is the optical bandgap. The photoelectrochemical performance was determined by the current density at both dark and illumination conditions with a three-electrode configuration in 1M KOH (pH14) electrolyte. Ag/AgCl in saturated KCl (Gamry Instruments, USA) and

platinum gauze (52 mesh, 99.9%, Sigma-Aldrich, USA) were chosen as reference electrode and counter electrode, respectively. The configuration of the cell and the CuO photocathode structure are shown in Figure 6.1. The reactor was made by quartz plates (Chemglass, USA). The electrode with area of  $2.25 \text{ cm}^2$  was scanned from 200 mV to -700 mV vs. Ag/AgCl. The light source was a 150 W full spectrum solar simulator (Oriel Instruments, USA), coupled with a full reflector beam turning mirror (Oriel Instruments, USA) and a AM1.5G filter with a measured intensity of 1 sun ( $1000 \text{ W/m}^2$ ) by a reference cell (Oriel instrument, USA) at  $25^\circ\text{C}$ .

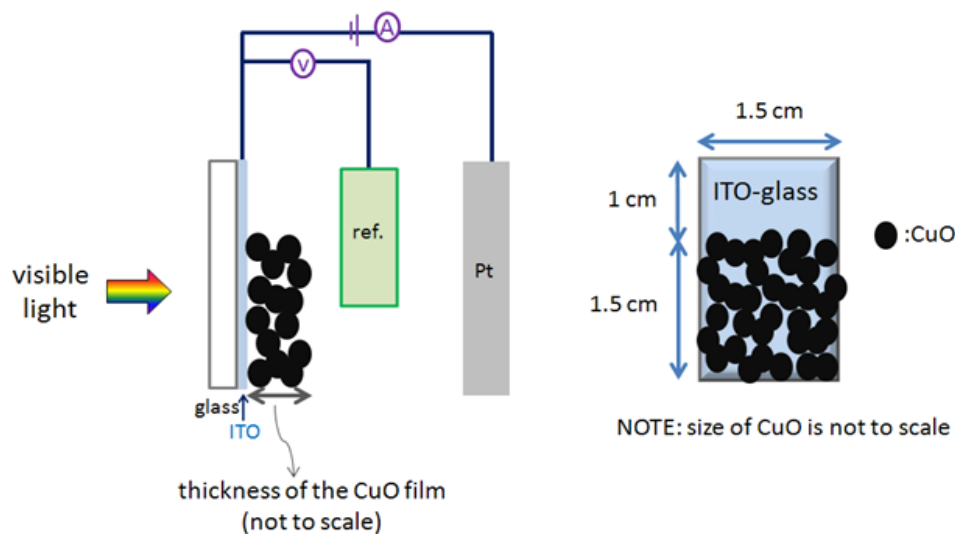


Figure 6.1. The configuration of the cell and the CuO photocathode structure.

The potentiostat (eDAQ, Australia) was used to apply the bias voltage and to measure the current. Furthermore, to know the flatband potential and charge carrier density, the required Mott-Schottky analysis was done by the AC impedance measurement (Solartron, USA). It was performed in the dark at AC amplitude of 5 mV and a frequency of 1 kHz

(Nakaoka et al., 2004) with a three-electrode system. The capacity can be calculated by the following equations based on the imaginary part of the impedance ( $Z''$ ),

$$Z = Z' + iZ'' \quad (6.5)$$

$$Z'' = -\frac{i}{\omega C} = -\frac{i}{2\pi f C} \quad (6.6)$$

where  $Z$  is the impedance,  $Z'$  is the real part of impedance,  $C$  is capacitance,  $f$  is AC frequency in Hertz. Based on the Mott-Schottky plot ( $1/C^2$  versus  $V$ ), the flatband potential ( $V_{fb}$ ) can be obtained by the intercept of x axis and from the slope, the carrier density ( $N_A$ ) can be obtained.

$$\frac{1}{C^2} = \left( \frac{2}{e\epsilon\epsilon_0 A^2 N_A} \right) \left[ (V - V_{fb}) - \frac{k_B T}{e} \right] \quad (6.7)$$

where  $e$  is the electronic charge,  $\epsilon$  is dielectric constant of CuO,  $\epsilon_0$  is the permittivity of vacuum,  $A$  is the surface area of the porous film,  $V$  is the applied voltage,  $k_B$  is Boltzmann's constant,  $T$  is the absolute temperature where  $(k_B T/e)$  is a temperature-dependent correction term.

#### 6.4. RESULTS AND DISCUSSION

The precipitation of  $\text{Cu}^{2+}$  from the solution is almost complete based on the absorbance of  $\text{Cu}^{2+}$  response. Powder samples produced by reaction at 25 °C needed a day to reach 79% CuO conversion based on the powder composition obtained from Rietveld refinement analysis of the XRD result shown in Figure 6.2. Because reaction rates of

$\text{Cu}^{2+}$  with the base highly depend on the reaction temperature in the system, a water bath was introduced to keep the solutions at higher temperatures of 60 °C and 95 °C for 45 min and 30 min, respectively to reach about 70% CuO formation. Non-CuO components in the powder are  $\text{Cu}_2(\text{NO}_3)(\text{OH})_3$ , which likely results from the partial decomposition of copper nitrate, and trace amounts of  $\text{Cu}(\text{OH})_2$ . These compounds might play a role in maintaining porosity during the film preparation process, which will be discussed later.

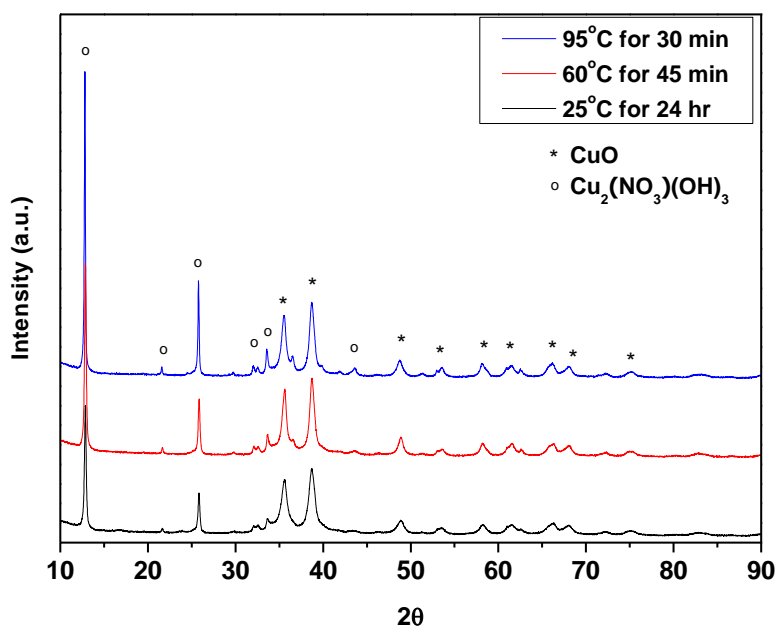


Figure 6.2. X-ray diffraction patterns of CuO powders as prepared.

Based on the morphologies observed from TEM micrographs (Figure 6.3), the particles produced at 25 °C tended to have a higher aspect ratio ( $9.7 \pm 4.9$ ) with rod-like shapes, 0.2  $\mu\text{m}$  to 2  $\mu\text{m}$  in length and about 50 nm in width (Figure 6.3a). As the temperature

increased to 60 °C, the aspect ratio decreased to  $3.1 \pm 1.2$  and the morphology was spindle-like (Figure 6.3b). Upon further increase in the temperature to 95 °C, needle-like shaped particles were observed and the particle length decreased significantly to tens of nanometers (Figure 6.3c).

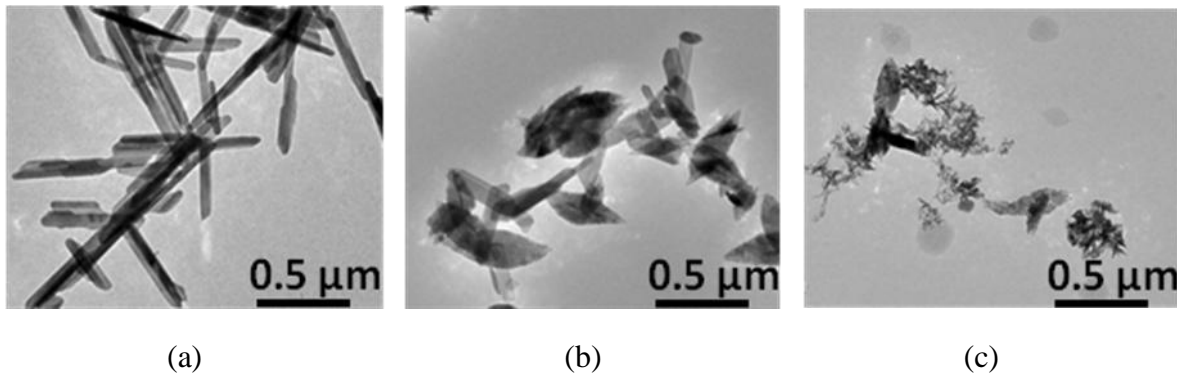


Figure 6.3. Transmission electron micrographs of samples produced at different temperature and duration: (a) 25 °C for 24 hr, (b) 60 °C for 45 min, (c) 95 °C for 30 min.

In Figure 6.4, film morphology changes based on the sintering temperature are shown. For samples sintered at 200 °C, the particle shapes are more similar to as reacted powder but with smaller aspect ratio because of the thermodynamic preference for minimizing the surface area of particles. Also, at this point, the film still contained  $\text{Cu}_2(\text{NO}_3)(\text{OH})_3$  impurity based on XRD and Rietveld refinement analysis for the trace amount of impurity which might not be easily seen in Figure 5 because of the scale. As the sintering temperature increased to 400 °C, based on the XRD result, pure CuO film was formed (Figure 6.5). The particles now have much smaller aspect ratio as seen in SEM and better



crystallinity as determined from narrowness of peaks in XRD compared to the samples at lower sintering temperature. By sintering the samples further to 600 °C, nearly spherical particles were formed; the composition of the films and the crystallinity were confirmed by XRD to be pure highly crystalline CuO nanoparticles. Also, all the samples sintered at 600 °C have porous structures as shown in Figure 6.4. Those pores might have resulted from the decomposition of the Cu-containing impurities from the reacted powder as they convert to CuO, and the resulting particle shape change during the sintering process.

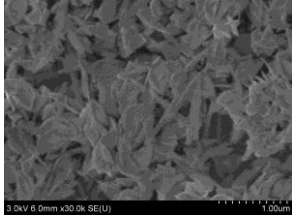
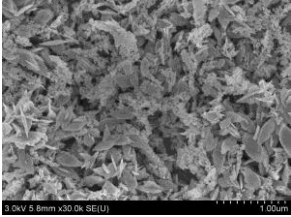
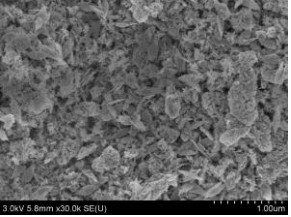
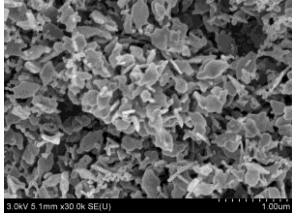
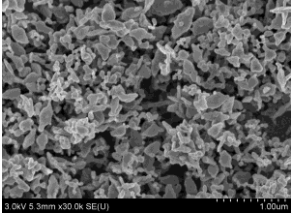
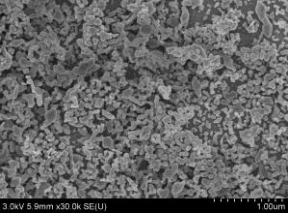
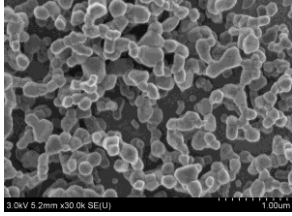
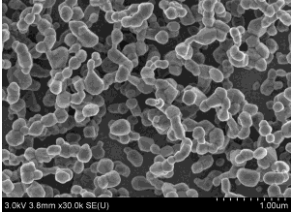
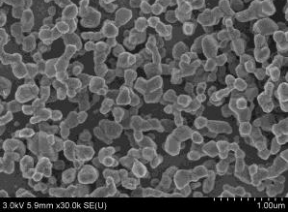
Sinter temperature	Reaction temperature		
	25 °C	60 °C	95 °C
200 °C			
400 °C			
600 °C			

Figure 6.4. Scanning electron micrographs of samples produced at 25 °C, 60°C, and 95°C and sintered at 200°C, 400°C and 600°C for 1 hr.

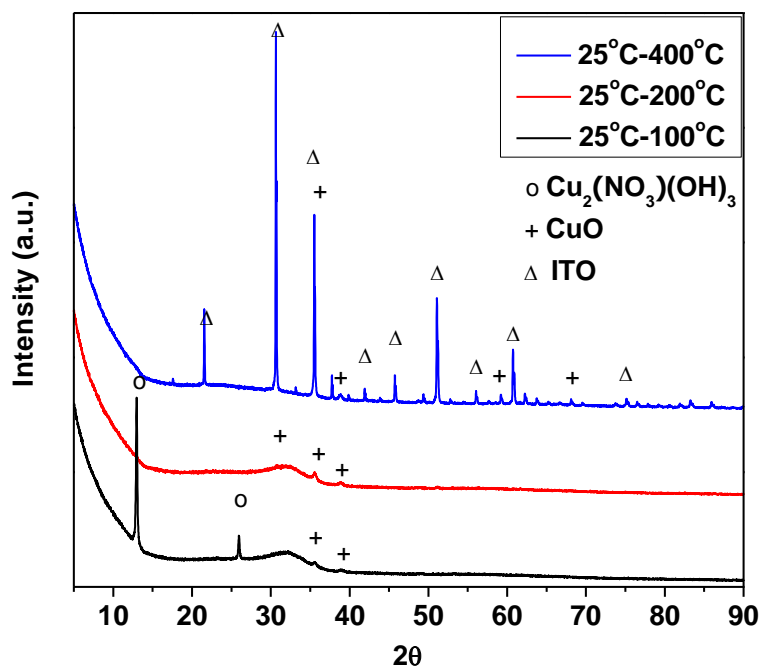


Figure 6.5. X-ray diffraction patterns of CuO films sintered at different temperatures.

The bandgap of the CuO samples was determined by the interception of the axis of photon energy ( $h\nu$ ) in the  $(\alpha h\nu)^2$  vs.  $(h\nu)$  plot as shown in Figure 6.6. For samples sintered at 400 °C with average primary particle diameter of  $98\pm 39$  nm and crystalline size of 30 nm, the bandgap was calculated to be 1.65 eV; for samples sintered at 600 °C with average primary particle diameter of  $178\pm 48$  nm and crystalline size of 110 nm, the bandgap decreased to 1.35 eV. The crystalline size dependent character for bandgap of CuO electrodes is also illustrated in the literature (Nakaoka et al., 2004) where the crystalline size varies from 12 to 41 nm with band gap changing from 1.56 to 1.38 eV, respectively. Not only size but also morphology and crystallinity of nanocrystals affect the optical absorption peak (Yang et al., 1995; Lu et al., 2005; Zhang et al., 2005; Yang

et al., 2007). It has been reported in the literature that the increase in crystal size and improvement of crystallinity results in a red shift (Zhang et al., 2005; Yang et al., 2007). As in our case, as sintering temperature increased, the resultant red-shift also led to a smaller bandgap.

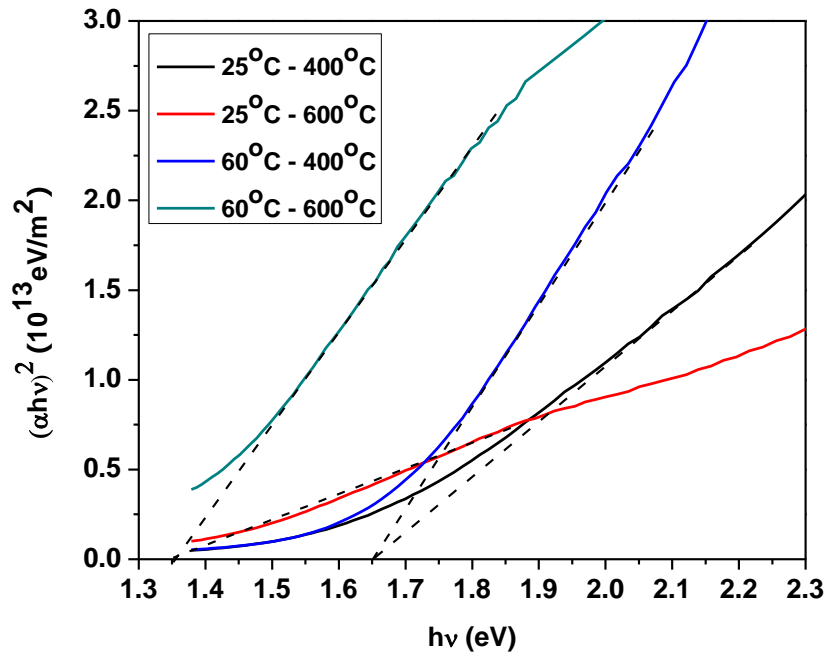
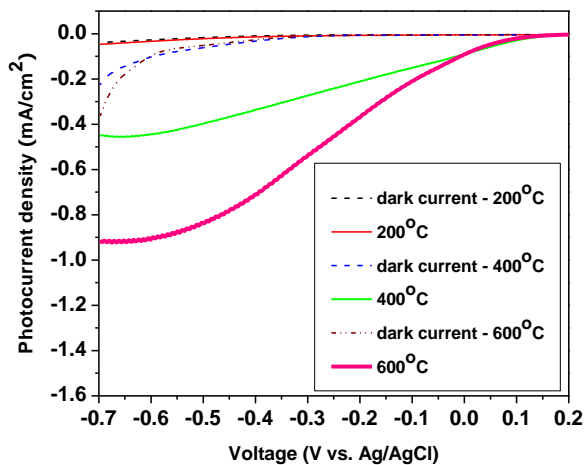


Figure 6.6. The relationship between  $(\alpha h\nu)^2$  and  $(h\nu)$  for CuO powder prepared under different reaction conditions and their films sintered at different temperature. The first temperature in the caption is the solution reaction temperature and the second one is the powder sintering temperature.

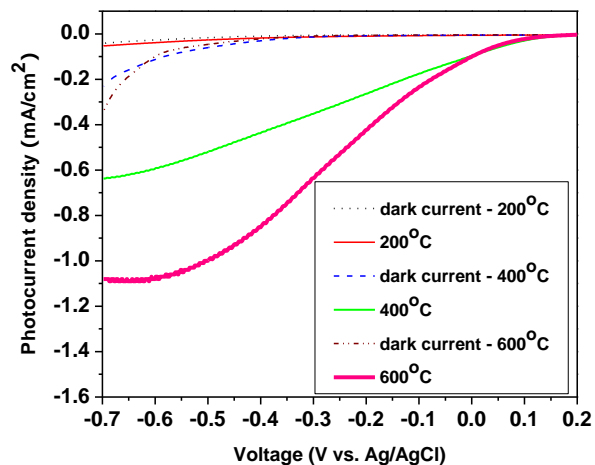
One of the most important characteristics for a PEC material is the crystallinity. If the samples are not crystalline or contain many defects, the photon generated electron and hole pairs might recombine easily. In our case, there was almost no photocurrent

observed for samples sintered at 200 °C, as shown in Figure 6.7, because of the  $\text{Cu}_2(\text{NO}_3)(\text{OH})_3$  impurity and poor crystallinity. However, as sintering temperature increased to 400 °C, apparent photocurrents, i.e. 0.45~0.6 mA/cm<sup>2</sup> under bias voltage of -0.55 V vs. Ag/AgCl, were observed for all samples independent of the reaction temperatures. When the sintering temperature further increased to 600 °C, the better crystallinity was reached and the structure appeared more open as seen in the SEM (Fig. 4). The photocurrents were nearly doubled, i.e. 0.85~1.1 mA/cm<sup>2</sup> under bias voltage of -0.55 V vs. Ag/AgCl, compared to the samples sintered at 400 °C.

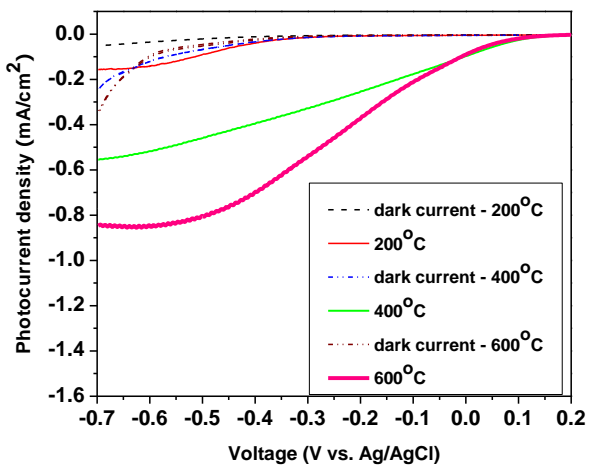
Based on Figure 6.7, better photo-response was observed for powder prepared at 25 °C and 60 °C. So, further studies were focused on these two sets of processing conditions. In Figure 6.8, the thickness of the film was considered. Powders prepared at different temperatures had different sizes and morphology. For the reaction at 25 °C, because of the large particle size and high aspect ratio, each layer deposited by spin coating had an average thickness of 223 nm. For reaction at 60 °C, particle size and aspect ratio were smaller, so each layer deposited by spin coating led to an average thickness of 168 nm. In Figure 8, the best photocurrent among the 25 °C samples was observed at 6 layers which gave a total thickness of about 1340 nm. The best photocurrent for samples prepared at 60 °C was observed at 8 layers which also gave the thickness of 1340 nm. This observation might be explained by the decrease in the resistance of the film when the thickness of the film decreases and the increase in the film thickness may increase absorbance of solar energy. Thus, an increase in the thickness led to a higher resistance of the film, which might decrease the efficiency of charge carrier transport but meanwhile it also increased absorbance of solar energy, which could enhance the efficiency.



(a)

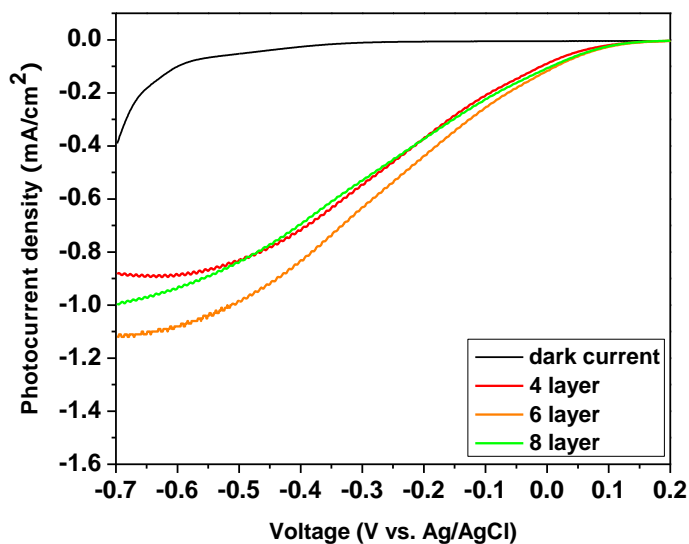


(b)

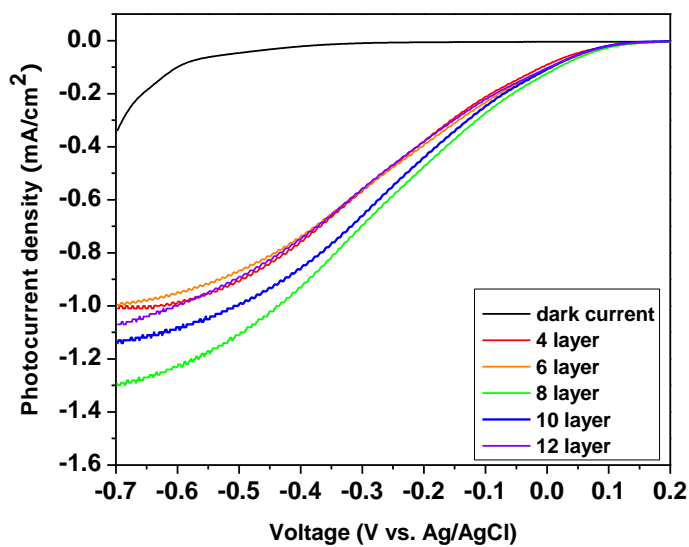


(c)

Figure 6.7. Current-potential (I-V) characteristics curve for 4 layered CuO/ITO electrodes sintered at different temperatures in the dark and under illumination in a 1 M KOH electrolyte: (a) powder prepared at 25 °C, (b) powder prepared at 60 °C, (c) powder prepared at 95 °C.



(a)



(b)

Figure 6.8. Current-potential (I-V) characteristics curve of different thickness of CuO/ITO electrodes: (a) powder prepared at 25 °C and sintered at 600°C, (b) powder prepared at 60°C and sintered at 600°C.

Figure 6.9 shows the Mott-Schottky plot for a CuO/ITO electrode in 1 M KOH electrolyte. Flatband potential was obtained by the calculation of the intersection of the line fit to the  $1/C^2$  measurements with the x-axis and the charge carrier density was determined by the slope. Considering the  $(k_B T/e)$  term, flatband potential of this CuO film is 0.21 V vs. Ag/AgCl, and the charge carrier density is  $6.1 \times 10^{20} \text{ cm}^{-3}$  assuming the dielectric constant of CuO is 10.26 (Nakaoka et al., 2004), the porosity of the film is 57% and the surface area of the porous film is  $2.31 \times 10^{-3} \text{ m}^2$  which was estimated based on the distribution of copper oxide particles in the side views of the film which was shown in Figure 6.10. By assuming the CuO particles are deposited uniformly on the film, the fractional area of the CuO from the cross section surfaces can represent the entire volume. Thus by calculating the fractional area of CuO in the cross section surface from the SEM images, the porosity can be estimated (Chapter 4 and Chiang et al., 2011).

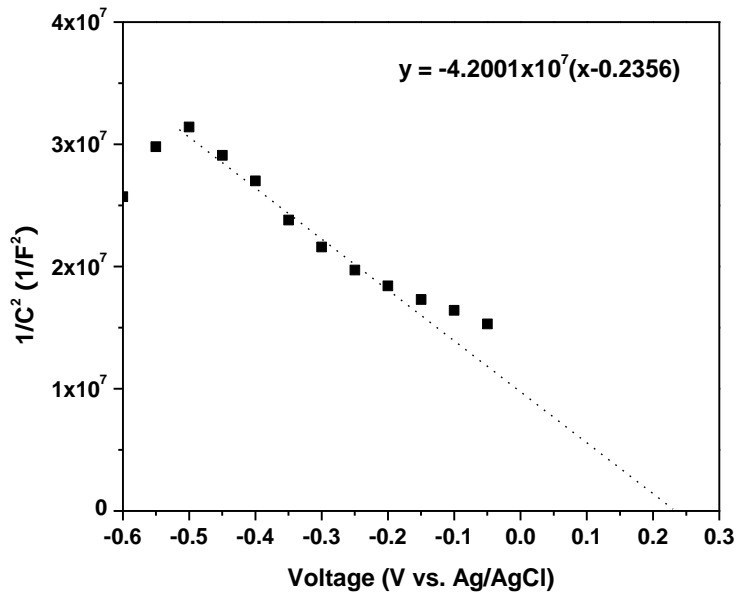
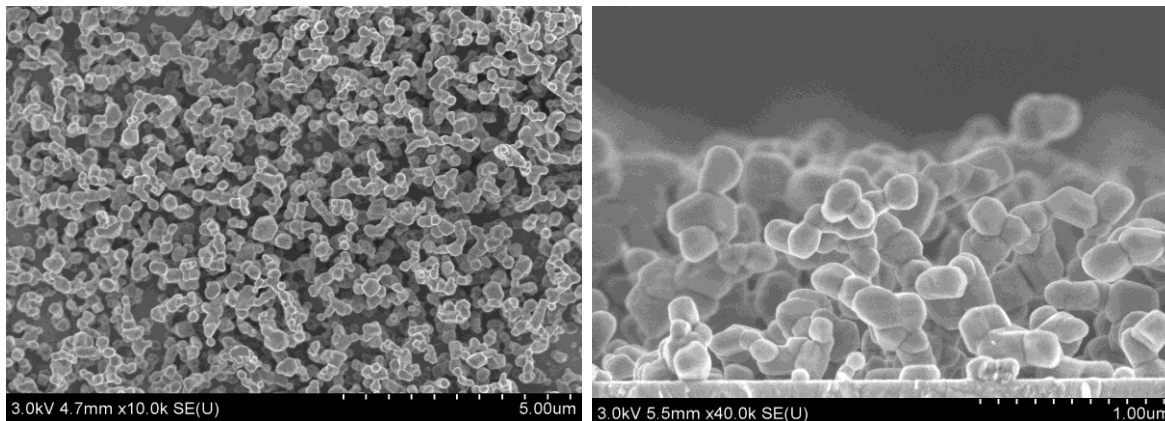


Figure 6.9. Mott-Schottky plots for a CuO/ITO electrode in 1 M KOH electrolyte.



Bird-eye view

Side view

Figure 6.10. Scanning electron micrographs of the bird-eye view and side view of sample prepared at 60 °C and sintered at 600 °C.

Comparing the charge carrier density in this CuO sample with values in the literature, it is higher than the  $4.0 \times 10^{20} \text{ cm}^{-3}$  CuO film prepared by electrodeposition (Nakaoka et al., 2004), the  $4.0 \times 10^{18} \text{ cm}^{-3}$  of CuO film prepared by sintering CuO powder (Koffyberg and Benko, 1982), and  $2 \sim 43 \times 10^{18} \text{ cm}^{-3}$  by the sol-gel method (Chauhan et al., 2006). However, it is lower than the 2 at% Li doped CuO film (Chapter 5 and Chiang et al., 2012c) which has charge carrier density of  $4.2 \times 10^{21} \text{ cm}^{-3}$ . The relatively high charge carrier density among those undoped CuO film also may have contributed to the high photocurrent density in our CuO PEC cell. This high charge carrier density and photocurrent density may be explained by the short distance for the charge carriers to transport to the electrode/electrolyte interface, because of the interpenetration of the electrolyte into the porous CuO nanostructure.



The position of the valence band edge with respect to the vacuum level is denoted here by  $D$ ,

$$D = V_{fb} + 4.64 + \Delta E_F + V_H \quad (6.8)$$

where 4.64 represents the absolute potential of Ag/AgCl below the vacuum level,  $\Delta E_F = E_F - E_V$  which is the difference between Fermi level and the valence band edge

$$\Delta E_F = E_F - E_V = kT \ln \left( \frac{N_A}{N_V} \right) \quad (6.9)$$

where  $N_V$  is the effective density of states in valence band and can be calculated based on Eq. 6.10.

$$N_V \equiv 2 \left( \frac{2\pi m^* kT}{h^2} \right)^{3/2} \quad (6.10)$$

where  $m^*$  is the effective mass.

The Helmholtz potential between CuO electrode and electrolyte is  $V_H = 0.059(P_0 - pH)$ . However, since the flatband potential was determined at the experimental value of  $P_0$ ,  $V_H$  can be neglected (Koffyberg and Benko, 1982). With  $V_{fb} = 0.21 V$  (vs. Ag/AgCl) at pH 14 and  $m^* = 7.9m_0$  (Ito et al., 1998) where  $m_0$  is electron rest mass,  $D$  can be obtained with the value of 4.85 eV (below vacuum level). Since the bandgap of the CuO electrode used is 1.35 eV, the conduction level should lie at 3.50 eV (below vacuum level). The energy band scheme for CuO in this study and CuO in prior reports in the literature (Chapter 4 and Chiang et al., 2011; Nakaoka et al., 2004; Koffyberg and Benko, 1982) was illustrated in Figure 6.11 with all values adjusted to pH 14 electrolyte. All the

studies showed that the band edges of CuO electrodes (-4.8 to -5.3 for valence band edge and -3.3 to -3.8 for conduction band edge) matched the water splitting to hydrogen redox potential.

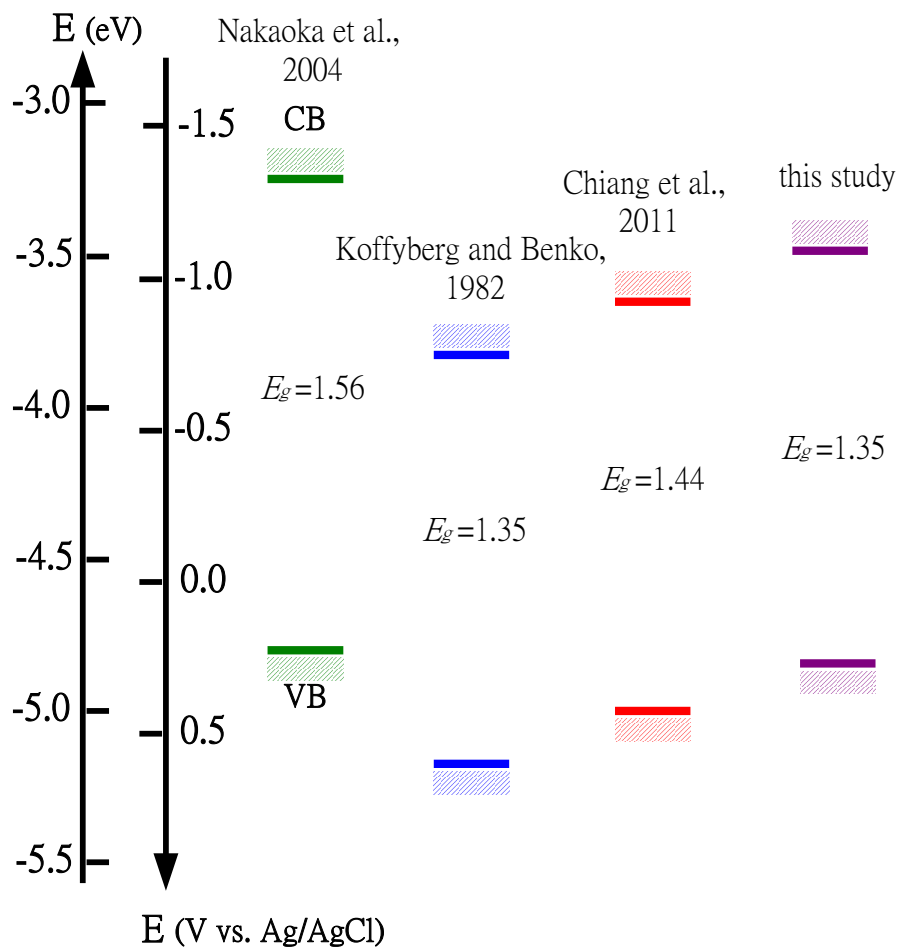


Figure 6.11. Estimated position of CuO bandedges for this study, performed at pH 14, and prior reports in the literature (Chiang et al., 2011; Nakaoka et al., 2004; Koffyberg and Benko, 1982) adjusted to pH 14.

The conversion efficiency of PEC cells can be calculated by solar conversion efficiency ( $\eta_c$ ), the ratio of the power used for water splitting to the input light power (Eq. 6.11) (Bak et al., 2002).

$$\eta_c = \frac{j_p(E_{rev}^0 - V_{bias})}{I_0} \times 100\% \quad (6.11)$$

where  $j_p$  is photocurrent density at a certain applied voltage,  $E_{rev}^0$  is the standard water splitting reaction potential (1.23 V vs. NHE) at pH =0.0,  $I_0$  is the light intensity with unit of W/m<sup>2</sup>, and  $V_{bias}$  (V vs. RHE) is the applied external potential.

Also with the conversion of Ag/AgCl reference electrode to the reversible hydrogen electrode (RHE) (Eq. 6.12) (Kay et al., 2006), the applied external potential and the effect of pH of electrolyte can be converted into the potential vs. RHE.

$$E_{RHE} = E_{AgCl} + E_{AgCl}^0 + 0.059pH \quad (6.12)$$

where  $E_{AgCl}^0 = 0.197$  V at 25°C. For example, when the  $V_{bias} = -0.55$  V (vs. Ag/AgCl) at pH14 electrolyte,  $V_{bias}(V \text{ vs. RHE}) = -0.55 + 0.197 + 0.059 \times 14 = 0.473$  V.

For the CuO film electrode made from powder prepared at 60 °C and sintered at 600 °C for 1 hr, at the applied voltage of -0.2 V vs. Ag/AgCl in 1M KOH, the photocurrent was found to be 0.50 mA/cm<sup>2</sup> and  $\eta_c$  was calculated to be 0.20%. At the applied voltage of -0.55 V vs. Ag/AgCl in 1M KOH which gave the maximum photocurrent, i.e. 1.20 mA/cm<sup>2</sup>, the  $\eta_c$  was calculated to be 0.91%. These calculations were based on the average of the three experimental results with fairly good reproducibility, with difference between samples less than 5% in each case.

## 6.5. CONCLUSIONS

We successfully made CuO nanoparticles by a solution based process and used these to prepare photoactive porous nanostructured CuO thin film electrodes for hydrogen generation via a photoelectrochemical cell. The particle and film morphologies were well controlled in the processes. The porous structure of the CuO film made by this process (powder prepared at 60 °C and sintered at 600 °C for 1 hr) had increased surface area and a high photocurrent and charge carrier density, i.e. 1.20 mA/cm<sup>2</sup> and 6.1×10<sup>20</sup> cm<sup>-3</sup> respectively. These films were demonstrated to have 0.91% solar conversion efficiency at applied voltage of -0.55 V vs. Ag/AgCl in 1 M KOH electrolyte with 1 sun (AM1.5G) illumination.

## Chapter 7

### Biological Templates for Anti-reflectance Surface and Current Collectors for Photoelectrochemical Cell Applications

#### 7.1. ABSTRACT

Structures with a scale comparable to the wavelengths of the major useful solar spectrum are the ideal design for decreasing the light reflection. The nanostructures can shorten the charge carrier transport distance by three dimensional (3D) structures such as nanowires, nanotubes, and nanorods and thus can be expected to highly increase the efficiency. In this study, self-assembly of genetically modified tobacco mosaic virus (TMV1cys) was used to form 3D structures for preparing the current collectors as well as the low light reflecting surface. CuO was deposited by sputtering on this patterned nanostructure. The CuO thickness of 520 nm on the patterned current collectors showed the highest photocurrent density, 3.15 mA/cm<sup>2</sup>, among the studies in the literature. This might be explained by reducing charge carrier transport distance by the 3D current collectors, the suppression of light reflection by introducing the nanorods with distance of about 500 nm, and decreasing the recombination in the particle by decrease the CuO particle dimensions to the nanoscale.

## 7.2. INTRODUCTION

Currently, over 80% of the world's energy consumption is derived from fossil fuels (Yilanci and Dincer, 2009; Turner et al. 2008); however, this method of electrical generation has posed significant concerns regarding widespread environmental damage. A subsequent, more sustainable alternative to fossil fuels was first presented by Fujishima and Honda when they successfully produced hydrogen from the photoelectrolysis of water using a  $\text{TiO}_2$  semiconducting electrode (Fujishima and Honda, 1972; Barborini et al. 2005). Successful water electrolysis is achieved when the semiconducting electrode material absorbs photons with energy at or greater than its band gap, generating electron/hole pairs (Gratzel, 2001; Khaselev and Turner, 1998; Yilanci and Dincer, 2009; Hensel and Zhang, 2011; Harris, 1978). These electron/hole pairs are collected at the anode and cathode of the solar cell where they drive the redox reactions that produce hydrogen gas, along with the byproduct oxygen gas (Khaselev and Turner, 1998; Gratzel, 2001). This solar cell, more specifically, is called a photoelectrochemical (PEC) cell. As its name implies, three major issues, i.e. photon absorption, electron transport, and redox potential of water splitting reaction, need to be addressed in order to make an efficient PEC cell. Many studies have focused on the nanostructures to shorten the charge carrier transport distance by introducing a three dimensional (3D) structures such as nanowires, nanotubes, and nanorods (Kongkanand et al., 2007; Faglia et al., 2009; Li and Zhang, 2010). However, in PEC studies, people seldom look into the efficient utilization of incident light, meaning decreasing the reflection by mimicking the surface structure of nature structures such as moth eye. For the next generation solar

cells, the structures with a scale comparable to the wavelengths of the majority of the useful solar spectrum are the ideal design (Zhu et al., 2010).

For preparing the nanostructure, a growing interest in harnessing the self-assembly and inorganic binding capabilities derived from biological materials, especially the novel bioinorganic interfaces of the genetically tractable virus (Shenton et al., 1999; Fowler et al., 2001; Dujardin et al., 2003; Royston et al., 2008). By taking the advantage of such interfaces, viruses have been scaffolded into battery electrode materials, conductive nanowires, and memory devices (Chen et al., 2010; Royston et al., 2008; Tseng et al., 2006). In the previous study of our team, a genetic modified tobacco mosaic virus (TMV), with length of 300 nm and outer diameter of 18 nm, can be easily patterned on gold substrate forming nanoscaled 3D structures (Royston et al., 2008). The introduce of cysteine residues in the coat protein of TMV enables patterning of the virus onto gold substrate and enhances the nickel coating in electroless plating process because of the strong covalent-like interactions between thiol groups of cysteines and metal ions (Royston et al., 2008; Chen et al., 2010). With the help of high aspect ratio TMV structures, a 3D current collector can be made and the transport distance for a photon-excited charge carrier from the photoactive material coated around the current collector is expected to be significantly reduced. It also expands the available surface area for photon absorption to increase water electrolysis reactions. More important, by carefully choosing the distance of these nano-rod 3D structures to show periodicity shorter than the wavelength of majority useful photons, this can suppress the reflection of the light and thus increase the photon utilization.

In order to demonstrate this concept, CuO, a small band gap material with band gap around 1.4-1.8 eV (Ghosh et al., 2000) was chosen since it can absorb about half of the solar irradiation on the ground and have sufficient energy to overcome the overpotential and successfully split water. One of the main limitations of its efficiency is the fast recombination of photon generated charge carriers. In our previous studies (Chapter 4 and Chiang et al., 2011), under AM1.5G with 1 sun irradiation, the use of nano size CuO particles successfully increased the photocurrent density to 1.20 mA/cm<sup>2</sup> by reducing the possible recombination in the large CuO particle itself (Jeong and Choi, 1996). Furthermore, porous CuO thin film electrodes were introduced to further decrease the charge carrier transport distance to the electrode/electrolyte surface for the water splitting and they demonstrated increased photocurrent density to 1.20-1.58 mA/cm<sup>2</sup> (Chapter 6 and Chiang et al., 2012b; Chiang et al., 2012d) comparing to other studies with photocurrent densities of 0.08-0.44 mA/cm<sup>2</sup> (Koffyberg and Benko, 1982; Nakaoka et al., 2004). However, during these processes, multiple steps were needed for photocathode preparation, i.e. the nanoparticles were produced first and then spin coated to form the film followed by an annealing treatment. With each high temperature heat treatment, particle growth can be expected, potentially resulting in lower efficiency.

Magnetron sputter deposition thus gives a chance for producing small crystalline size CuO particles and the flexibility to deposit films on many different kinds of nanostructures. It can be used to produce micro and nanostructural multilayers with different monolayer thicknesses (Petrantoni et al., 2010). RF sputtering can be used for the deposition of copper oxide because of its ability to produce evenly dispersed, low resistance thin films (Parretta, 1996). Thus, in this study, we demonstrated the ITO



coated TMV1cys template can be used as a current collector for a 3D nanocrystalline CuO photocathode deposited by sputtering. To combine the advantage of both small particles with less chance for the charge carrier recombination in the particles and short charge carrier transport distance as well as the nearly anti-reflection structure, this structure might highly increase the photocurrent density because of the increase in the life time of charge carriers and utilization more incident photon.

### **7.3. MATERIALS AND METHODS**

#### **7.3.1. TMV1cys Preparation**

TMV1cys, a coat protein mutant of tobacco mosaic virus (TMV) with outer diameter and length of 18 nm and 300 nm respectively, had been previously genetically engineered by inserting a single codon in the third amino acid position of the TMV coat protein, adding a single cysteine residue to each TMV coat protein subunit (Royston et al., 2008). RNA transcripts of a TMV1cys cDNA clone were used to inoculate *Nicotiana benthamiana*, a TMV host species. Approximately 20 days post-inoculation, symptomatic leaf tissue was harvested and ground in 0.1M pH7 sodium phosphate buffer, which was used to infect tobacco plants, *Nicotiana tabacum*. Virus was then harvested approximately 20 days post-infection and was purified as described in the literature (Gooding and Hebert, 1967). Virus concentration was determined by spectrophotometric measurement of the absorption of the purified virus solution at 260 nm and 325 nm.

### 7.3.2. Self-Assembly and Mineralization

The TMV1cys was self assembled onto gold coated ITO/glass substrates (SPI supplies, USA) by submerging the substrate in  $10^{-4}$ ,  $10^{-2}$ ,  $10^{-3}$  and  $10^{-1}$  mg TMV1cys/mL 0.1M phosphate buffer (pH 7) for 24 hours to allow the virus to vertically attach to the substrate surface via electrostatic interactions between gold and the genetically modified cysteine residues on the amino-terminus (Lee et. al., 2005). The processes of the virus scaffold-CuO photocathode are illustrated schematically in Figure 7.1. The TMV1cys was then activated by palladium catalyst through the reduction of  $\text{Pd}^{2+}$  to  $\text{Pd}^0$  using hypophosphite reducing agent (Royston et al., 2008) where the process is shown in Figure 7.1(B). Nickel was electrolessly deposited on  $\text{Pd}^0$  activated virus surface by placing the substrate in a 0.1M  $\text{NiCl}_2$  solution containing 0.25M glycine, 0.15M sodium tetraborate ( $\text{Na}_2\text{B}_4\text{O}_7$ ), 0.5M dimethylamino borane (DMAB) and water. Here, DMAB served as a reducing agent and the substrate was immersed in the nickel plating solution until the substrate surface had darkened which is about 3 min (shown in Figure 7.1(C)). Then, the substrate was dipped in a beaker of ethanol to dislodge any remaining uncoated TMV viruses on the substrate surface (Royston et al., 2008) and dried in a furnace at 300 °C for 1 hr. This also helps to oxidize both nickel metal and the TMV1cys scaffold to prevent the structure change, i.e. volume expansion, during the post annealing after the sputter deposition of ITO and CuO.

### 7.3.3. Sputtering ITO and CuO

The substrates were covered by aluminum foil on the side without TMV1cys coated, 0.5 cm × 0.8 cm, to prevent the CuO deposition because this area would be used for the

external circuit connection (shown in Figure 7.1). The photoactive CuO layer with thickness from 170 nm to 1030 nm and the conducting layer ITO with thickness of 60 nm were deposited on the substrates by the reactive magnetron sputtering technique (AJA International ATC 1800-V) at chamber pressure of 5 mTorr. The ITO target (purity 99.99%, AJA International) was d.c. sputtered under argon plasma at 200 W with an argon flow rate of 17 sccm. The Cu target (purity > 99.999%, AJA International) was r.f. sputtered under argon and oxygen plasma at 300 W with oxygen and argon flow rates of 3 sccm and 17 sccm, respectively. Both targets were placed 111 mm from the substrate. During the sputter process, the chuck was rotated to achieve uniform deposition. After the sputter deposition of copper oxide, the films were annealed in air at 450 °C for 1 hour to increase the crystallinity of CuO. A schematic of the final CuO electrode structure is shown in Figure 7.1(D).

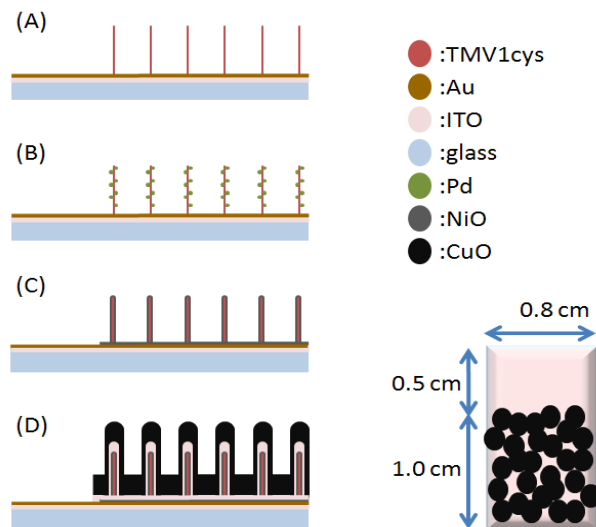


Figure 7.1. Diagram of the assembling processes for CuO photocathode with a final bird-eye view illustration: (A) TMV1cys self-assembly onto Au coated substrate, (B) Pd activated the virus surface, (C) Ni uniformly coated on the virus surface, and (D) sputter deposition of ITO and CuO.

#### 7.3.4. Analysis

The compositions of the thin films were characterized by X-ray diffraction (XRD) using a Philips PW 1800 diffractometer with a graphite monochromator and with Cu  $K_{\alpha}$  ( $\lambda=1.54 \text{ \AA}$ ) as the incident radiation. The morphology and thickness of the film were analyzed using a Hitachi SU-70 SEM with 3 kV as the acceleration voltage. The CuO photocathode structure and composition was determined by a field emission gun transmission electron microscope (FEG-TEM) (JEOL JEM 2100F), energy dispersive x-ray spectrometer (EDS) (Oxford INCA 250), and a scanning image observation device for the scanning transmission electron microscope (STEM). The film reflectance was measured by an UV-vis spectrophotometer (Perkin Elmer Lambda 35, USA). PEC studies were conducted by a potentiostat (eDAQ, Australia) in 1M KOH (pH 14) electrolyte under both dark and illumination conditions with a three-electrode configuration. CuO semiconductor films were used as a working electrode, while Ag/AgCl in saturated KCl (Gamry Instruments, USA) and platinum gauze (52 mesh, 99.9%, Sigma-Aldrich, USA) were chosen as reference electrode and counter electrode, respectively. A 150 W full spectrum solar simulator (Oriel Instruments, USA) coupled with a full reflector beam turning mirror (Oriel Instruments, USA) and a AM1.5G filter was used for the standard solar energy input measured intensity of 1 sun ( $1000 \text{ W/m}^2$ ) by a reference cell (Oriel instrument, USA) at  $25^{\circ}\text{C}$ . The configuration of the cell can be found in our previous publication (Chapter 6 and Chiang et al., 2012b).

#### 7.4. RESULTS AND DISCUSSION

The thickness of the nickel coated TMV1cys after heat treatment at 300 °C for 1 hr in air was estimated to be about 20 nm and thus gave about 70 nm for the overall diameter of the template as shown in Figure 2. It can be seen in the figure that the crystalline nickel oxide (NiO) encased the virus template uniformly.

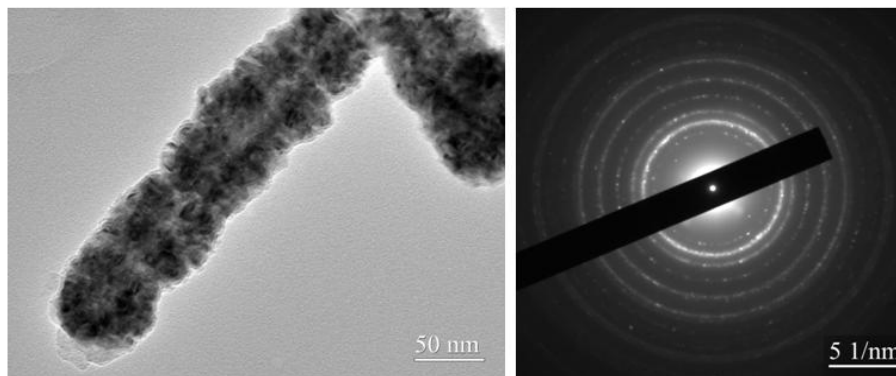


Figure 7.2. TEM image of nickel-coated TMV1cys after heat treatment at 300 °C for 1 hr.

After the sputter deposition of ITO and CuO for 4 min (corresponding to the thickness of 60 nm) and 15 min (which is about 520 nm), respectively, the image of one nanorod is shown in Figure 7.3 along with the line scan EDS analysis for intensity of different elements, i.e. Ni, In, Sn, and O, based on the position. A strong single of nickel from NiO was found in the center of the rod and surrounded by indium and tin which came from the ITO layer. The outer diameter of the ITO layer was estimated to be 130 nm. Because of the TMV copper grid, the oxygen signal was chosen to demonstrate the CuO

concentration at the outer most layer and this layer was further proved to be CuO by XRD as shown in Figure 7.4. The uniform ITO and CuO deposition indicate the relatively vertical orientation of the virus on the gold surface because of the thiol group-gold interaction. Specifically, the 1cys genetic modification is only surface-accessible at the 3' end of the virus rod (Chen et al., 2010).

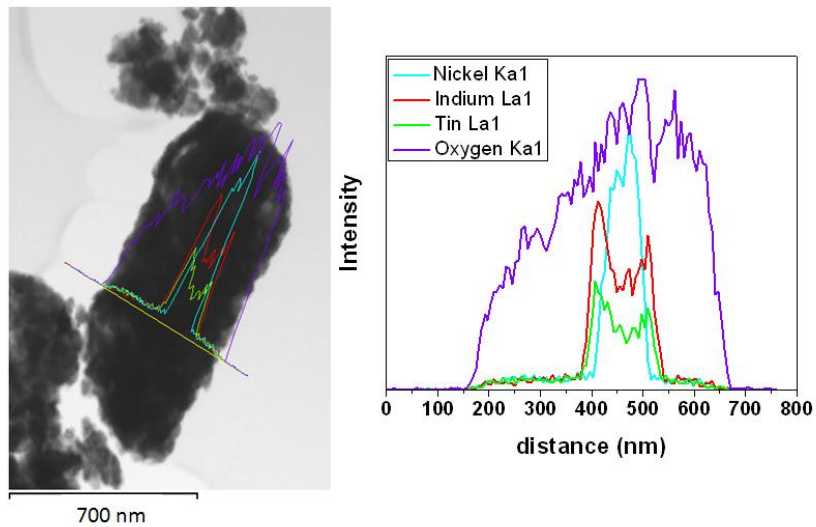


Figure 7.3. TEM image of a CuO/ITO/NiO nanowire with 15 min and 4 min sputter deposition of CuO and ITO and sintered at 450 °C for 1 hr.

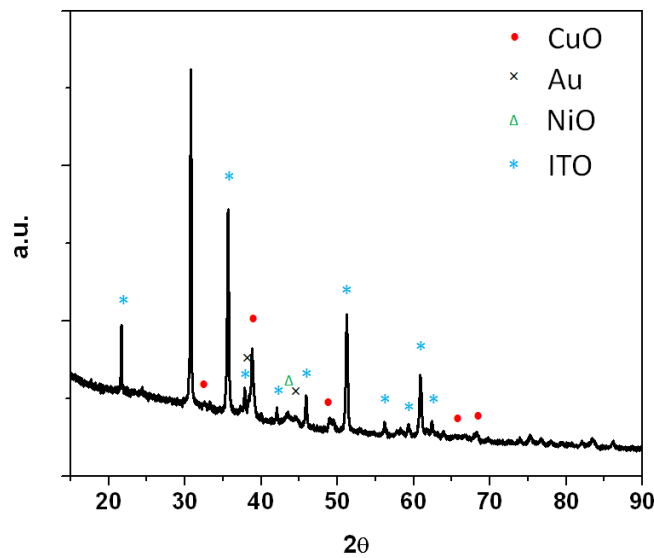


Figure 7.4. XRD for the film of CuO/ITO/NiO-TMV1cys/Au/ITO-glass.

The film morphology is well known to affect the efficiency of solar cell performance by varying the degree of light reflection (Zhu et al., 2010), charge transport distance (Kongkanand et al., 2007), total surface area (Chiang et al., 2012d), etc. Here, by varying the density of virus deposited on the substrate, the total surface area can be increased up to a factor of 13 (Royston et al., 2008). An increase in the density of surface assembled TMV1cys particles was observed between the range of  $10^{-4}$  and  $10^{-1}$  mg/mL. Based on the image analysis of the SEM micrographs as shown in Figure 7.5, the densities of the deposited TMV1cys particles were  $44 \pm 8$  per  $100 \mu\text{m}^2$  and  $228 \pm 25$  per  $100 \mu\text{m}^2$  for TMV1cys concentrations of  $10^{-4}$  and  $10^{-3}$  mg/mL, respectively, while the TMV1cys concentration of  $10^{-2}$  and  $10^{-1}$  gave densities of  $403 \pm 37$  per  $100 \mu\text{m}^2$  and  $610 \pm 56$  per  $100 \mu\text{m}^2$ , respectively. The average distance between virion particles was found to be 1200 nm and 500 nm for TMV1cys concentrations of  $10^{-4}$  and  $10^{-3}$  mg/mL, respectively. For more concentrated conditions, viruses tended to have different degrees of overlap between each other. In addition, the surface assembled virus rods have an average length of 600 nm which is about twice of a single virus length (Chen et al., 2011). This represents the end-to-end alignment of TMV1cys particles that occurs during the self assembling process in the solution (Shenton et al., 1999).

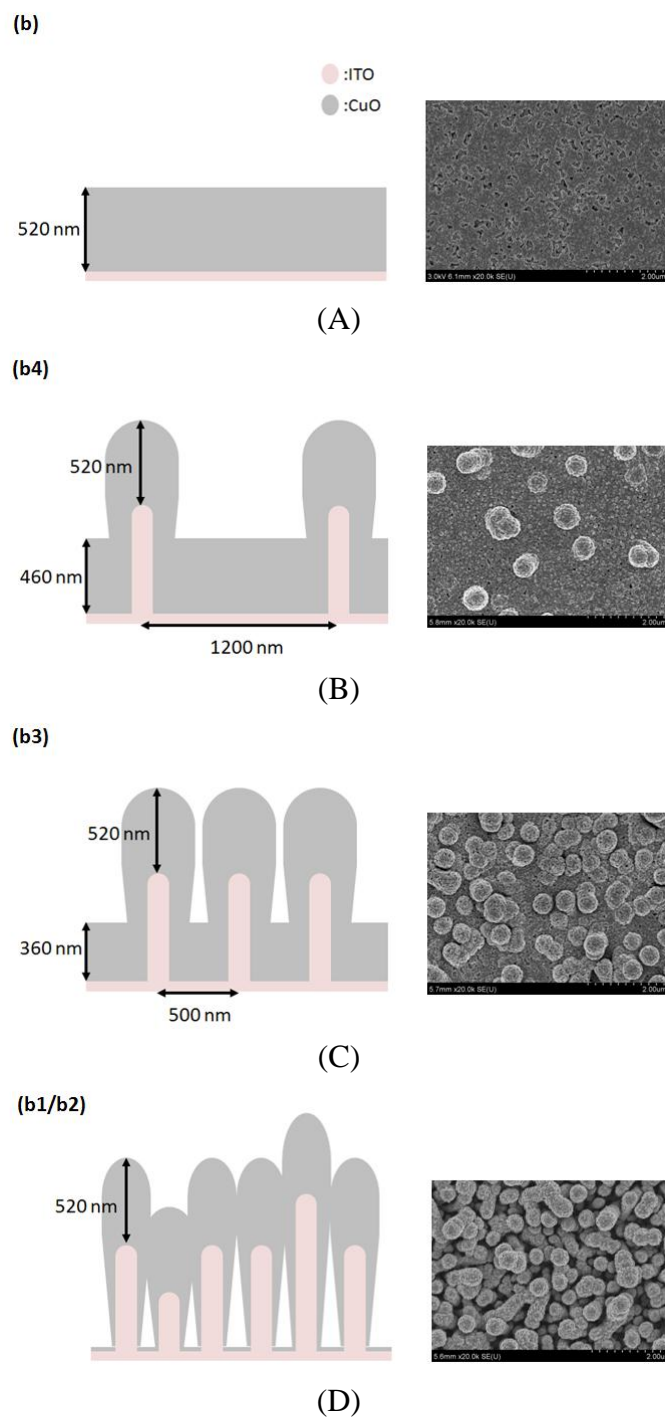


Figure 7.5. TMV concentration effects on the charge transport distance to the current collector and SEM micrographs for the surface morphology of 15 min CuO sputter deposition on different TMV1cys concentration prepared template current collector: (A) plain substrate, (B)  $10^{-4}$  mg/mL, (C)  $10^{-3}$  mg/mL, (D)  $10^{-2}$  mg/mL and  $10^{-1}$  mg/mL.



With sputtering different thicknesses of CuO, i.e. 5 min for 170 nm, 15 min for 520 nm, and 30 min for 1030 nm, on plain ITO glass substrates as standards, the PEC results of these CuO photocathodes are shown in Figure 7.6. An onset of photocurrent density at 0.1 V vs. Ag/AgCl was shown for all electrodes and the photocurrent density for all electrodes showed only a small different with applied bias voltage more positive than -0.2 V vs. Ag/AgCl. Once the bias voltage passed -0.2 V, the increase in photocurrent density was found for the sample with the virus patterned current collectors. This might be explained by higher concentration of charge carriers were generated and with the help of current collectors embedded, more charge carriers can survive without recombining before reaching the back contact.

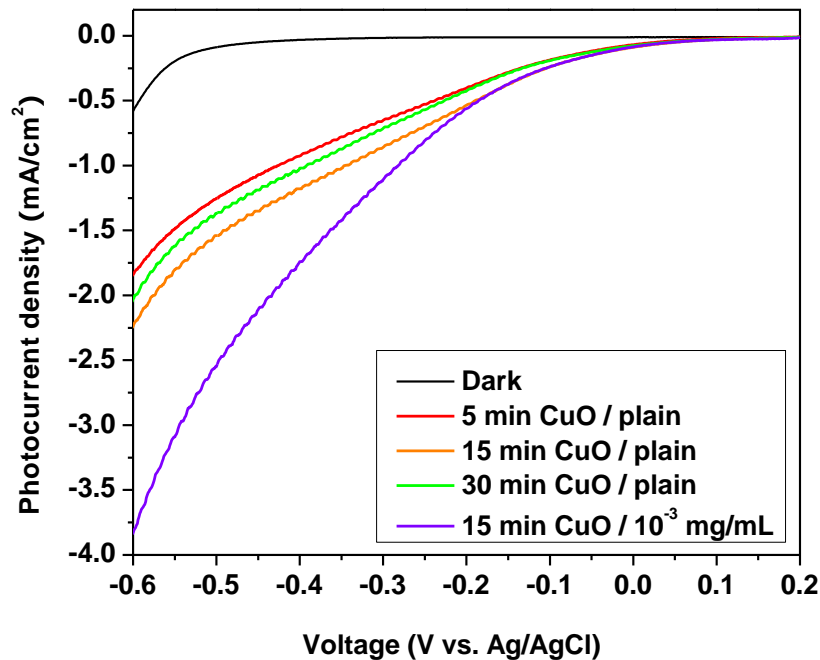


Figure 7.6. PEC performance of CuO deposited on plain substrates for the sputter deposition time of 5 min, 15min and 30 min along with a 15 min CuO deposition on TMV1cys patterned substrate.

A detailed comparison of photocurrent densities is tabulated in Table 7.1. The sample ID starts from “a” represents the CuO with thickness of 170 nm, “b” for 520 nm, and “c” for 1030 nm. The number in the sample ID represents the corresponding TMV1cys concentration, i.e. a2 means CuO thickness of 170 nm and TMV1cys concentration of  $10^{-2}$  mg/mL while a3 has concentration of  $10^{-3}$  mg/mL. Comparing the pure thickness effects of the CuO photocathodes, the best photocurrent density occurred at the CuO thickness of 520 nm and this half micron thickness was also the optimal for other CuO photocathodes in the PEC application (Chapter 4 and Chiang et al., 2011). It is not difficult to explain the existence of an optimal thickness for the film because the thicker the layer, the higher resistance of the film leading to an increase of the chance for charge carrier recombination, meanwhile, a thicker layer absorbs more incident light and thus leads to a higher solar irradiation usage. Introducing of the virus template current collector, the photocurrent densities increased for all conditions. This might be explained by the increased surface roughness and the decreased light reflectance which can be easily distinguished by eyes since the samples without virus deposition have mirror-like smooth and light reflecting surfaces as shown in Figure 7.7.

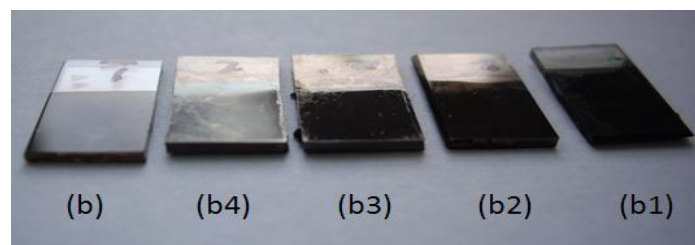


Figure 7.7. Appearance of samples with 520 nm CuO deposited on different substrates: (b) flat substrate with mirror like surface, (b4) virus patterned substrate with structure period more than 500 nm, (b3) to (b1) virus patterned substrate with patterned period less than 500 nm which suppress the light reflection.

Table 7.1. PEC results based on different CuO thickness and TMV concentrations.

Sample ID	CuO thickness (nm)	TMV1cys concentration <sup>#</sup> (mg/mL)	Photocurrent density* (mA/cm <sup>2</sup> )
(a)	170	0	1.50
(b)	520	0	1.80
(c)	1030	0	1.55
(a1)	170	10 <sup>-1</sup>	1.85
(a2)	170	10 <sup>-2</sup>	2.50
(b1)	520	10 <sup>-1</sup>	2.00
(b2)	520	10 <sup>-2</sup>	2.70
(b3)	520	10 <sup>-3</sup>	3.15
(b4)	520	10 <sup>-4</sup>	2.55
(c1)	1030	10 <sup>-1</sup>	2.05
(c2)	1030	10 <sup>-2</sup>	2.50
(c3)	1030	10 <sup>-3</sup>	2.75

<sup>#</sup> TMV concentration in solution

\* at bias voltage of -0.55 V vs. Ag/AgCl

Additionally, the introducing of virus template current collectors can help to decrease the charge transport distance and thus increase the photocurrent density. However, an interesting phenomenon was found in that the photocurrent density increased with decreasing the virus concentration except for the sample (b4), the lowest TMV1cys concentration tested in this experiment. For the detailed illustration of the phenomenon, the cross section cartoon for the samples with dimension to scale and the bird eye view of the samples by SEM are given in Figure 7.5. In the figure, CuO was sputtered on the substrates with various concentration current collectors, as noted on the top-left corner,

for 15 min (520 nm on flat surface and on top of current collector). In Figure 7.5(A), sample (b) with a plain ITO substrate and 520 nm CuO showed a 1.8 mA/cm<sup>2</sup> photocurrent density at bias voltage of -0.55 V vs. Ag/AgCl. For sample (b4), as the TMV1cys concentration increased to 10<sup>-4</sup> mg/mL which corresponding to the average distance between virus template current collectors of 1200 nm, the lower of the average CuO thickness to 460 nm on the no virus area was observed. This might be due to the vertical current collectors serving as geometrical obstacles during the sputter deposition. Comparing these two samples, one can see that the shorter charge carrier transport distance was demonstrated because the three dimensional current collector provided more than one direction for charge carrier to be collected. The photon excited charge carriers on the top surface of the film do not have to go through all 520 nm to be safely separated as in sample (b); on contrary, the excited charge carriers can find the shorter distance to either the back ITO contact or the three dimensional ITO current collector and thus increase the possible life time of the charge carriers. Also, with the introduction of the template, more surface area was provided.

As the TMV1cys concentration further increased to 10<sup>-3</sup> mg/mL, sample (b3), which corresponding to the average distance between virus template current collectors of 500 nm, the highest photocurrent density, 3.15 mA/cm<sup>2</sup> at bias voltage of -0.55 V vs. Ag/AgCl (shown in Figure 7.6), was found among all the samples in this study. Similarly, due to the geometrical obstacle, the thickness of CuO at the area without virus deposition decreased to 360 nm. The highest photocurrent density found in this sample might be because the charge carrier transport distance was shortened to less than or equal to 500 nm which was shown to be the optimal thickness for the intrinsic CuO samples (Chapter

4 and Chiang et al., 2011) at the same time it also had an enough thickness for absorbing solar energy throughout the sample. However, as the TMV1cys concentration further increased to  $10^{-2}$  mg/mL and  $10^{-1}$  mg/mL, sample (b2) and (b1), the highly concentrated virus templates were no longer available for the uniform deposition of the CuO by sputtering. Only a small amount of CuO was deposited at the bottom of the film, i.e. right on the back contact ITO, and most of the CuO was deposited on the top of the current collectors leaving lots of empty space at the bottom of the samples. Because of this situation, the effect on shortening the charge carrier transport distance was not as apparent comparing to the plain substrate. As in Table 7.1, the photocurrent densities for sample (b1) only showed a 10% increase comparing to the plain substrate. The difference between sample (b1) and (b) can be further explained by the slightly increased surface area and roughness of the surface of (b1) since the TMV1cys can self-align into different lengths, i.e. 600 nm for two viruses and 900 nm for three viruses. This also gave a shorter distance for charge carrier transport as shown in Figure 7.5(D).

Additionally, when light hits the interface between materials with different refractive indices, a significant portion of it is reflected. With the nanorod surface structure, a graded-refractive index layer was formed and light experienced a gradual change and reduced the reflection. A comparison of the effect of surface structure of sample b, b1, b2, b3 and b4 on reflectance is shown in Figure 7.8. As the TMV1cys concentration increased to  $10^{-3}$  mg/mL (b3), the light reflectance decreased from 13% to 3% at the wavelength range of 200-600 nm. When the concentration was further increased, there was no apparent different in reflectance.

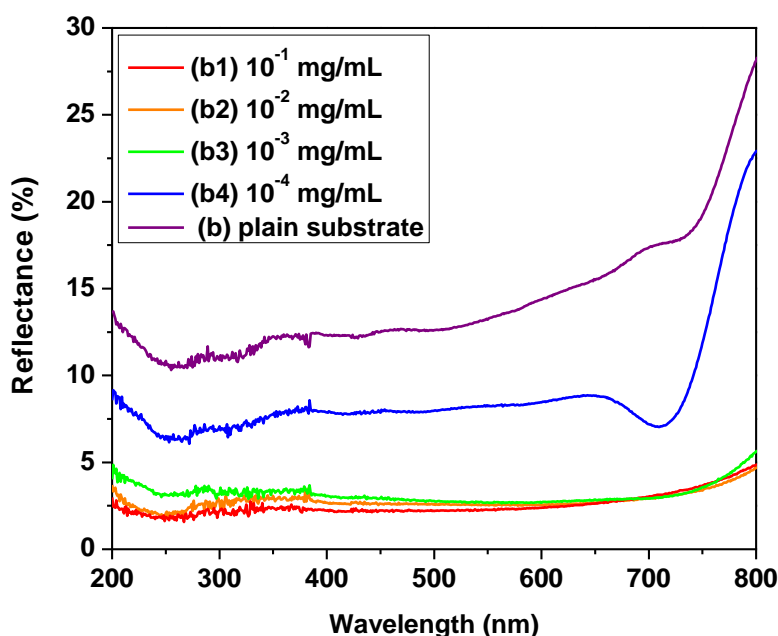


Figure 7.8. Reflectance of samples with 15 min CuO deposited on different TMV1cys concentration substrates.

Based on the virus templates with concentration of  $10^{-2}$  mg/mL, the CuO was sputtered at different thicknesses, i.e. (a2) 5 min for 170 nm, (b2) 15 min for 520 nm, and (c2) 30 min for 1030 nm, which gave very different morphologies of the films as shown in Figure 9. The average outer diameters of each of the CuO rods increase from 220 nm to 450 nm and 710 nm and the detailed construction of each CuO rods is illustrated in Figure 10. As seen in Figure 7.9 and Figure 7.10, a uniform rod like shape was found for sample with 5 min CuO deposition but as the sputtering time increased, thicker deposition on the head was found due to the geometrical obstacle increasing the difficulty in CuO deposition down to the bottom area. Based on these samples, the photocurrent density increased from  $2.5 \text{ mA/cm}^2$  for (a2) to  $2.7 \text{ mA/cm}^2$  for (b2) but it decreased back to  $2.5 \text{ mA/cm}^2$

while increasing the CuO thickness to 1030 nm for (c2) at bias voltage of -0.55 V vs. Ag/AgCl as shown in Table 7.1. This further confirmed the importance of the CuO film thickness to the photocurrent density.

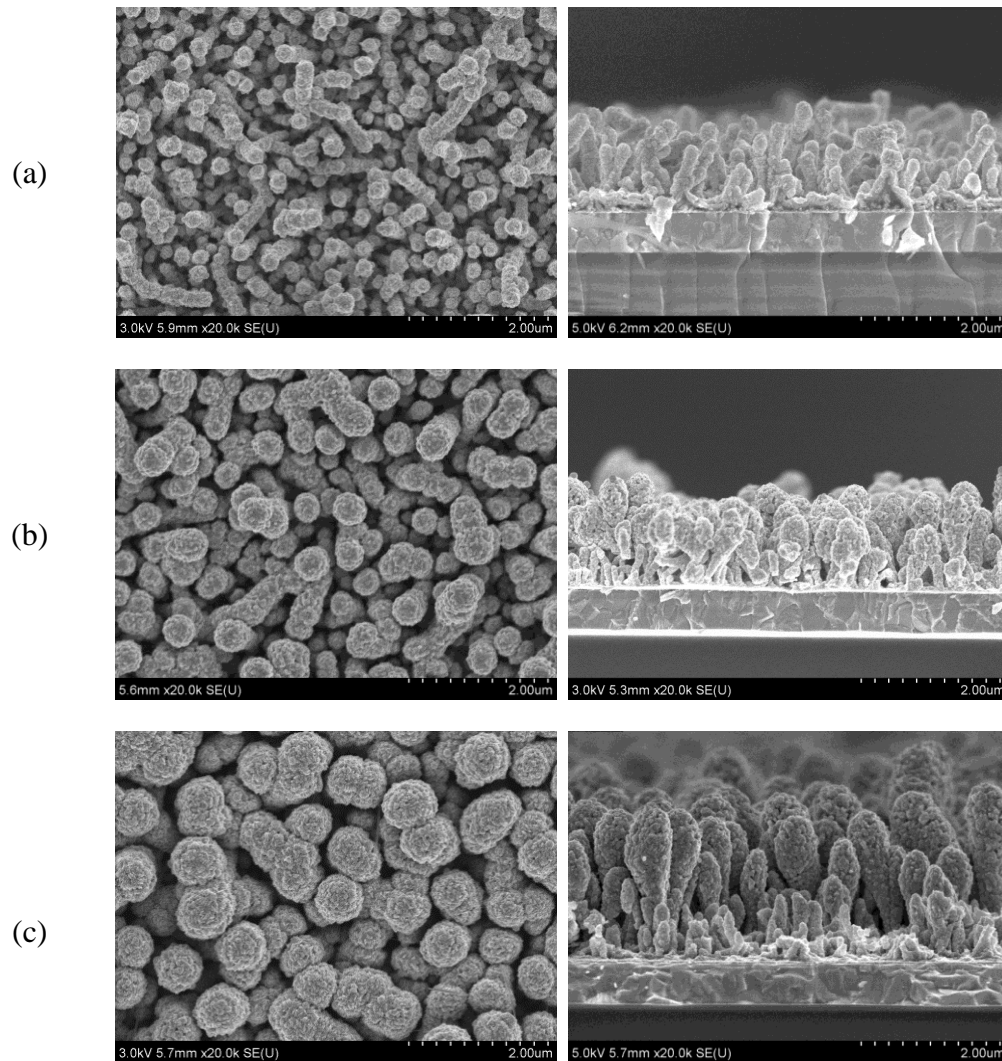


Figure 7.9. SEM image of virus solution at  $10^{-2}$  mg/mL and sputtering coated with 4 min ITO and various deposition time for CuO: (a) 5 min (b) 15 min and (c) 30 min.

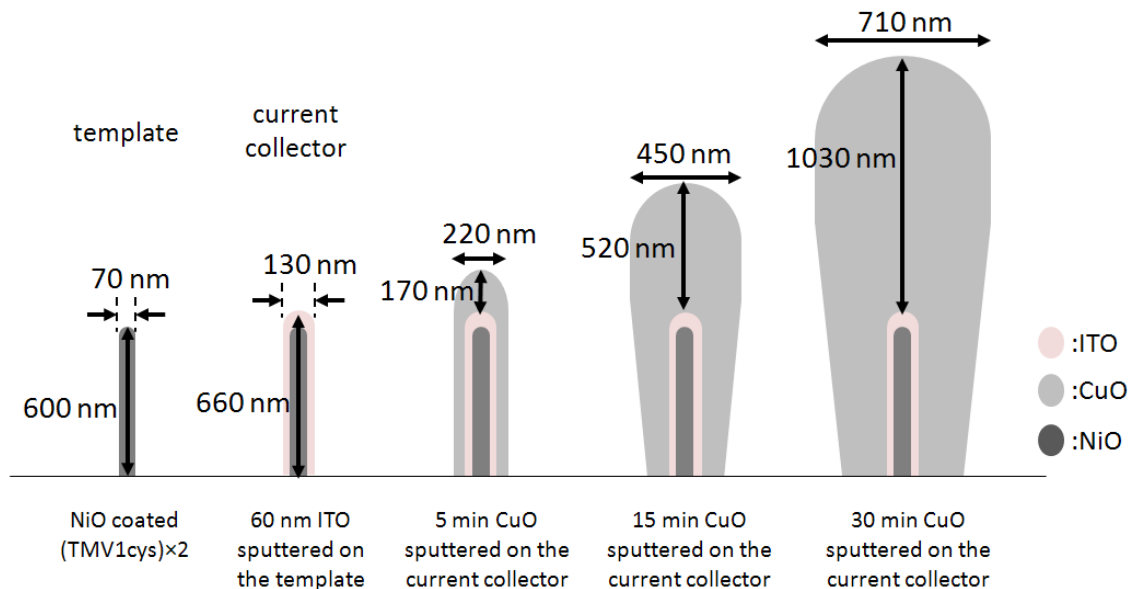


Figure 7.10. Illustration of the detail construction of virus template, current collector and each CuO rods at different CuO deposition thickness.

The highly increased photocurrent density for the three dimensional virus patterned current collectors was reinforced when compared to other CuO photocathode systems in the literature (Nakaoka et al., 2004; Chauhan et al., 2006; Chapter 4 and Chiang et al., 2011; Chapter 5 and Chiang et al., 2012c; Chapter 6 and Chiang et al., 2012b; Chiang et al., 2012d; Koffyberg and Benko, 1982) as tabulated in Table 7.2. The highest photocurrent density was found to be  $3.15 \text{ mA/cm}^2$  in this study under 1 sun irradiation (AM1.5G,  $1000 \text{ W/m}^2$ ). It is two to three times higher than our previous nanoparticle systems (Chapter 4 and Chiang et al., 2011; Chapter 5 and Chiang et al., 2012c; Chapter 6 and Chiang et al., 2012b; Chiang et al., 2012d) and about an order of magnitude higher than other study (Koffyberg and Benko, 1982) where a much higher incident light intensity,  $8100 \text{ W/m}^2$ , was applied. This work demonstrates the effectiveness of



composite nanosized three dimensional current collectors which their periodicity also functioned as anti-reflection structure in enhancing photoelectrochemical cell efficiency.

Table 7.2. Photocurrent density of CuO photocathodes in different systems.

System	Light source	Incident power density (W/m <sup>2</sup> )	Bias voltage (V)	Photocurrent density (mA/cm <sup>2</sup> )	Reference
CuO	150W Solar simulator	1000	-0.55 vs. Ag/AgCl	3.15	This study
CuO	500W Xenon lamp		-0.2 vs. Ag/AgCl	0.08	Nakaoka et al., 2004
CuO	150W Xenon Arc lamp		-0.5 vs. SCE	2.2	Chauhan et al., 2006
CuO	150W Solar simulator	1000	-0.55 vs. Ag/AgCl	1.20	Chiang et al., 2011
CuO	150W Solar simulator	1000	-0.55 vs. Ag/AgCl	1.20	Chiang et al., 2012b
CuO	150W Solar simulator	1000	-0.55 vs. Ag/AgCl	1.58	Chiang et al., 2012d
2at% Li-CuO	150W Xenon Arc lamp	8100	-0.4 vs. SCE	0.44	Koffyberg and Benko,1982
2at% Li-CuO	150W Solar simulator	1000	-0.55 vs. Ag/AgCl	1.69	Chiang et al., 2012c

## 7.5. CONCLUSIONS

Three dimensional patterned current collectors were successfully prepared by self-assembling of TMV1cys on gold coated substrate and ITO depositing by sputtering method. This greatly reduces the charge carrier transport distance and along with this advantage, the surface structure with period about 500 nm, i.e. TMV1cys concentration at

$10^{-3}$  mg/mL, was demonstrated to suppress the light reflection which leads to a higher efficiency in utilizing the incident photons. Sputter deposition of CuO with thickness of 520 nm on the patterned current collectors demonstrates the highest photocurrent density, i.e.  $3.15 \text{ mA/cm}^2$ , among the literature because of the nanosized CuO which decreases the recombination in the particle, the three dimensional current collectors, which shortens charge carrier transport distance, and patterned surface structure, which lowers light reflection.

# Chapter 8

## Conclusions and Future Work

### 8.1. CONCLUSIONS

The photoelectrochemical water splitting efficiency of CuO photocathodes has been successfully improved by the four main approaches proposed in this study: (1) decrease particle size to decrease the electron-hole recombination in the particles, (2) increase surface area to increase the active sites and decrease the distance for electron to react with water (3) increase conductivity to decrease the resistance of the electrode, and (4) shorten charge carrier transport distance to decrease the probability of recombination of charge carriers.

In the first part, flame spray pyrolysis (Chapter 3) and wet chemical method of CuO particle preparation (Chapter 6) are demonstrated able to decrease the particle size down to the nanoscale. For the FSP approach, CuO particle size can be manipulated from  $7\pm 2$  to  $20\pm 11$  nm by varying the precursor concentration from 0.5% to 35% w/w without changing the primary particle aspect ratio (1.2-1.3). Also, introduction of liquid nitrogen is shown to decrease the crystalline size by quenching the particles and thus limit atoms become oriented. Furthermore, primary particles tended to grow larger when the particle residence time in the high temperature was approximately 8 times longer due to the lower gas flow rate in set B. A simulation of particle growth based on collision/sintering theory gave a reasonable estimation of the particle size given the time-temperature history.

Compared to the near spherical nano CuO particles produced by FSP method, the CuO particles produced by the wet chemical method have relatively high aspect ratios, i.e. from 3.1 to 9.7 based on the reaction temperature and time. Particles prepared with solution reacted at 25 °C tended to have a higher aspect ratio ( $9.7 \pm 4.9$ ) rod-like shapes with dimension of  $(0.2 \mu\text{m to } 2 \mu\text{m}) \times (50 \text{ nm})$ . As the temperature increased to 60 °C, the aspect ratio decreased to  $3.1 \pm 1.2$  and the morphology was spindle-like. Upon further increase in the temperature to 95 °C, needle-like shaped particles were observed and the particle length decreased significantly to tens of nanometers. The PEC performance based on these CuO nanoparticle based photocathodes reached 0.91% solar to hydrogen conversion efficiency (Chapter 4 and Chapter 6) which is higher than commercially available CuO nanoparticles from Sigma-Aldrich, which do not have as uniform of a particle size distribution.

In the second approach, highly porous films were prepared by spin coating of the CuO along with some impurities from the incomplete reaction during the particle preparation processes such as the wet chemical process (Chapter 6). The impurity,  $\text{Cu}_2(\text{NO}_3)(\text{OH})_3$ , along with CuO nanoparticles were spin coated on the substrate and sintered at higher temperature to transform the impurities into CuO. The morphology changes lead to porous structure of the films and higher surface area. Comparing the films with same thickness, i.e. 1340 nm, made by FSP (Chapter 4) and wet chemical synthesis (Chapter 6), a 30% increase in efficiency at -0.55 V vs. Ag/AgCl as found in porous film prepared by the wet chemical process.

The next target was to increase the conductivity of the film which can decrease the resistance of the charge carrier transport and thus increase the efficiency (Chapter 5). Li

was introduced to the CuO particles by FSP method and the carrier density was estimated to be  $4.2 \times 10^{21}$  which is about an order higher than most of the intrinsic samples. The increase in the carrier density also contributed to about a two orders of magnitude increase in the electrical conductivity. Based on the 2 at% Li doped CuO sample with thickness of 1.7  $\mu\text{m}$ , the photoelectrochemical efficiency is found to be 1.3% which is the highest among all the CuO samples.

The last idea of shortening the charge transport distance by a current collector was demonstrated in Chapter 7. The TMV1cys virus embedded 3D current collectors have demonstrated that shortening the transport distance allows for the photon-excited charge carriers to be safely separated. The CuO film deposited by sputtering technique with thickness of half micron meter showed the optimal for efficient solar irradiation absorption and the effective charge carrier separation. The concentration of  $10^{-3}$  mg TMV1cys/mL solution gave a distance between two virus particles of a half micron, when deposited on the substrate. Such a periodical structure serves as an anti-reflecting surface which decreases the light bounce off from the surface and increases the efficiency. The best photocurrent density among these samples was found to be  $3.15 \text{ mA/cm}^2$  corresponding to a CuO thickness of 520 nm and a virus concentration at  $10^{-3}$  mg/mL.

## **8.2. FUTURE WORK**

### **8.2.1. CuO Stability Improvement**

Although CuO has been proven able to absorb sunlight efficiently and has suitable band edges, the major problem is the stability upon illumination in the electrolyte. Since CuO is not thermodynamically stable upon illumination in the electrolyte, the kinetic stabilization of semiconductor-electrolyte interface approach would be the option to solve the issue. The kinetic stabilization approach is that the photoactivated charge carriers are predominately channeled into the desired pathway, i.e. water splitting, rather than photocorrosion of the semiconductor. It can be accomplished by coating a corrodible semiconductor with a thin protective layer of a nearly non-corrodible material such as TiO<sub>2</sub> or Pt (Tsubomura and Nakato, 1987). It also can be achieved by introducing surface states or modifying the semiconductor surface with a thin polymer layer doped with catalysts which help to stabilize the photoelectrodes (Frank, 1983). Such strategies for p-type CuO photocathodes are illustrated in Figure 8.1.

Two recent studies of the stabilization of Cu<sub>2</sub>O photocathodes based on the strategy of coating a relatively stable semiconductor (along with Pt catalyst) have reported results demonstrating improved stability (Paracchino et al., 2011; Zhang and Wang, 2012). After 20 min of water splitting reaction, about 80% retention of the activity of the photocathode is shown in both studies. Based on this concept, a small band gap CuO photocathode might be able to work stably for PEC water splitting if any of these electrode stabilization strategies are applied.

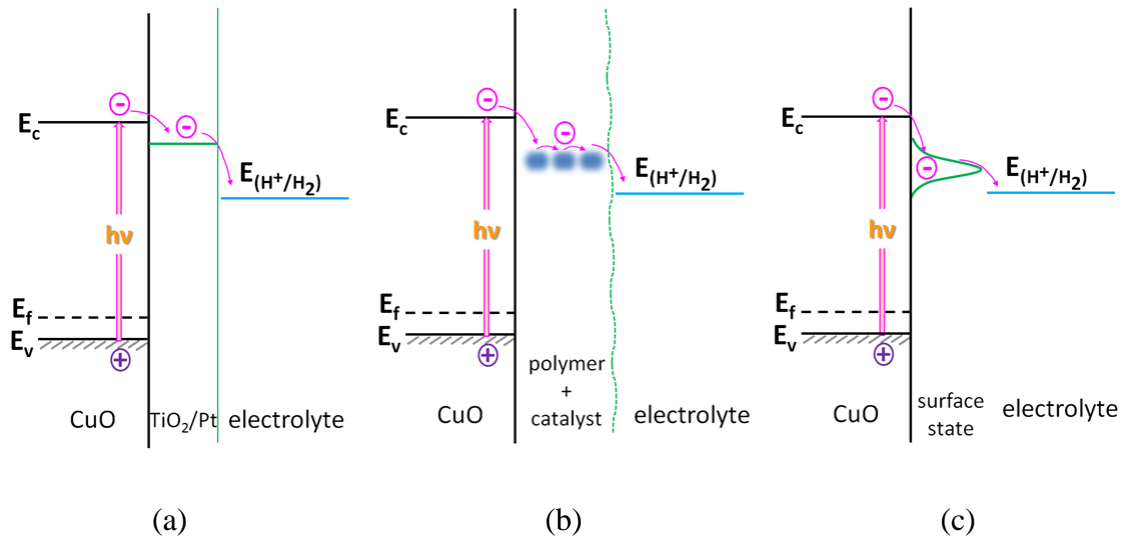


Figure 8.1. Different strategies for stabilization of semiconductor electrolyte interface: (a) surface layer of noble metal or stable semiconductor, (b) stabilization with polymer layer along with electron transfer catalysts, (c) stabilization through catalytic surface states.

### 8.2.2. Possible Nanoarchitectures for PEC Cells

In this dissertation, polycrystalline structures with nanosized particle made films and 3D current collectors embedded in the film for photocathodes have been shown to increase the efficiency of PEC cells. More nanostructures, such as single-crystal nanowire arrays, can be applied to increase the efficiency by increasing the mobility of charge carriers as shown in Figure 8.2 (Baxter and Aydil, 2005; Baxter et al., 2006; Law et al., 2005; Faglia et al., 2009). The mobility of charge carriers in a single-crystal nanowire is approximately 100 times higher than in a polycrystalline network (Faglia et al., 2009). By applying the single-crystal nanowire array, the drawback in the polycrystalline system, i.e. the electrons must pass thousands of grain boundaries before reaching the back contact, can be eliminated. For copper oxide nanowire array preparation, many methods such as

heating the copper foil in the air (Chen et al., 2008), sol-gel method (2007), and thermal oxidation (Cheng and Chen, 2012) can be used. The photocurrent density is expected to be higher with the nanowire structure.

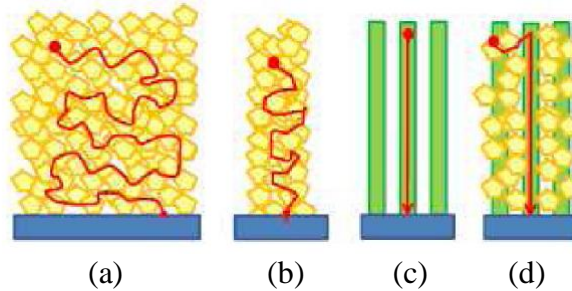


Figure 8.2. Four different structures for photoelectrochemical cells: (a) Polycrystalline network, (b) polycrystalline nanotube, (c) single-crystal nanowire array, and (d) network of single-crystal nanowires and dispersed nanoparticles. (Faglia et al., 2009)

### 8.2.3. Effects of Particle Size/Surface Area/Porosity on PEC Cells

In order to further distinguish the effects of particle size, surface area and porosity separately on a PEC cell, we assumed that the uniform photoactive particles are available and with radius of  $r$ . The films can be prepared by spin coating to reach different porosity ( $P$ ) by varying the concentration of particle suspension as describe in previous chapters. The substrate has a constant surface ( $A_{sub}$ ) and the film is prepared to be a constant height ( $h$ ). In the film, the number of particles is  $n$ . Upon heat treatment, the particles are sintered and only a fraction of the original surface area ( $C(T)$ ) remains, for example,  $C=0.8$  when 20% of their surface area is lost after particles sintered together. The illustration of  $C$  is shown in Figure 8.3.



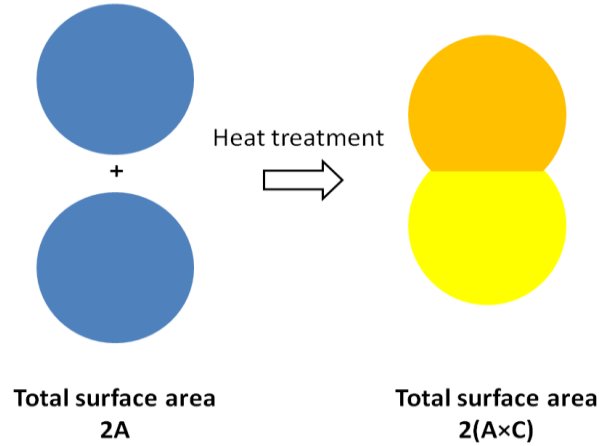


Figure 8.3. The illustration of  $C$ .

Constant porosity

Based on a given suspension solution concentration and a given spin coating condition, the equations can be described as follows,

$$S = 4\pi r^2 n C \quad (8.1)$$

$$P = 1 - \frac{\frac{4}{3}\pi r^3 n}{A_{sub} h} \quad (8.2)$$

where  $S$  is the total surface area of the film,  $r$  is particle radius,  $n$  is the number of particles in the film. Before and after heat treatment, the mass of photoactive material should remain constant, thus  $P$  is constant before and after sintering. Eq 8.1 can be rearranged to

$$\begin{aligned} S &= 4\pi r(T)^2 n(T) C(T) \\ &= \left( \frac{4}{3}\pi r(T)^3 n(T) \right) \frac{3}{r(T)} C(T) \\ &\sim \frac{C(T)}{r(T)} \end{aligned} \quad (8.3)$$

When sintering temperature is increased,  $C(T)$  decreases and  $r(T)$  increases, thus  $S(T)$  decreases.

### Surface Area Effect

By changing the suspension concentration while keep  $A_{sub}$  and  $h$  constants,  $S$  is proportional to  $n$ . As described above, the porosity keeps constant before and after sintering, and at a given sintering temperature,  $r$  and  $C$  are both constant. As a result,  $S$  is proportional to  $n$  which is proportional to the mass of coated particles. If the mass is known and the PEC result as a function of suspension concentration is determined by experiment, the effect of surface area on PEC can be found.

Note: however, the number of particles is different, thus the total light absorption might not be the same.

Photoactive particles with different particle sizes ( $r_1, r_2, r_3$ ) are spin coated on the substrates at constant thickness ( $h$ ). By varying the suspension concentration to change  $n$  and let  $r^3n$  is a constant. Then the porosity for different films is the same. After heat treatment, the porosity remains constant and  $S$  is proportional to  $1/r$ . Thus the pure surface area effect on PEC can be found. This analysis assumes  $C$  is the same for different particle size samples during heat treatment.

### Particle Size Effect

Rearranging Eq 8.1 and Eq 8.2, we can obtain Eq 8.4

$$1 - P = \frac{r S}{3 \bar{C} A_{sub} h} \quad (8.4)$$

Since we assumed  $A_{sub}$ , and  $h$  are constants, then

$$(1 - P) \sim \frac{rS}{C} \quad (8.5)$$

Since we know the effect on surface area based on previous discussion, and  $P$  is constant before and after heat treatment, thus at a given sintering temperature ( $C$  is assumed to be the same for samples), the effect of  $r$  on PEC can be distinguished.

# Appendix 1

## Film Porosity/Total Surface Area Estimation

Coverage percentage refers to the amount of space occupied by copper oxide particles in the film of certain volume. It essentially resembles  $(1 - \text{porosity})$ . To find the coverage percentage of a given film, follow the procedure outlined below along with Figure A.1. In Figure A.1, there are “n” number of red, horizontal lines that cross through a cross-sectional image of the film with a known length “a”. Circles represent individual copper oxide particles. The dashed lines represent empty space, whereas solid, bolded lines represent the length occupied by the particles. For respective red lines, calculate the sum of the length inside the particles, i.e. for  $n=1$ , calculate the sum of  $b(1,1)$ ,  $b(1,2)$ , and  $b(1,3)$ . Then, divide that sum by the horizontal length “a”. Repeat the same calculations for each subsequent red line. By finding the average of all those calculations, the estimated value for coverage percentage can be achieved. In theory, infinite number of lines would provide the exact value of coverage percentage.

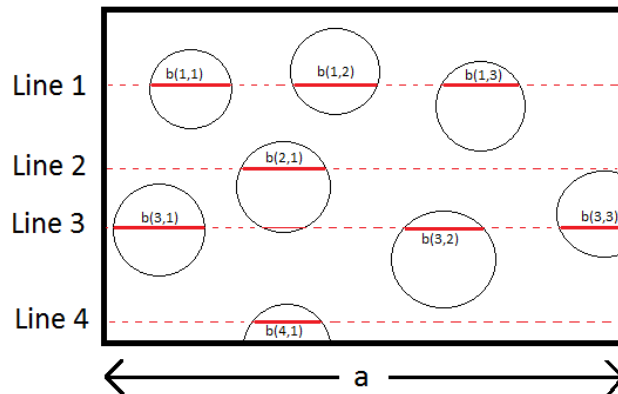


Figure A.1. Cross-section view of the film

In theory, infinite number of cross-sections in the same direction is required to find the coverage percentage in a 3D film. Because it is infeasible to obtain so many cross-sectional images, few assumptions must be made to obtain a 3D analysis of coverage percentage. Due to the uniform nature of spin-coating, particles are dispersed onto the flat surface of the film uniformly. Copper oxide particles, however, might not be placed similarly from one layer of spin-coating to another. By using the side-view cross-sectional images to undergo the coverage percentage calculations, it is possible to take both factors into account. Because one side-view cross-sectional image is similar to another from the same axis, it is possible to extend the coverage percentage at the 2D level to the 3D level.

Considering that the average diameter of CuO particle is known through SEM images, the number of particles in a perfectly compact three dimensional film can be found. To do so, divide the diameter of the particle from the length, width, and height of the film; then, multiply the three values together to find the total number of particles in a perfectly compact film. The coverage percentage was required because it is unreasonable to assume that the particles will occupy the film in a perfectly compact manner. Therefore, the total number of particles in a perfectly compact film is multiplied by the coverage percentage to find the estimated number of particles in the film. By assuming that the particles are shaped spherically, the surface area of individual copper oxide particles can be found using the equation:  $SA = 4\pi r^2$ . The individual surface area of the particle can then be multiplied by the estimated number of particles to find the total surface area of the film.

**Coverage Percentage:** Amount of space occupied by the particles in the film

- n : Number of horizontal lines that cross through the length of the film  
m : Number of separate solid lines for each horizontal line  
a : Length of the film  
b(n,m) : Length of the solid line inside the particle

1. Solve for  $c_i$  for each horizontal line using

$$c_i = \frac{\sum b(n_i, m_i)}{a} \quad (A.1)$$

i.e. for Line 1,  $c_1 = [(b(1,1) + b(1,2) + b(1,3)]/a$

2. Average the fractional values from each horizontal line using

$$d_n = \frac{(c_1 + c_2 + c_3 + c_4 + \dots + c_n)}{n} \quad (A.2)$$

i.e. for  $n = 5$ ,  $d_5 = (c_1 + c_2 + c_3 + c_4 + c_5)/5$

### **Total Surface Area of Film:**

Given: a film of dimension  $l \times w \times h$  and spherically shaped particles of diameter  $d$

1. Calculate the total # of particles in a perfectly compact film using

$$N_{\text{perfect}} = \frac{l}{d} \times \frac{w}{d} \times \frac{h}{d} \quad (A.3)$$

2. Calculate the estimated # of particles in the experimental film using

$$N_{\text{exp}} = N_{\text{perfect}} \times \text{coverage percentage} \quad (A.4)$$

3. Calculate the surface area of individual particles using

$$SA = 4\pi r^2 \quad (A.5)$$

4. Calculate the total surface area of film using Eq. (A.6)

$$SA_{\text{film}} = N_{\text{exp}} \times SA \quad (A.6)$$

## REFERENCES

- Adamczyk Z, Nowotny J. Effect of segregation on near-surface and bulk transport phenomena in ionic crystals. *J Phys Chem Solids*. 1986;47:11–24.
- Alexander L, Klug HP. Determination of crystallite size with the X-Ray spectrometer. *J Appl Phys* 1920; 21: 137-142.
- Anpo M, Takeuchi M. The design and development of highly reactive titanium oxide photocatalysts operating under visible light irradiation. *J Catal*. 2003;216;505-16.
- Arana-Chavez D, Toumayan E, Lora F, McCaslin C, Adomaitis RA. Modeling the transport and reaction mechanisms of copper oxide CVD. *Chem Vapor Depos* 2010; 16: 336-345.
- Ashokkumar M. An overview on semiconductor particulate systems for photoproduction of hydrogen. *Int J Hydrogen Energ*. 1998;23;427-38.
- Bak T, Nowotny J, Rekas M, Sorrell CC. Photo-electrochemical hydrogen generation from water using solar energy. Materials-related aspects. *Int J Hydrogen Energ* 2002; 27: 991-1022.
- Bak T, Nowotny J, Sorrell CC. In: Nowotny J, Sorrell CC, editors. *Electrical properties of oxide materials*. Enfield, NH: Trans Tech Publ; 1997, p. 1.
- Barrerca D, Fornasiero P, Gasparotto A, Gombac V, Maccato C, Montini T, Tondello E. The potential of supported Cu<sub>2</sub>O and CuO nanosystems in photocatalytic H<sub>2</sub> production. *ChemSusChem* 2009;2:230-33.
- Barborini E, Conti A, Kholmanov I, Piseri P, Podestá A, Milani P, Sancrotti M. Nanostructured TiO<sub>2</sub> films with 2 eV optical gaps. *Adv Mater*. 2005;17:1842-6.
- Baxter JB, Aydil ES, Nanowire-based dye-sensitized solar cells, *Appl. Phys. Lett*. 2005; 86: 053114.

- Baxter JB, Walker AM, van Ommering K, Aydil ES, Synthesis and characterization of ZnO nanowires and their integration into dye-sensitized solar cells, *Nanotechnol.* 2006; 17: S304–S312.
- Belova IV, Murch GE. Diffusion in Nanocrystalline Materials. *J Phys Chem Solids* 2003; 64: 873–878.
- Bequerel E. Recherches sur les effets de la radiation chimique de la lumière solaire, au moyen des courants électriques. *C.R. Acad Sci* 1839; 9; 145.
- Bockris JOM, Khan SUM. *Surface Electrochemistry, A molecular level approach.* New York: Springer; 1993.
- Borghain K, Singh JB, Rao MVR, Shripathi T, Mahamuni S. Quantum size effects in CuO nanoparticles. *Phys Rev B* 2000; 61:11093-11096.
- Borzi RA, Stewart SJ, Punte G, Mercader RC, Curutchet GA, Zysler RD, Tovar M. Effect of ion doping on CuO magnetism. *J. Appl. Phys.* 2000; 87:4870-2.
- Bradley D, Matthews KJ. Measurement of High Gas Temperatures with Fine Wire Thermocouples. *J Mech Eng Sci* 1968; 10: 299-305.
- Bui NN, Kang SZ, Li X, Jin M. Effect of Si doping on the photocatalytic activity and photoelectrochemical property of TiO<sub>2</sub> nanoparticles. *Catal Commun.* 2011;13;14-7.
- Carnes CL, Stipp J, Klabunde KJ. Synthesis, characterization, and adsorption studies of nanocrystalline copper oxide and nickel oxide. *Langmuir* 2002; 18:1352-1359.
- Carnes CL, Klabunde KJ. The catalytic methanol synthesis over nanoparticle metal oxide catalysts. *J Mol Catal A-Chem* 2003; 194:227-236.
- Camenzind A, Caseri WR, Pratsinis SE. Flame-made nanoparticles for nanocomposites. *Nano Today* 2010; 5:48-65.



- Camenzind A, Strobel R, Pratsinis SE. Cubic or monoclinic  $\text{Y}_2\text{O}_3\text{-Eu}^{3+}$  nanoparticles by one step flame spray pyrolysis. *Chem Phys Lett* 2005; 415:193-197.
- Carey JH, Oliver BG. Intensity effects in the electrochemical photolysis of water at the  $\text{TiO}_2$  electrode. *Nature*. 1976;259:554-56.
- Chandra Babu KS, Singh D, Srivastava ON. Preliminary investigations on the mixed oxide material  $\text{TiO}_2 \text{In}_2\text{O}_3$  with regard to photoelectrolytic hydrogen production. *Int J Hydrogen Energy*. 1991;16:387-91.
- Chandra S. Photoelectrochemical solar cells. New York: Gordon and Breach, 1985. p. 98.
- Chang MH, Liu HS, Tai CT. Preparation of copper oxide nanoparticles and its application in nanofluid. *Powder Tech* 2011; 207:378-386.
- Chang H, Lenggoro W, Okuyama K, Jang HD. Flame spray pyrolysis for preparing red-light-emitting, submicron-sized luminescent strontium titanate particles. *Jpn J Appl Phys* 2006; 45:967-973.
- Chang H, Lenggoro IW, Okuyama K, Kim TO. Continuous single-step fabrication of nonaggregated, size-controlled and cubic nanocrystalline  $\text{Y}_2\text{O}_3\text{:Eu}^{3+}$  phosphors using flame spray pyrolysis. *Jpn J Appl Phys* 2004; 1 43:3535-3539.
- Chauhan D, Satsangi VR, Dass S, Shrivastav R. Preparation and characterization of nanostructured CuO thin films for photoelectrochemical splitting of water. *B Mater Sci* 2006; 29:709-16.
- Chen CY, Wang M, Li JY, Pootrakulchote N, Alibabaei L, Ngoc-le CH, Decoppet JD, Tsai JH, Gratzel C, Wu CG, Zakeeruddin SM, Gratzel M. Highly efficient light-harvesting ruthenium sensitizer for thin-film dye-sensitized solar cells. *ACS Nano*. 2009;3;3103-9.
- Chen J, Deng SZ, Xu NS, Zhang WX, Wen XG, Yang S. Temperature dependence of field emission from cupric oxide nanobelt films. *Appl Phys Lett* 2003; 83:746-748.

- Chen D, Gao YF, Wang G, Zhang H, Lu W, Li JH. Surface tailoring for controlled photoelectrochemical properties: Effect of patterned TiO<sub>2</sub> microarrays. *J Phys Chem C* 2007; 111:13163-69.
- Chen X, Gerasopoulos K, Guo J, Brown A, Wang C, Ghossi R, Culver JN. A patterned 3D silicon anode fabricated by electrodeposition on a virus-structured current collector. *Adv Funct Mater.* 2011;21:380-7.
- Chen X, Gerasopoulos K, Guo J, Brown A, Wang C, Ghodssi R, Culver JN. Virus-enabled silicon anode for lithium-ion batteries. *ACS Nano.* 2010;4:5366-72.
- Chiang CY, Aroh K, Franson N, Satsangi VR, Dass S, Ehrman SH. Copper oxide nanoparticle made by flame spray pyrolysis for photoelectrochemical water splitting – Part II. photoelectrochemical study. *Int J Hydrogen Energy* 2011; 36, 15519-15526.
- Chiang CY, Aroh K, Ehrman SH. Copper oxide nanoparticle made by flame spray pyrolysis for photoelectrochemical water splitting – Part I. CuO nanoparticle preparation. *Int J Hydrogen Energy* 2012a.; 37, 4871-4879
- Chiang CY, Shin Y, Aroh K, Ehrman SH. Copper oxide photocathodes prepared by a solution based process” *Int. J. Hydrogen Energ* 2012b; 10.1016/j.ijhydene.2012.02.049
- Chiang CY, Shin Y, Ehrman S. Li doped CuO film electrodes for photoelectrochemical cells. *J Electrochem Soc* 2012c; 159: B227-B231.
- Chiang CY, Chang MH, Liu HS, Tai CY, Ehrman S. Process intensification in the production of photocatalysts for solar hydrogen generation.” *Ind. Eng. Chem. Res.*, 2012d, 51, 5207-5215.
- Chowdhuri A, Gupta V, Sreenivas K, Kumar R, Mozumdar S, Patanjali PK. Response Speed of SnO<sub>2</sub>-based H<sub>2</sub>S Gas Sensors with CuO Nanoparticles. *Appl Phys Lett* 2004; 84:1180-1182.

- Condorelli GG, Malandrino G, Fragalà IL. Nucleation and growth of copper oxide films in MOCVD processes using the  $\beta$ -ketoiminate precursor 4,4'-(1,2-ethanediyldinitrilo)bis(2-pentanolate) copper(II). *Chem Vapor Depos* 1999; 5: 237-244.
- Cruccolini A, Narducci R, Palombari R. Gas adsorption effects on surface conductivity of nonstoichiometric CuO. *Sensor Actuat B-Chem* 2004; 98:227-232.
- Dai PC, Mook HA, Aeppli G, Hayden SM, Dogan F. Resonance as a measure of pairing correlations in the high-Tc superconductor YBa<sub>2</sub>Cu<sub>3</sub>O<sub>6.6</sub>. *Nature* 2000. 406:965-968.
- Drobny VF, Pulfrey L. Properties of reactively-sputtered copper oxide thin films. *Thin Solid Films* 1979; 61: 89-98.
- Du XH, Zhang K, Holland K, Tomblor T, Moskovits M. Chemical corrosion protection of optical components using atomic layer deposition. *Appl Opt*. 2009;48;6470-4.
- Duret A, Gratzel M. Visible light-induced water oxidation on mesoscopic  $\alpha$ -Fe<sub>2</sub>O<sub>3</sub> films made by ultrasonic spray pyrolysis. *J Phys Chem* 2005; 109:17184-91.
- Dujardin E, Peet C, Stubbs G, Culver JN, Mann S. Organization of metallic nanoparticles using tobacco mosaic virus templates. *Nano Lett*. 2003; 3: 413–7.
- Ehrman SH, Friedlander SK. Bimodal distributions of two component metal oxide aerosols. *Aerosol Sci Tech* 1999. 30:259-272.
- El Zayat MY, Saed AO, El-Dessouki MS. Photoelectrochemical properties of dye sensitized Zr-doped SrTiO<sub>3</sub> electrodes. *Int J Hydrogen Energy*. 1998;23:259-66.
- Eliseev AA, Lukashin AV, Vertegel AA, Heifets LI, Zhirov AI, Tretyakov YD. Complexes of Cu(II) with polyvinyl alcohol as precursors for the preparation of CuO/SiO<sub>2</sub> nanocomposites. *Mater Res Innov* 2000; 3:308-312.

- Faglia G, Vomiero A, Sberveglieri G. Nanostructured materials improve efficiency in excitonic solar cells. SPIE. 2009. doi: 10.1117/2.1201001.002531
- Fan HM, Yang LT, Hua WS, Wu XF, Wu ZY, Xie SS, Zou BS. Controlled synthesis of monodispersed CuO nanocrystals. *Nanotechnology* 2004; 15: 37-42.
- Fan HM, Zou BS, Liu YL, Me SS. Size effect on the electron-phonon coupling in CuO nanocrystals. *Nanotechnology* 2006; 17:1099-1103.
- Fan CF, Pan LQ, Zhu H, Qiu HM, Wang FP, Wu P, Qiu H, Zhang Y, Xiao JQ. Structure and magnetic properties of Mn-doped CuO solids. *Trans Nonferrous Met Soc China*. 2005;15;349-52.
- Fatih K, Marsan B. <http://www.electrochem.org/dl/ma/201/pdfs/1372.pdf>
- Finklea HO. In: Finklea HO, editor. *Semiconductor electrodes*. Amsterdam: Elsevier; 1988. p. 1–145.
- Fowler CE, Shenton W, Stubbs G, Mann S. tobacco mosaic virus liquid crystals as templates for the interior design of silica mesophases and nanoparticles. *Adv.Mater.* 2001; 13: 1266–69.
- Frank AJ. In *Energy resources through photochemistry and catalysis*, M. Gratzel, Ed., Academic Press: New York, 1983, p.467.
- Frenkel J. Viscous flow of crystalline bodies under the action of surface tension. *J Phys* 1945; 9:385-391.
- Frietsch M, Zudock F, Goschnick J, Bruns M. CuO Catalyticmembrane as selectivity trimmer for metal oxide gas sensors. *Sensor Actuat B-Chem* 2000; 65:379-381.
- Friedlander SK, Wu MK. Linear rate law for the decay of the excess surface-area of a coalescing solid particle. *Phys Rev B* 1994; 49: 3622-3624.
- Fujishima A, Hashimoto K, Watanabe T. *TiO<sub>2</sub> photocatalysis. Fundamentals and applications*. Tokyo: BKC, Inc.; 1999. p. 14–176.

- Fujishima A, Honda K. Electrochemical photolysis of water at a semiconductor electrode. *Nature* 1972; 238:37.
- Galinska A, Walendziewski J. Photocatalytic water splitting over Pt-TiO<sub>2</sub> in the presence of sacrificial reagents. *Energ Fuel*. 2005;19:1143-7.
- Gao XP, Bao JL, Pan GL, Zhu HY, Huang PX, Wu F, Song DYJ. Preparation and electrochemical performance of polycrystalline and single crystalline CuO nanorods as anode materials for Li ion battery. *J Phys Chem B* 2004; 108:5547-5551.
- Gerischer H. Heterogeneous electrochemical systems for solar energy conversion. *Pure Appl Chem*. 1980;52:2649-67.
- Gerischer J. In: Seraphin BO, editor. *Solar energy conversion*. Berlin: Springer; 1979; 115–72.
- Gerischer H, Tribusch H. *Ber Bunsenges Phys Chem*. 1968;72:1083.
- Ghosh S, Avasthi DK, Shah P, Ganesan V, Gupta A, Sarangi D, Assmann W. Deposition of thin films of different oxides of copper by RF reactive sputtering and their characterization. *Vacuum*. 2000;57:377-85.
- Giordano N, Antonucci V, Cavallaro S, Lembo R, Bart J CJ. Photoassisted decomposition of water over modified rutile electrodes. *Int J Hydrogen Energy*. 1982;7:867-72.
- Gooding GV, Hebert TT. A simple technique for purification of tobacco mosaic virus in large quantities. *Phytopathology*. 1967;57:1285-7.
- Grätzel M. Photoelectrochemical cells. *Nature* 2001; 414:338-44.
- Gupta RB. *Hydrogen fuel: Production, Transport, and Storage*. CRC Press, London, New York, 2009, p.10.
- Guidi F, Moretti G, Carta G, Natali M, Rossetto G, Pierino Z, Salmaso G, Rigato V. Electrochemical anticorrosion performance evaluation of Al<sub>2</sub>O<sub>3</sub> coatings

- deposited by MOCVD on an industrial brass substrate. *Electrochim Acta*. 2005;50:4609-14.
- Hagfeldt A, Gratzel M. Light-induced redox reactions in nanocrystalline systems. *Chem Rev* 1995; 95:49-68.
- Han SY, Lee DH, Herman GS, and Chang CH. Inkjet-printed high mobility transparent-oxide semiconductors. *J Display Technol* 2009; 5, 520-524.
- Hardee KL, Bard AJ. Semiconducting electrodes. 10. Photoelectrochemical behavior of several polycrystalline metal-oxide electrodes in aqueous solutions. *J Electrochem Soc* 1977; 124:215-224.
- Harris LA. Semiconductors for photoelectrolysis. *Ann Rev Mater Sci*. 1978;8:99-134.
- Hensel JK, Zhang J. Photogenerated charge carriers in semiconductor nanomaterials for solar energy conversion. *Int J Nanoparticles*. 2011;4:95-118.
- Heller A. Hydrogen-evolving solar-cells. *Science* 1984; 223:1141-48.
- Hirschwald W. In: Nowotny J, Dufour L-C, editors. *Surface and near-surface chemistry of metal oxides*. Amsterdam: Elsevier; 1988. p. 61.
- Hoffmann MR, Martin ST, Choi W, Bahnemann DW. Environmental applications of semiconductor photocatalysis. *Chem Rev*. 1995;95:69-96.
- Hong ZS, Cao Y, Deng JF. A convenient alcohothermal approach for low temperature synthesis of CuO nanoparticles. *Mater Lett* 2002; 52:34-38.
- Horvath J, Birringer R, Gleiter H. Diffusion in nanocrystalline material. *Solid State Commun* 1987; 62:319-322.
- Hsieh CT, Chen JM, Lin HH, Shih HC. Field emission from various CuO nanostructures. *Appl Phys Lett* 2003; 83:3383-3385.

- Hussain MM, Dincer I, Li X. A preliminary life cycle assessment of PEM fuel cell powered automobiles. *Appl Thermal Eng.* 2007;27:2294-9.
- Hwang DW, Kim HG, Lee JS, Kim J, Li W, Oh SH. Photocatalytic hydrogen production from water over M-doped  $\text{La}_2\text{Ti}_2\text{O}_7$  (M = Cr, Fe) under visible light irradiation ( $\lambda = 420$  nm). *J Phys Chem B.* 2005;109:2093-102.
- Ishii T, Kato H, Kudo A.  $\text{H}_2$  evolution from an aqueous methanol solution on  $\text{SrTiO}_3$  photocatalysts codoped with chromium and tantalum ions under visible light irradiation. *J Photochem Photobiol A.* 2004;16:181-6.
- Ito T, Yamaguchi H, Okabe K, Masumi T. Single-crystal growth and characterization of  $\text{Cu}_2\text{O}$  and  $\text{CuO}$ . *J Mater Sci* 1998; 33:3555-3566.
- Jang HD. Experimental study of synthesis of silica nanoparticles by a bench-scale diffusion flame reactor. *Powder Technol* 2001; 119:102-108.
- Jang HD, Chang H, Okuyama K. Synthesis of binary component metal oxide nanoparticles by flame spray pyrolysis. *Resources Processing* 2007; 54:9-13.
- Jeong YK, Choi GM. Nonstoichiometry and electrical conduction of  $\text{CuO}$ . *J Phys Chem Solids* 1996; 57: 81-84.
- Jia DZ, Yu JQ, Xia X. Synthesis of  $\text{CuO}$  nanometer powder by one step solid state reaction at room temperature. *Chinese Sci Bull* 1998; 43:571-573.
- Jiang Y, Decker S, Mohs C, Klabunde KJ. Catalytic solid state reactions on the surface of nanoscale metal oxide particles. *J Catal* 1998; 180:24-35.
- Khaselev O, Turner JA. A monolithic photovoltaic-photoelectrochemical device for hydrogen production via water splitting. *Science.* 1998;280:425-7.
- Kalyanasundaram K, Grätzel M. Applications of functionalized transition metal complexes in photonic and optoelectronic devices. *Coord Chem Rev.* 1998;177:347-414.

- Kammler HK, Madler L, Pratsinis SE. Flame synthesis of nanoparticles. *Chem Eng Technol* 2001; 24:583-596.
- Kang YC, Seo DJ, Park SB, Park HD. Direct synthesis of strontium titanate phosphor particles with high luminescence by flame spray pyrolysis. *Mater Res Bull* 2002; 37:263-269.
- Kato H, Kudo A. Visible-light-response and photocatalytic activities of TiO<sub>2</sub> and SrTiO<sub>3</sub> photocatalysts codoped with antimony and chromium. *J Phys Chem B*. 2002;106:5029-34.
- Katti VR, Debnath AK, Muthe KP, Kaur M, Dua AK, Gadkari SC, Gupta SK, Sahni VC. Mechanism of drifts in H<sub>2</sub>S sensing properties of SnO<sub>2</sub>:CuO composite thin film sensors prepared by thermal evaporation. *Sensor Actuat. B-Chem* 2003; 96:245-252.
- Kay A, Cesar I, Gratzel M. New benchmark for water photooxidation by nanostructured  $\alpha$ -Fe<sub>2</sub>O<sub>3</sub> films. *J Am Chem Soc* 2006; 128:15714-21.
- Khan SUM, Akikusa J. Photoelectrochemical splitting of water at nanocrystalline n-Fe<sub>2</sub>O<sub>3</sub> thin-film electrodes. *J Phys Chem B* 1999; 103:7184-7189.
- Kingery WD, Bowen HK, Uhlmann DR. *Introduction of ceramics*. New York: Wiley-Interscience; 1976.
- Kiwi J, Gratzel K. Heterogeneous photocatalysis: enhanced dihydrogen production in titanium dioxide dispersions under irradiation. The effect of magnesium promoter at the semiconductor interface. *J Phys Chem*. 1986;90:637-40.
- Kocha SS, Peterson MW, Arent DJ, Redwing JM, Tischler MA, Turner JA. Electrochemical investigation of the gallium nitride-aqueous electrolyte interface. *J Electrochem Soc*. 1995;142:2625-30.



- Kocha SS, Turner J, Nozik AJ. Study of the Schottky barrier and determination of the energetic positions of band edges at the n- and p-type gallium indium phosphide electrode/electrolyte interface. *Electroanal Chem.* 1994;367:27-30.
- Koch W, Friedlander SK. Particle growth by coalescence and agglomeration. *J Aerosol Sci* 1990; 21: S73-S76.
- Kofstad P. Nonstoichiometry, electrical conductivity and diffusion in binary metal oxides. New York: Wiley; 1972.
- Koffyberg FP, Benko FA. A photo-electrochemical determination of the position of the conduction and valence band edges of p-type CuO. *J Appl Phys* 1982; 53:1173-77.
- Konta R, Ishii T, Kato H, Kudo A. Photocatalytic activities of noble metal ion doped SrTiO<sub>3</sub> under visible light irradiation. *J Phys Chem B.* 2004;108:8992-5.
- Kongkanand A, Dominguez RM, Kamat PV. Single wall carbon nanotube scaffolds for photoelectrochemical solar cells. Capture and transport of photogenerated electrons. *Nano Lett.* 2007;7:676-80.
- Kozuka H, Takahashi Y, Zhao G, Yoko T. Preparation and photoelectrochemical properties of porous thin films composed of submicron TiO<sub>2</sub> particles. *Thin Solid Films.* 2000;358:172-9.
- Kuczkowski A. Photoelectrochemical processes at semiconductors. In *Photochemistry and Photophysics, Vol III.* Jan F. Rabek, ed. CRC Press; 1991.
- Laidler KJ, Meiser JH, Sanctuary BC. *Physical Chemistry* 4<sup>th</sup> edition, Houghton Mifflin, 2003. P. 291.
- Larsson PO, Andersson A, Wallengerg RL, Svensson B. Combustion of CO and toluene; characterisation of copper oxide supported on titania and activity comparisons with supported cobalt, iron, and manganese oxide. *J Catal* 1996; 163:279-293.

- Law W, Greene LE, Johnson JC, Saykally R, Yang P, Nanowire dye sensitized solar cells, *Nat. Mater.* 2005; 4: 455.
- Lee S, Royston E, Culver JN. Improved metal cluster deposition on a genetically engineered tobacco mosaic virus template. *Nanotechnology.* 2005;16:435-41.
- Lethinen KEJ, Windeler RS, Friedlander SK. A note on the growth of primary particles in agglomerate structures by coalescence. *J Colloid Interf Sci* 1996; 182: 606-608.
- Li Y, Zhang JZ. Hydrogen generation from photoelectrochemical water splitting based on nanomaterials. *Laser Photonics Rev.* 2012;4:517-28.
- Liao HB, Xiao RF, Wang H, Wong KS, Wong GKL. Large third-order optical nonlinearity in Au:TiO<sub>2</sub> composite films measured on a femtosecond time scale. *Appl Phys Lett.* 1998;72:1817-19.
- Licht S, Wang B, Mukerji S, Soga T, Umeno M, Tributsch H. Efficient solar water splitting, exemplified by RuO<sub>2</sub>-catalyzed AlGaAs/Si photoelectrolysis. *J Phys Chem B.* 2000;104:8920.
- Limaye AU, Helble JJ. Morphological control of zirconia nanoparticles through combustion aerosol synthesis. *J Am Ceram Soc* 2002; 85:1127-1132.
- Linsebigler AL, Lu G, Yates Jr JT. Photocatalysis on TiO<sub>2</sub> surfaces: principles, mechanisms, and selected result. *Chem Rev.* 1996;95:735-58.
- Liu J, Cao G, Yang Z, Wang D, Dubois D, Zhou X, Graff GL, Pederson LR, Zhang JG. Oriented nanostructures for energy conversion and storage. *Chem Sus Chem* 2008; 1:676-97.
- Lu CH, Qi LM, Yang JH, Wang XY, Zhang DY, Xie JL, Ma JM. One-pot synthesis of octahedral Cu<sub>2</sub>O nanocages via a catalytic solution route. *Adv Mater* 2005;17:2562-7.

- Mädler L, Kammler HK, Mueller R, Pratsinis SE. Controlled synthesis of nanostructured particles by flame spray pyrolysis. *J Aerosol Sci* 2002; 33:369-389.
- Matsumura M, Nomura Y, Tsobomura H. Dye-sensitization on the photocurrent at zinc oxide electrode in aqueous electrolyte solution. *Bull Chem Soc Jpn.* 1977;50:2533-37.
- Mizushima K, Tanaka M, Asai A, Iida S, Goodenough JB. Impurity levels of iron-group ions in TiO<sub>2</sub>(II). *J Phys Chem Solids.* 1979;40:1129.
- Mizushima K, Tanaka M, Iida S. Energy levels of iron group impurities in TiO<sub>2</sub>. *J Phys Soc Jpn.* 1972;32:1519-24.
- Morales J, Sa'nchez L, Marti'n F, Ramos-Barrado JR. Use of Low-temperature nanostructured CuO thin films deposited by spray-pyrolysis in lithium cells. *Thin Solid Films* 2005; 474:133-140.
- Morales J, Sanchez L, Marti'n F, Ramos-Barrado JR, Sanchez M. Nanostructured CuO thin film electrodes prepared by spray pyrolysis: a simple method for enhancing the electrochemical performance of CuO in lithium cells. *Electrochim Acta* 2004; 49: 4589–4597.
- Morisaki H, Watanabe T, Iwase M, Yazawa K. Photoelectrolysis of water with TiO<sub>2</sub>-covered solar-cell electrodes. *Appl Phys Lett.* 1976;29:338.
- Morrison SR. *Electrochemistry at semiconductor and oxidized metal electrodes.* New York: Plenum Press; 1980. pp. 1–401.
- Murphy ABB, Barnes PRF, Randeniya LK, Plumb IC, Grey IE, Horne MD, Glasscock JA. Efficiency of solar water splitting using semiconductor electrodes. *Int J Hydrogen Energ* 2006; 31:1999-2017.
- Myrach P, Nilius N, Levchenko SV, Gonchar A, Risse T, Dinse K, Boatner LA, Frandsen W, Horn R, Freund H, Schlegl R, Scheffler M. Temperature-dependent

- morphology, magnetic and optical properties of Li-doped MgO. *ChemCatChem* 2010; 2: 854-862.
- Nakaoka K, Ueyama J, Ogura K. Photoelectrochemical behavior of electrodeposited CuO and Cu<sub>2</sub>O thin films on conducting substrates. *J Electrochem Soc* 2004; 151:C661-65.
- Nakatano Y, Shioji M, Tsubomura H. Photoeffects on the potentials of thin metal films on a n-TiO<sub>2</sub> crystal wafer. The mechanism of semiconductor photocatalysts. *Chem Phys Lett.* 1982;90:453.
- Namba K, Pattanayak T, Stubbs GJ. Visualization of protein-nucleic acid interactions in a virus: refinement of intact tobacco mosaic virus at 2.9 Å resolution by X-ray fiber diffraction. *J Mol Biol.* 1989;28:307-25.
- Nanthakumar A, Armstrong NR. In: Finklea HO, editor. *Semiconductor electrodes.* Amsterdam: Elsevier; 1988. p. 203–40.
- Navarro Yerga RM, Alvarez Galvan MC, del Valle F, de la Mano JAV, Fierro JLG. Water splitting on semiconductor catalysts under visible-light irradiation. *ChemSusChem.* 2009; 2:471-485.
- Nishimura N, Raphael B, Maeda K, Gendre L, Abe R, Kubota J, Domen K. Effect of TiCl(4) treatment on the photoelectrochemical properties of LaTiO<sub>2</sub>N electrodes for water splitting under visible light. *Thin Solid Films.* 2010;518;5855-9.
- Nowotny J. In: Nowotny J, Dufour L-C, editors. *Surface and near-surface chemistry of metal oxides.* Amsterdam: Elsevier; 1988. p. 281.
- Nowotny J. In: Nowotny J, editor. *Science of ceramic interfaces II.* Amsterdam: Elsevier; 1994. p. 1.
- Nowotny J. Interface defect chemistry and its impact on properties of oxide ceramic materials. In: Nowotny J, editor. *Science of materials interfaces.* Amsterdam: Elsevier; 1991. pp. 79–204.

- Nowotny J. Interface electrical phenomena in ionic solids. In: Gellings PJ, Bouwmeester HJM, editors. The CRC handbook of solid-state electrochemistry. Boca Raton: CRC Press; 1977. p. 121–159.
- Nowotny J. Nonstoichiometry and related properties of ceramic interfaces. In: Nowotny J, editor. Science of materials interfaces II. Amsterdam: Elsevier; 1997.
- Nowotny J, Radecka M, Rekas M. Semiconducting properties of undoped TiO<sub>2</sub>. J Phys Chem Solids. 1997;58:927-37.
- Nozik A. Photoelectrochemistry: applications to solar energy conversion. Ann Rev Phys Chem. 1978;29:189-222.
- Nozik AJ. p - n photoelectrolysis cells. Appl Phys Lett. 1976;29:150-3.
- Ohya Y, Ito S, Ban T, Takahashi Y. Preparation of CuO thin films and their electrical conductivity. Key Eng Mat 2000; 181-182: 113-116.
- Odgen JM. Prospects for building a hydrogen energy infrastructure. Annu Rev Energy Environ. 1999;24:227-79.
- Ogden JM, Dennis E, Steinbugler M, Strohbahn J. Hydrogen Energy Systems Studies. Final Report. Department of Energy (US); 1995 Jan 18. Contract No.: XR-11265-2.
- O'Regan B, Gratzel M. A low-cost, high-efficiency solar cell based on dye-sensitized colloidal TiO<sub>2</sub> films. Nature. 1991;353:737-40.
- Paracchino A, Laporte V, Sivula K, Gratzel M, Thimsen E. Highly active oxide photocathode for photoelectrochemical water reduction. Nature Materials. 2011; 10: 456-461.
- Parkinson BA, Spitler AM. Recent advances in high quantum yield dye sensitization of semiconductor electrodes. Electrochem Acta. 1992;37: 943-8.

- Parretta A, Jayaraj MK, Di Nocera A, Loreti S, Quercia L, Agati A. Electrical and optical properties of copper oxide films prepared by reactive RF magnetron sputtering. *Phys Status Solidi A*. 1996;155:399–404.
- Pati RK, Lee IC, Hou, S, Akjuemonkhanm O, Gaskell KJ, Wang Q, Frenkel AI, Chu D, Salamanca-Riba LG, Ehrman SH. Flame Synthesis of Nanosized Cu-Ce-O, Ni-Ce-O, and Fe-Ce-O Catalysts for the Water-Gas Shift (WGS) Reaction. *ACS Applied Materials & Interfaces* 2009; 1:2624-2635.
- Peter LM. The gratzel cell: where next? *J Phys Chem Lett*. 2011;2:1861-7.
- Petrantoni M, Rossi C, Conedera V, Bourrier D, Alphonse P, Tenailleau C. Synthesis process of nanowired Al/CuO thermite. *J Phys Chem Solids* 2010; 71: 80-83.
- Petrantoni M, Rossi C, Salvagnac L, Conedera V, Esteve A, Tenailleau C, Alphonse P, Chabal YJ. Multilayered Al/CuO thermite formation by reactive magnetron sputtering: nano versus micro. *Journal of Applied Physics*. 2010;108: 084323-5.
- Poizot P, Laruelle S, Grugeon S, Dupont L, Tarascon JM. Nano-sized transition-metaloxides as negative-electrode materials for lithium-ion batteries. *Nature* 2000; 407:496-499.
- Pratsinis SE. Flame aerosol synthesis of ceramic powders. *Prog Energ Combust* 1998; 23:197-219.
- Qu P, Meyer GJ. In: *Electron Transfer in Chemistry* (Ed: V Balzani). New York: Wiley; 2001. p. 355.
- Rajeshwar K. Hydrogen generation at irradiated oxide semiconductor-solution interfaces. *J. Appl. Electrochem*. 2007; 37:765-87.
- Rebane JA, Yakovlev NV, Chicherin DS, Tretyakov YD, Leonyuk LI, Yakuninc VG. An experimental study of copper self-diffusion in CuO, Y<sub>2</sub>Cu<sub>2</sub>O<sub>5</sub> and YBa<sub>2</sub>Cu<sub>3</sub>O<sub>7-x</sub> by secondary neutral mass spectrometry. *J Mater Chem* 1997; 7: 2085–2089.

- Reisfeld R, Eyal M, Brusilovsky D. Luminescence enhancement of rhodamine 6G in sol-gel films containing silver aggregates. *Chem Phys Lett.* 1988;153:210.
- Reitz JB, Solomon EI. Propylene oxidation on copper oxide surfaces: electronic and geometric contributions to reactivity and selectivity. *J Am Chem Soc* 1998; 120:11467-11478.
- Rifkin J. *The Hydrogen Economy.* New York: Penguin Putnam Inc.; 2002.
- Ritterskamp P, Kuklya A, Wüstkamp MA, Kerpen K, Weidenthaler C, Demuth M. A titanium disilicide derived semiconducting catalyst for water splitting under solar radiation-reversible storage of oxygen and hydrogen. *Angew Chem Int Ed.* 2007;46:7770-4.
- Roel VDK, Grätzel M. *Photoelectrochemical hydrogen production.* Berlin: Springer, 2011.
- Royston E, Ghosh A, Kofinas P, Harris MT, Culver JN. Self-assembly of virus-structured high surface area nanomaterials and their application as battery electrodes. *Langmuir.* 2008;24:906-12.
- Saito K, Ikeuchi S, Nakazawa Y, Zhang X, Maple MB, Sorai M. Phase diagram of lithium-doped copper oxide,  $\text{Cu}_{1-x}\text{Li}_x\text{O}$ . *Solid State Communications.* 2003;125:23-6.
- Samarasekera P. A solution of the Heisenberg Hamiltonian for oriented thick ferromagnetic films. *Chinese Journal of Physics* 2006; 44: 377-386.
- Santos A, Yustos P, Quintanilla A, Ruiz G, Garcia-Ochoa F. Study of the copper leaching in the wet oxidation of phenol with CuO-based catalysts: Causes and Effects. *Appl Catal B-Environ* 2005; 61:323-333.
- Saremi-Yarahmadi S, Tahir AA, Vaidhyanathan B, Wijayantha KGU. Fabrication of nanostructured  $\alpha\text{-Fe}_2\text{O}_3$  electrodes using ferrocene for solar hydrogen generation. *Mater Lett* 2009; 63:523-26.

- Schultze JW, Lohrengel MM. Stability, reactivity and breakdown of passive films. Problems of recent and future research. *Electrochim Acta* 2000; 45: 2499–2513.
- Seraphin BO. In: Seraphin BO, editor. *Solar energy conversion*. Berlin: Springer; 1979. p. 5–56.
- Shan CX, Hou XH, Choy KL. Corrosion resistance of TiO<sub>2</sub> films grown on stainless steel by atomic layer deposition. *Surf Coat Technol.* 2008;202;2399-402.
- Shah A, Mittal N, Bhati I, Sharma VK, Punjabi PB. Photocatalytic degradation of crystal violet by use of copper oxide as semiconductor. *Pol J Chem* 2009; 83:2001-2007.
- Shenton W, Douglas T, Young M, Stubbs G, Mann S. Inorganic–organic nanotube composites from template mineralization of tobacco mosaic virus. *Adv Mater.* 1999;11:253-6.
- Siripala W, Ivanovskaya A, Jaramillo TF, Baeck SH, McFarland EW. A Cu<sub>2</sub>O/TiO<sub>2</sub> heterojunction thin film cathode for photoelectrocatalysis. *Sol Energ Mater Sol C.* 2003;77;229-37.
- Son DI, You CH, Kim TW. Structural, Optical, and electronic properties of colloidal CuO nanoparticles formed by using a colloid-thermal synthesis process. *Appl Surf Sci* 2009; 255:8794-8797.
- Steigerwald JM, Duquette DJ, Murarka SP, Gutmann RJ. Electrochemical potential measurements during the chemical-mechanical polishing of copper thin films. *J Electrochem Soc.* 1995;142;2379-85.
- Strataki N, Antoniadou M, Dracopoulos V, Lianos P. Visible-light photocatalytic hydrogen production from ethanol–water mixtures using a Pt–CdS–TiO<sub>2</sub> photocatalyst. *Catal Today.* 2010;151;53-7.
- Strobel R, Baiker A, Pratsinis SE. Aerosol flame synthesis of catalysts. *Adv Powder Technol* 2006; 17:457-480.



- Suda S, Fujitsu S, Koumoto K, Yanagida H. The effect of atmosphere and doping on electrical conductivity of CuO. *Jpn J Appl Phys* 1992; 31: 2488-2491.
- Tahir AA, Wijayantha KGU, Saremi-Yarahmadi S, Mazhar M, Mckee V. Nanostructured r-Fe<sub>2</sub>O<sub>3</sub> thin films for photoelectrochemical hydrogen generation. *Chem Mater* 2009; 21:3763-72.
- Tani T, Takatori K, Pratsinis SE. Evolution of the morphology of zinc oxide/silica particles made by spray combustion. *J Am Ceram Soc* 2004; 87:365-370.
- Tseng RJ, Tsai CL, Mai LP, Quyang JY. Bio-based digital memory device on tobacco mosaic virus conjugated with nanoparticles. *Nat Nanotechnol*. 2006;1:72-7.
- Tsubomura H, Nakato Y. Solar-energy conversion by means of photoelectrochemical methods-metal coated silicon photoelectrodes. *New J. Chim* 1987; 11: 167.
- Turner JA. A realizable renewable energy future. *Science*. 1999; 285:687-9.
- Turner J, Sverdrup G, Mann MK, Maness PC, Kroposki B, Ghirardi M, Evans RJ, Blake D. Renewable hydrogen production. *Int J Energ Res*. 2008;32:379–407.
- Ulrich GD. Theory of particle formation and growth in oxide synthesis flames. *Combust Sci Technol* 1971; 4: 47-&.
- Uno M, Kosuga A, Okui M, Horisaka K, Yamanaka S. Photoelectrochemical study of lanthanide titanium oxides; Ln<sub>2</sub>Ti<sub>2</sub>O<sub>7</sub> (Ln = La, Sm, and Gd). *J Alloy Compd*. 2005;400;270-5.
- Veziroglou TN. Dawn of the hydrogen age. *Int J Hydrogen Energy* 1998;23:1077–978.
- Veziroglou TN. Quarter century of hydrogen movement 1974–2000. *Int J Hydrogen Energy*. 2000;25:1143–50.
- Vijayakumar R, Elgamiel R, Diamant Y, Gedanken A. Sonochemical preparation and characterization of nanocrystalline copper oxide embedded in poly(vinyl alcohol) and its effect on crystal growth of copper oxide. *Langmuir* 2001; 17: 1406–1410.

- Wang J, Yang J, Sun J, Bao Y. Synthesis of copper oxide nanomaterials and the growth mechanism of copper oxide nanorods. *Mater Des* 2004; 25: 625–629.
- Wang MH, Guo RJ, Tso TL, Preng TP. Effects of sintering on the photoelectrochemical properties of Nb-doped TiO<sub>2</sub> electrodes. *Int J Hydrogen Energy*. 1995;20:555-60.
- Wang P, Zakeeruddin SM, Moser JE, Humphry-Baker R, Comte P, Aranyos V, Hagfeldt A, Nazeeruddin MK, Gratzel M. Stable new sensitizer with improved light harvesting for nanocrystalline dye-sensitized solar cells. *Adv Mater*. 2004; 16; 1806-11.
- Wang Y, Cheng H, Hao Y, Ma J, Li W, Cai S. Photoelectrochemical properties of metal-ion-doped TiO<sub>2</sub> nanocrystalline electrodes. *Thin Solid Films*. 1999;349:120-5.
- Wenham SR, Green MA, Watt ME. *Applied photovoltaics*. Centre for Photovoltaic Devices and Systems; Sydney; 1994. p. 239–46.
- Windeler RS, Lehtinen KEJ, Friedlander SK. Production of nanometer-sized metal oxide particles by gas phase reaction in a free jet II: particle size and neck formation - comparison with theory. *Aerosol Sci Technol* 1997; 27:191-205.
- Wu MK, Ashburn JR, Torng CJ, Hor PH, Meng RL, Gao L, Huang ZJ, Wang YQ, Chu CW. Superconductivity at 93-K in a new mixed-phase Y-Ba-Cu-O compound system at ambient pressure. *Phys Rev Lett* 1987; 58:908-910.
- Wu MK, Windeler RS, Steiner CKR, Borst T, Friedlander SK. Controlled synthesis of nanosized particles by aerosol processes. *Aerosol Sci Tech* 1993; 19: 527-548.
- Yang JP, Meldrum FC, Fendler JH. Morphology control of PbS nanocrystallites, epitaxially under mixed monolayers. *J Phys Chem* 1995;99:5505-11.
- Yang Z, Xu J, Zhang W, Liu A, Tang S. Controlled synthesis of CuO nanostructures by a simple solution route. *J Solid State Chem* 2007;180:1390-6.

- Yilanci A, Dincer I, Ozturk HK. A review on solar-hydrogen/fuel cell hybrid energy systems for stationary applications. *Prog Energy Combust* 2009; 35:231-44.
- Zhang Y, Wang S, Li X, Chen L, Qian Y, Zhang Z. CuO shuttle-like nanocrystals synthesized by oriented attachment. *J Cryst Growth* 2006; 291: 196–201.
- Zhang HR, Shen CM, Chen ST, Xu ZH, Liu FS, Li JQ, Gao HJ. Morphologies and microstructures of nano-sized Cu<sub>2</sub>O particles using a cetyltrimethylammonium template. *Nanotechnology* 2005;16:267-70.
- Zhang Z, Wang P. Highly stable copper oxide composite as an effective photocathode for water splitting via a facile electrochemical synthesis strategy. *J Mater Chem.* 2012;22:2456-64.
- Zhao G, Kozuka H, Yoko T. Effects of the incorporation of silver and gold nanoparticles on the photoanodic properties of rose bengal sensitized TiO<sub>2</sub> film electrodes prepared by sol-gel method. *Sol Energy Sol Cells.* 1997;46:219-31.
- Zhao G, Kozuka H, Lin H, Takahashi M, Yoko T. Preparation and photoelectrochemical properties of Ti<sub>1-x</sub>V<sub>x</sub>O<sub>2</sub> solid solution thin film photoelectrodes with gradient bandgap. *Thin Solid Films.* 1999;340:125-31.
- Zhao G, Kozuka H, Yoko T. Sol—gel preparation and photoelectrochemical properties of TiO<sub>2</sub> films containing Au and Ag metal particles. *Thin Solid Films.* 1996; 277: 147-54.
- Zhu J, Yu Z, Fan S, Cui Y. Nanostructured photon management for high performance solar cells. *Mater. Sci. Eng., R.* 2010; 70, 330-40.